

Current Status of Numerical-Relativity Simulations in Kyoto

Yuichiro SEKIGUCHI¹, Kenta KIUCHI¹, Koutarou KYUTOKU^{1,2}, Masaru SHIBATA¹

¹*Yukawa Institute for Theoretical Physics, Kyoto University,
Kyoto 606-8502, Japan,*

²*Theory Center, Institute of Particle and Nuclear Studies, KEK, Tsukuba, Ibaraki
305-0801, Japan*

We describe the current status of our numerical simulations for the collapse of a massive stellar core to a black hole (BH) and the merger of binary neutron stars (BNS), performed in the framework of full general relativity incorporating finite-temperature equations of state (EOS) and neutrino cooling.

For the stellar core collapse simulation, we present the latest numerical results. We employed a purely nucleonic EOS derived by Shen et al. (Nucl. Phys. A **637** (1998), 435). As an initial condition, we adopted a 100 M_{\odot} presupernova model calculated by Umeda and Nomoto (Astrophys. J. **637** (2008), 1014), which has a massive core ($M \approx 3M_{\odot}$) with a high value of entropy per baryon ($s \approx 4k_B$). Changing the degree of rotation for the initial condition, we clarify the strong dependence of the outcome of the collapse on this. When the rotation is rapid enough, the shock wave formed at the core bounce is deformed to be a torus-like shape. Then, the infalling matter is accumulated in the central region due to the oblique shock at the torus surface, hitting the proto-neutron star and dissipating the kinetic energy there. As a result, outflows can be launched. The proto-neutron eventually collapses to a BH and an accretion torus is formed around it. We also found that the evolution of the BH and torus depends strongly on the rotation initially given.

In the BNS merger simulations, we employ an EOS incorporating a degree of freedom for hyperons derived by Shen et al. (Astrophys. J. Suppl. **197** (2011), 20), in addition to the purely nucleonic EOS. The numerical simulations show that for the purely nucleonic EOS, a hypermassive neutron star (HMNS) with a long lifetime ($\gg 10$ ms) is the outcome for the total mass $M \lesssim 3.0M_{\odot}$. By contrast, the formed HMNS collapses to a BH in a shorter time scale with the hyperonic EOS for $M \gtrsim 2.7M_{\odot}$. It is shown that the typical total neutrino luminosity of the HMNS is $\sim 3\text{--}10 \times 10^{53}$ ergs/s and the effective amplitude of gravitational waves from the HMNS is $2\text{--}6 \times 10^{-22}$ at $f \approx 2\text{--}2.5$ kHz for a source distance of 100 Mpc.

§1. Introduction

Along with the development of formulations and numerical techniques, as well as progress in computational resources, numerical relativity (NR) is now the most viable approach for exploring phenomena accompanying strong gravitational fields, such as gravitational collapse of massive stellar core to a black hole (BH) or a neutron star (NS) and coalescence of compact-star binaries. These phenomena show a wide variety of observable signatures, including electromagnetic radiation, neutrinos, and gravitational radiation, and observations of neutrinos and gravitational radiation will provide us unique information of strong gravity and properties of dense nuclear matter otherwise cannot be obtained. Next-generation kilo-meter-size gravitational-wave detectors such as LIGO,¹⁾ VIRGO,²⁾ and KAGRA³⁾ will report the first detection of gravitational waves in the next ~ 5 years. In addition, the above phenomena are promising candidates of the central engine of long gamma-ray bursts (LGRB) and short gamma-ray bursts (SGRB).⁴⁾

All four known forces of nature are involved and play important roles in the stellar core collapse and the merger of binary compact objects: General relativistic gravity plays a crucial role in the formation of a BH and a neutron star. Neutrinos produced by weak-interaction processes govern the energy and chemical evolution of the system. The electromagnetic and strong interactions determine the thermodynamical properties, in particular equation of state (EOS) of the dense nuclear matter. Strong magnetic field, if it is present, can modify the dynamics of the matter motion. To study the dynamical phenomena in general relativity, therefore, a multi-dimensional simulation incorporating a wide variety of physics is necessary.

We performed a simulation of stellar core collapse to a neutron star¹¹⁾ and a black hole,¹²⁾ incorporating a finite-temperature, a self-consistent treatment of the electron capture, and neutrino cooling by a detailed leakage scheme, for the first time. Such multi-dimensional simulations had not been done in full general relativity until quite recently ^{*}). Ott et al.⁷⁾ (see also Dimmelmeyer et al.⁸⁾) performed fully general relativistic simulations of stellar core collapse, employing a finite-temperature EOS derived by Shen et al.⁹⁾ (Shen-EOS) for the first time. In their calculation, however, the electron capture rate was not calculated in a self-consistent manner and neutrino cooling is not taken into account. Instead, they adopted a simple parameterized prescription proposed by Ref. 10): The electron fraction is assumed to be a function of density which is presumed based on a result of a single core collapse simulation with a specific initial condition. Recently, Müller et al.¹³⁾ performed simulations of stellar core collapse with detailed microphysics and neutrino transfer. However it is done in the framework of an approximate general relativistic gravity.¹⁴⁾ Kuroda et al.¹⁵⁾ have made a fully general relativistic code with an approximate treatment of neutrino transfer, applying the schemes developed by the authors.^{11),16)} Ott et al.¹⁷⁾ performed simulations of rotating stellar core collapse, employing the parameterized prescription¹⁰⁾ in the collapse phase, and a ray-by-ray neutrino leakage scheme after bounce.

As for the compact-star binary mergers, there have been only a few studies in general relativistic frameworks ^{**}). In the framework of an approximate general relativistic gravity (the conformal flatness approximation¹⁸⁾), Oechslin and Janka¹⁹⁾ performed simulations of binary neutron star (BNS) mergers adopting the Shen-EOS and a finite-temperature EOS by Lattimer and Swesty,²⁰⁾ but they did not take account of weak interaction processes. Duez et al.²³⁾ studied effects of EOS on the dynamics of black hole-neutron star mergers (BHNS) adopting the Shen-EOS in full general relativity. Recently, Bauswein et al.²⁴⁾ performed BNS simulations adopting a wide variety of EOS in the conformal flatness approximation and investigated the dependence of gravitational wave spectra on EOS. In these works, however, the weak interaction processes are not included.

In this paper, we describe our latest results of numerical-relativity simulations

^{*}) There are a number of simulations of stellar core collapse in spherical symmetry⁶⁾ in which Boltzmann's equation is solved and detailed microphysical processes are implemented.

^{**}) There are several studies of binary neutron star mergers in Newtonian frameworks in which finite-temperature EOS and weak interactions are taken into account together with neutrino cooling.^{21), 22)}

for the stellar core collapse to a BH⁽²⁶⁾ and the BNS merger,^(27),28) which are performed incorporating both a finite-temperature EOS^(9),25) and neutrino cooling.⁽¹¹⁾ For reviews on other topics, namely, simulations of stellar core collapse to a neutron star, of BHNS merger, and of BH-BH binary merger, the reader may refer to Refs. 30), 29), 31), Refs. 32), 33) and Refs. 36), 35), respectively.

The paper is organized as follows. In § 2, we first briefly summarize basic equations, input microphysics, and numerical setup. The results of simulations of the stellar core collapse and BNS merger are described in § 3 and § 4, respectively. Section 5 is devoted to a summary. Throughout this paper, \hbar , k_B , c , and G denote the Planck's constant, the Boltzmann's constant, the speed of light, and the gravitational constant, respectively. In appendices, details of the microphysics adopted in our latest implementation are summarized for the purpose of completeness. We adopt the geometrical unit $c = G = 1$ in § 2.1 and § 2.2.

§2. Basic Equations and Numerical Method

2.1. Einstein's equations and gauge conditions

The standard variables in the 3+1 decomposition of Einstein's equations are the three-dimensional metric γ_{ij} and the extrinsic curvature K_{ij} on a three-dimensional hypersurface defined by⁽³⁷⁾

$$\gamma_{\mu\nu} \equiv g_{\mu\nu} + n_\mu n_\nu, \quad (2.1)$$

$$K_{\mu\nu} \equiv -\frac{1}{2}\mathcal{L}_n \gamma_{\mu\nu}, \quad (2.2)$$

where $g_{\mu\nu}$ is the spacetime metric, n_μ is the unit normal to the three-dimensional hypersurface, and \mathcal{L}_n is the Lie derivative with respect to the unit normal n^μ . Then the line element is written in the form

$$ds^2 = -\alpha^2 dt^2 + \gamma_{ij}(dx^i + \beta^i dt)(dx^j + \beta^j dt), \quad (2.3)$$

where α and β^i are the lapse function and the shift vector, which describe the gauge degree of freedom.

Numerical simulations are performed in the so-called BSSN-puncture formulation,^(38),39),40) in which the spatial metric, γ_{ij} , is conformally decomposed as $\gamma_{ij} = W^{-2}\tilde{\gamma}_{ij}$ where the condition, $\det(\tilde{\gamma}_{ij}) = 1$, is imposed for the conformal spatial metric $\tilde{\gamma}_{ij}$. From this condition, the conformal factor is written as $W^{-6} = \det(\gamma_{ij})$. The extrinsic curvature, K_{ij} , is decomposed into the trace part, K , and the traceless part, A_{ij} , as $K_{ij} = A_{ij} + (1/3)\gamma_{ij}K$. The traceless part is conformally decomposed as $A_{ij} = W^{-2}\tilde{A}_{ij}$. To summarize, the fundamental quantities for the evolution equation are now split into W , $\tilde{\gamma}_{ij}$, K , and \tilde{A}_{ij} . Furthermore, the auxiliary variable $F_i \equiv \delta^{jk}\partial_k \tilde{\gamma}_{ij}$ is introduced in the original version of the BSSN formulation.⁽³⁸⁾ Merits of using W as a conformal factor are that (i) the equation for the Ricci tensor is slightly simplified, (ii) no singular term appears in the evolution equations even for $W \rightarrow 0$, and (iii) the determinant of γ_{ij} is always positive.^(41),42)

The basic equations to be solved are

$$(\partial_t - \beta^k \partial_k) W = \frac{1}{3} (\alpha K - \partial_k \beta^k) W, \quad (2.4)$$

$$(\partial_t - \beta^k \partial_k) \tilde{\gamma}_{ij} = -2\alpha \tilde{A}_{ij} + \tilde{\gamma}_{ik} \partial_j \beta^k + \tilde{\gamma}_{jk} \partial_i \beta^k - \frac{2}{3} \tilde{\gamma}_{ij} \partial_k \beta^k, \quad (2.5)$$

$$(\partial_t - \beta^k \partial_k) K = -D^k D_k \alpha + \alpha \left[\tilde{A}_{ij} \tilde{A}^{ij} + \frac{1}{3} K^2 \right] + 4\pi \alpha (e_h^{\text{Total}} + S^{\text{Total}}), \quad (2.6)$$

$$\begin{aligned} (\partial_t - \beta^k \partial_k) \tilde{A}_{ij} = & \alpha W^2 \left(R_{ij} - \frac{1}{3} \tilde{\gamma}_{ij} R \right) - \left(W^2 D_i D_j \alpha - \frac{1}{3} \tilde{\gamma}_{ij} D^k D_k \alpha \right) \\ & + \alpha \left(K \tilde{A}_{ij} - 2 \tilde{A}_{ik} \tilde{A}^k_j \right) + \tilde{A}_{ik} \partial_j \beta^k + \tilde{A}_{jk} \partial_i \beta^k - \frac{2}{3} \tilde{A}_{ij} \partial_k \beta^k \\ & - 8\pi \alpha \left(W^2 S_{ij}^{\text{Total}} - \frac{1}{3} \tilde{\gamma}_{ij} S^{\text{Total}} \right), \end{aligned} \quad (2.7)$$

$$\begin{aligned} (\partial_t - \beta^k \partial_k) F_i = & -16\pi \alpha j_i^{\text{Total}} \\ & + 2\alpha \left\{ f^{kj} \partial_j \tilde{A}_{ik} + \tilde{A}_{ik} \partial_j f^{kj} - \frac{1}{2} \tilde{A}^{jl} \partial_i h_{jl} - 3 \tilde{A}^k_i \partial_k \ln W - \frac{2}{3} \partial_i K \right\} \\ & + \delta^{jk} \left\{ -2 \tilde{A}_{ij} \partial_k \alpha + (\partial_k \beta^l) \partial_l h_{ij} \right. \\ & \left. + \partial_k \left(\tilde{\gamma}_{il} \partial_j \beta^l + \tilde{\gamma}_{jl} \partial_i \beta^l - \frac{2}{3} \tilde{\gamma}_{ij} \partial_l \beta^l \right) \right\}, \end{aligned} \quad (2.8)$$

where $f^{ij} \equiv \tilde{\gamma}^{ij} - \delta^{ij}$, ${}^{(3)}R$, ${}^{(3)}R_{ij}$, and D_i are the Ricci scalar, the Ricci tensor, and the covariant derivative associated with three-dimensional metric γ_{ij} , respectively. The matter source terms are the projections of the stress-energy tensor (see Eq. (2.20)) with respect to n^μ and $\gamma_{\mu\nu}$, and $S^{\text{Total}} \equiv \gamma^{ij} S_{ij}^{\text{Total}}$.

$$e_h^{\text{Total}} \equiv (T^{\text{Total}})^{\alpha\beta} n_\alpha n_\beta, \quad (2.9)$$

$$j_i^{\text{Total}} \equiv -(T^{\text{Total}})^{\alpha\beta} \gamma_{i\alpha} n_\beta, \quad (2.10)$$

$$S_{ij}^{\text{Total}} \equiv (T^{\text{Total}})^{\alpha\beta} \gamma_{i\alpha} \gamma_{j\beta}, \quad (2.11)$$

where $(T^{\text{Total}})_{\alpha\beta}$ is the total energy-momentum tensor (see Eq. (2.14) for definition).

As a gauge condition for the lapse, we use a dynamical slicing^{43), 44) *}:

$$(\partial_t - \beta^k \partial_k) \alpha = -2K\alpha. \quad (2.12)$$

It is known that this dynamical slicing enables to perform a long-term-evolution simulation of neutron stars and BH spacetime. The shift vector is determined by solving a dynamical-shift equation⁴⁶⁾

$$\partial_t \beta^k = \tilde{\gamma}^{kl} (F_l + \Delta t \partial_t F_l). \quad (2.13)$$

Here the second term in the right-hand side is necessary for the numerical stability, and Δt denotes the numerical timestep.

*) In the axisymmetric stellar core collapse simulation described in § 3, we do not include the advection term $\beta^k \partial_k \alpha$.

A fourth-order-accurate finite differencing in space and a fourth-order Runge-Kutta time integration are used in solving Einstein's equations and the gauge conditions.

2.2. Hydrodynamic equations and GR leakage scheme

Numerical simulations were performed using a fully general relativistic hydrodynamic code¹¹⁾ recently developed, in which a nuclear-theory-based finite-temperature EOS, a self-consistent treatment of electron and positron captures, and neutrino cooling by a general relativistic leakage scheme, are implemented.

Because the characteristic timescale of the weak-interaction processes ($t_{\text{wp}} \sim |Y_e/\dot{Y}_e|$) is much shorter than the dynamical timescale, t_{dyn} , in hot dense matters, source terms in the hydrodynamic equations become too *stiff* for the equations to be solved explicitly in a straightforward manner.⁴⁵⁾ A very short timestep ($\Delta t < t_{\text{wp}} \ll t_{\text{dyn}}$) will be required to solve the equations explicitly. The characteristic timescale, t_{leak} , with which neutrinos leak out from the system, by contrast, is much longer than t_{wp} in the hot dense matter region, as $t_{\text{leak}} \sim L/c \sim t_{\text{dyn}}$, where L is the characteristic length scale of the system. Using this fact, we developed a method of solving the hydrodynamic equations in which the source terms are characterized by the leakage timescale t_{leak} .

Note that neutrino heating is not included in the current version of the leakage scheme. A conservative shock capturing scheme⁴⁷⁾ with third-order accuracy in space and fourth-order accuracy in time is employed for solving hydrodynamic equations. In this section, we adopt the geometrical unit $c = G = 1$.

2.2.1. Energy-momentum conservation equation

The basic equations of general relativistic hydrodynamics including the radiation transfer for neutrinos are

$$\nabla_\alpha (T^{\text{Total}})^\alpha_\beta = \nabla_\alpha [(T^{\text{F}})^\alpha_\beta + (T^\nu)^\alpha_\beta] = 0, \quad (2.14)$$

where $(T^{\text{Total}})_{\alpha\beta}$ is the total energy-momentum tensor, and $(T^{\text{F}})_{\alpha\beta}$ and $(T^\nu)_{\alpha\beta}$ are the energy-momentum tensor of fluids and neutrinos, respectively. Equation (2.14) can be decomposed, by introducing the interaction source term, as

$$\nabla_\alpha (T^{\text{F}})^\alpha_\beta = -Q_\beta, \quad (2.15)$$

$$\nabla_\alpha (T^\nu)^\alpha_\beta = Q_\beta. \quad (2.16)$$

Here the source term Q_α is characterized by t_{wp} and becomes too stiff in hot dense matter regions. To overcome the situation, the following procedures are adopted.

1. The neutrino energy-momentum tensor is decomposed into 'trapped-neutrino' $((T^{\nu,\text{T}})_{\alpha\beta})$ and 'streaming-neutrino' $((T^{\nu,\text{S}})_{\alpha\beta})$ parts as

$$(T^\nu)_{\alpha\beta} = (T^{\nu,\text{T}})_{\alpha\beta} + (T^{\nu,\text{S}})_{\alpha\beta}. \quad (2.17)$$

Here, the trapped-neutrino part phenomenologically represents neutrinos which interact sufficiently frequently with matter, and the streaming-neutrino part

describes a phenomenological flow of neutrinos which freely stream out of the system^{*)}

2. A part of neutrinos produced by Eq. (2.16) is assumed to *leak out* to be the streaming-neutrinos with a leakage rate Q_α^{leak} :

$$\nabla_\alpha (T^{\nu, S})^\alpha_\beta = Q_\beta^{\text{leak}}. \quad (2.18)$$

On the other hand, it is assumed that the remaining neutrinos constitute the trapped-neutrino part:

$$\nabla_\beta (T^{\nu, T})^\beta_\alpha = Q_\alpha - Q_\alpha^{\text{leak}}. \quad (2.19)$$

3. The trapped-neutrinos is combined with the fluid part as

$$T_{\alpha\beta} \equiv (T^F)_{\alpha\beta} + (T^{\nu, T})_{\alpha\beta}. \quad (2.20)$$

Then the equation for $T_{\alpha\beta}$ is

$$\nabla_\alpha T^\alpha_\beta = -Q_\beta^{\text{leak}}. \quad (2.21)$$

We solve Eqs. (2.18) and (2.21). Note that the new equations only include the source term, Q_α^{leak} , which is characterized by the leakage timescale t_{leak} . Definition of Q_α^{leak} is given in § 2.3.2.

The energy-momentum tensor of the fluid and trapped-neutrino parts ($T_{\alpha\beta}$) is treated as that of a perfect fluid,

$$T_{\alpha\beta} = (\rho + \rho\varepsilon + P)u_\alpha u_\beta + Pg_{\alpha\beta}, \quad (2.22)$$

where ρ and u^α are the rest mass density and the 4-velocity of the fluid. The specific internal energy (ε) and the pressure (P) are the sum of the contributions from the baryons (free protons, free neutrons, α -particles, and heavy nuclei), leptons (electrons, positrons, and *trapped-neutrinos*), and photons as,

$$P = P_B + P_e + P_{ph} + P_{(\nu)}, \quad (2.23)$$

$$\varepsilon = \varepsilon_B + \varepsilon_e + \varepsilon_{ph} + \varepsilon_{(\nu)}, \quad (2.24)$$

where subscripts '*B*', '*e*', '*ph*', and '*(ν)*' denote the components of baryons, electrons and positrons, photons, and trapped-neutrinos (for ν_e , $\bar{\nu}_e$, and ν_x , see § 2.2.2), respectively. Our treatment of the EOS is summarized in § 2.3.1.

The Euler equation ($\gamma_i^\alpha \nabla_\beta T^\beta_\alpha = -\gamma_i^\alpha Q_\alpha^{\text{leak}}$), and the energy equation ($n^\alpha \nabla_\beta T^\beta_\alpha = -n^\alpha Q_\alpha^{\text{leak}}$) can be written explicitly, in terms of $e_h \equiv T^{\alpha\beta} n_\alpha n_\beta$ and $j_i \equiv -T^{\alpha\beta} \gamma_{i\alpha} n_\beta$, as,

$$\begin{aligned} \partial_t(\sqrt{\gamma}j_i) + \partial_k \left[\sqrt{\gamma}(j_i v^k + \alpha \delta_i^k) \right] \\ = \sqrt{\gamma} \left[-e_h \partial_i \alpha + j_k \partial_i \beta^k + \frac{\alpha}{2} S^{jk} \partial_i \gamma_{jk} - \alpha Q_i^{\text{leak}} \right], \end{aligned} \quad (2.25)$$

$$\begin{aligned} \partial_t(\sqrt{\gamma}e_h) + \partial_k \left[\sqrt{\gamma}(e_h v^k + P(v^k + \beta^k)) \right] \\ = \alpha \sqrt{\gamma} \left(S^{ij} K_{ij} - \gamma^{ik} j_i \partial_k \ln \alpha + n^\mu Q_\mu^{\text{leak}} \right), \end{aligned} \quad (2.26)$$

^{*)} We note that Liebendörfer et al.⁴⁸⁾ developed a more sophisticate method in terms of the distribution functions of trapped and streaming neutrinos in the Newtonian framework.

where $w \equiv \alpha u^t$ and $v^i \equiv u^i/u^t$.

The streaming-neutrino part, on the other hand, is written in the general form of

$$(T^{\nu,S})_{\alpha\beta} = En_\alpha n_\beta + F_\alpha n_\beta + F_\beta n_\alpha + P_{\alpha\beta}, \quad (2.27)$$

where $F_\alpha n^\alpha = P_{\alpha\beta} n^\alpha = 0$. Then the evolution equations of streaming-neutrinos (E and F_i) are explicitly written as

$$\partial_t(\sqrt{\gamma}E) + \partial_k \left[\sqrt{\gamma}(\alpha F^k - \beta^k E) \right] = \sqrt{\gamma} \left(\alpha P^{kl} K_{kl} - F^k \partial_k \alpha - \alpha Q_a^{\text{leak}} n^a \right), \quad (2.28)$$

$$\begin{aligned} \partial_t(\sqrt{\gamma}F_i) + \partial_k \left[\sqrt{\gamma}(\alpha P_i^k - \beta^k F_i) \right] \\ = \sqrt{\gamma} \left(-E \partial_i \alpha + F_k \partial_i \beta^k + \frac{\alpha}{2} P^{kl} \partial_i \gamma_{kl} + \alpha Q_i^{\text{leak}} \right). \end{aligned} \quad (2.29)$$

In order to close the system, we need an explicit expression of $P_{\alpha\beta}$ (closure relation). In the current implementation, we adopt a simple form $P_{\alpha\beta} = \chi E \gamma_{\alpha\beta}$ with $\chi = 1/3$. We solve Eq. (2.18) in a high resolution shock capturing scheme.¹¹⁾

The closure relation employed in the current implementation is not very physical. Moreover we do not consider the so-called neutrino heating. To take into account the neutrino heating as well as the propagation of the streaming neutrinos accurately, a more sophisticated implementation of handling the neutrino transfer together with a better closure relation is required. However, such a study is beyond the scope of this paper. A more sophisticated implementation based on the moment method,^{49),16)} will be presented in the near future.

2.2.2. Baryon and Lepton-number conservation equations

The continuity equation for the baryon is

$$\nabla_\alpha(\rho u^\alpha) = 0, \quad (2.30)$$

which can be written explicitly as

$$\partial_t(\sqrt{\gamma}\rho w) + \partial_k(\sqrt{\gamma}\rho w v^i) = 0. \quad (2.31)$$

The conservation equations of the lepton fractions are written schematically as

$$\frac{dY_e}{dt} = \gamma_e, \quad (2.32)$$

$$\frac{dY_{\nu_e}}{dt} = \gamma_{\nu_e}, \quad (2.33)$$

$$\frac{dY_{\bar{\nu}_e}}{dt} = \gamma_{\bar{\nu}_e}, \quad (2.34)$$

$$\frac{dY_{\nu_x}}{dt} = \gamma_{\nu_x}, \quad (2.35)$$

where Y_e , Y_{ν_e} , $Y_{\bar{\nu}_e}$, and Y_{ν_x} denote the fractions per baryon number for electrons, electron neutrinos (ν_e), electron anti-neutrinos ($\bar{\nu}_e$), and *total* of μ and τ neutrinos and anti-neutrinos (ν_x), respectively. Note that only the trapped-neutrinos are responsible for these neutrino fractions.

Using the continuity equation for the baryon, we rewrite the conservation equations of the lepton fractions in the following form as

$$\partial_t(\sqrt{\gamma}\rho w Y_{(L)}) + \partial_k(\sqrt{\gamma}\rho w Y_{(L)} v^k) = \sqrt{\gamma}\alpha\rho\gamma_{(L)}, \quad (2.36)$$

where $Y_{(L)}$ and $\gamma_{(L)}$ are abbreviated expressions of the lepton fractions and the source terms.

The source terms are given by

$$-\gamma_e = \gamma_{\nu_e}^{\text{local}} - \gamma_{\bar{\nu}_e}^{\text{local}}, \quad (2.37)$$

$$\gamma_{\nu_e} = \gamma_{\nu_e}^{\text{local}} - \gamma_{\nu_e}^{\text{leak}}, \quad (2.38)$$

$$\gamma_{\bar{\nu}_e} = \gamma_{\bar{\nu}_e}^{\text{local}} - \gamma_{\bar{\nu}_e}^{\text{leak}}, \quad (2.39)$$

$$\gamma_{\nu_x} = \gamma_{\nu_x}^{\text{local}} - \gamma_{\nu_x}^{\text{leak}}, \quad (2.40)$$

where γ^{local} 's and γ^{leak} 's are rates of the local production and leakage for each species of neutrinos, respectively. As local reactions, we consider the electron capture, the positron capture, electron-positron pair annihilation, plasmon decay, and the Bremsstrahlung radiation of pair neutrinos (see § 2.3.2 for definitions and details). Because γ^{local} 's are characterized by the timescale of weak-interaction processes t_{wp} , we follow the procedure proposed in Ref. 11) to stably solve the equations with a usual timestep ($\Delta t \approx 0.4\Delta x$) in an explicit manner (see Fig. 1).

1. At each timestep n , we first solve the conservation equation of the *total* lepton fraction ($Y_l = Y_e + Y_{\nu_e} - Y_{\bar{\nu}_e}$),

$$\frac{dY_l}{dt} = \gamma_l = -(\gamma_{\nu_e}^{\text{leak}} - \gamma_{\bar{\nu}_e}^{\text{leak}}), \quad (2.41)$$

instead of solving Eqs. (2.32)–(2.34), together with Eqs. (2.31), (2.25)–(2.29), and (2.35). Note that the source term in Eq. (2.41) is characterized by the leakage timescale and can be solved explicitly. In this step, we assume that the β -equilibrium condition is achieved, and the source terms are modified according to this assumption. After the time integration, the lepton fractions in the 'hypothetical' β -equilibrium (Y_e^β , $Y_{\nu_e}^\beta$, and $Y_{\bar{\nu}_e}^\beta$) are calculated from the evolved Y_l .

2. We next solve the whole set of the equations (Eqs. (2.31), (2.25)–(2.29), and (2.32)–(2.35)). In this step, we first calculate the maximum allowed values of the source terms, $\gamma_{\nu_e, \text{max}}^{\text{local}}$ and $\gamma_{\bar{\nu}_e, \text{max}}^{\text{local}}$, regarding that $Y_{\nu_e}^\beta$ and $Y_{\bar{\nu}_e}^\beta$ as the maximum allowed values of the neutrino fractions at the next timestep $n+1$. Then the source terms are limited according to

$$\gamma_{\nu_e}^{\text{local}} = \min \left[\gamma_{\nu_e}^{\text{local}}, \gamma_{\nu_e, \text{max}}^{\text{local}} \right], \quad (2.42)$$

$$\gamma_{\bar{\nu}_e}^{\text{local}} = \min \left[\gamma_{\bar{\nu}_e}^{\text{local}}, \gamma_{\bar{\nu}_e, \text{max}}^{\text{local}} \right], \quad (2.43)$$

$$Q_{\nu_e}^{\text{local}} = \min \left[Q_{\nu_e}^{\text{local}}, Q_{\nu_e}^{\text{local}} (\gamma_{\nu_e, \text{max}}^{\text{local}} / \gamma_{\nu_e}^{\text{local}}) \right], \quad (2.44)$$

$$Q_{\bar{\nu}_e}^{\text{local}} = \min \left[Q_{\bar{\nu}_e}^{\text{local}}, Q_{\bar{\nu}_e}^{\text{local}} (\gamma_{\bar{\nu}_e, \text{max}}^{\text{local}} / \gamma_{\bar{\nu}_e}^{\text{local}}) \right]. \quad (2.45)$$

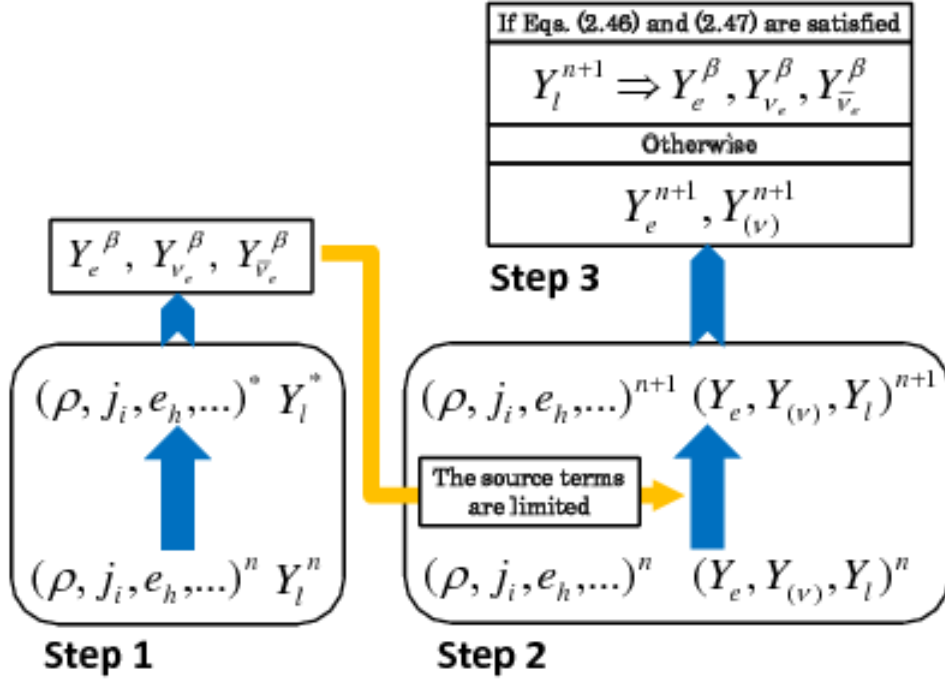


Fig. 1. A schematic picture of the leakage scheme. See text for details.

These limiter procedures enable us to solve the equations in an explicit manner.

3. After the evolution, following conditions are checked,

$$\mu_p + \mu_e < \mu_n + \mu_{\nu_e}, \quad (2.46)$$

$$\mu_n - \mu_e < \mu_p + \mu_{\bar{\nu}_e}, \quad (2.47)$$

where μ_p , μ_n , μ_e , μ_{ν_e} , and $\mu_{\bar{\nu}_e}$ are the chemical potentials of protons, neutrons, electrons, electron neutrinos, and electron anti-neutrinos, respectively. If both conditions are satisfied, the values of the lepton fractions at the timestep $n+1$ are reset to be those in the β -equilibrium value; Y_e^β , $Y_{\nu_e}^\beta$, and $Y_{\bar{\nu}_e}^\beta$.

2.3. Microphysics

2.3.1. Equation of state

We employ two versions of Shen's EOS. One is a purely nucleonic EOS,⁹⁾ which is adopted both in stellar core collapse simulations (see § 3) and in BNS merger simulations (see § 4). In the BNS merger simulation, we also adopt an EOS in which effects of Λ hyperons are taken into account²⁵⁾ (hereafter, referred to as Hyp-EOS). These EOS are tabulated in terms of the rest-mass density (ρ), temperature (T), and Y_e or Y_l .

Shen-EOS, derived from a relativistic mean-field theory,⁵⁰⁾ is a stiff one among many other EOS, giving a large maximum gravitational mass of zero-temperature spherical neutron stars $M_{\max} \approx 2.2M_\odot$. By contrast, $M_{\max} \approx 1.8M_\odot$ for Hyp-EOS

because the appearance of hyperons softens the EOS. The latest discovery of a high-mass neutron star with mass $1.97 \pm 0.04 M_\odot$ ⁵¹⁾ suggests that stiff EOS are favored, and Shen-EOS satisfies this requirement whereas Hyp-EOS does not. However, we consider that Hyp-EOS is a viable candidate for the neutron-star EOS except for a very high density that an only high-mass neutron star of $M \lesssim M_{\text{max}}$ has. We note that the neutron star in the BNS and a hypermassive neutron star (HMNS) studied here do not have the extremely high density (except for the HMNS just before the collapse to a BH).

The thermodynamical quantities of a dense matter at various sets of (ρ, Y_p, T) are calculated to construct the numerical data table for simulations. Here Y_p is the total proton fraction per baryon number. The original table covers a range of density $10^{5.1} - 10^{15.4} \text{ g/cm}^3$, proton fraction 0.0–0.56, and temperature 0–100 MeV, which are sufficient parameter ranges for supernova simulations. The original table has been extended to a higher density ($10^{5.1} - 10^{17} \text{ g/cm}^3$)^{52), 25)} and a higher temperature (0–400 MeV),^{53), 25)} for following the BH formation.

It should be noted that the causality is guaranteed to be satisfied in this framework, whereas the sound velocity sometimes exceeds the speed of the light in the non-relativistic framework, e.g., in the EOS by Lattimer and Swesty.²⁰⁾ This is one of the benefits of the relativistic EOS.

To consistently calculate the pressure and the internal energy of electrons and positrons, the charge neutrality condition $Y_p = Y_e$ has to be solved to determine the electron chemical potential μ_e for a given set of ρ and T in the EOS table. Namely, it is required to solve the equation

$$n_e(\mu_e, T) \equiv n_- - n_+ = \frac{\rho Y_e}{m_u} \quad (2.48)$$

in terms of μ_e for given values of ρ , T , and $Y_e (= Y_p)$. Here, $m_u = 931.49432 \text{ MeV}$ is the atomic mass unit, and n_- and n_+ are the total number densities (i.e., including electron-positron pairs) of electrons and positrons, respectively. Then, assuming that electrons and positrons obey the Fermi-Dirac distribution, the number density, the pressure, and the internal energy density of electrons and positrons are calculated.⁵⁴⁾

The pressure and the specific internal energy density of photons are given by

$$P_{ph} = \frac{a_r T^4}{3}, \quad \varepsilon_{ph} = \frac{a_r T^4}{\rho}, \quad (2.49)$$

where $a_r = (\pi^2 k_B^4)/(15c^3 \hbar^3)$ is the radiation constant.

In our leakage scheme, the trapped-neutrinos are assumed to interact sufficiently frequently with the matter that be thermalized, and hence, they are described as ideal Fermi gases with the matter temperature. From the numerically evolved trapped-neutrino fractions $Y_{(\nu)}$ (ν_e , $\bar{\nu}_e$, and ν_x are abbreviated by (ν)), the chemical potentials of the trapped-neutrinos ($\mu_{(\nu)}$) are calculated by solving

$$Y_{(\nu)} = \frac{m_u}{\rho} n_{(\nu)}(\mu_{(\nu)}, T), \quad (2.50)$$

where $n_{(\nu)}$ is the number density of the trapped-neutrinos. Then the pressure and

the internal energy of the trapped-neutrinos are calculated in the same manner as for electrons, using $\mu_{(\nu)}$ and the matter temperature.

In the high-resolution shock-capturing scheme for hydrodynamics, we in general need to evaluate the sound velocity c_s ,

$$c_s^2 = \frac{1}{h} \left[\frac{\partial P}{\partial \rho} \Big|_{\epsilon} + \frac{P}{\rho} \frac{\partial P}{\partial \epsilon} \Big|_{\rho} \right]. \quad (2.51)$$

Here, the derivatives of the pressure are calculated by

$$\frac{\partial P}{\partial \rho} \Big|_{\epsilon} = \sum_i \left[\frac{\partial P_i}{\partial \rho} \Big|_T - \frac{\partial P_i}{\partial T} \Big|_{\rho} \left(\sum_j \frac{\partial \epsilon_j}{\partial \rho} \Big|_T \right) \left(\sum_k \frac{\partial \epsilon_k}{\partial T} \Big|_{\rho} \right)^{-1} \right], \quad (2.52)$$

$$\frac{\partial P}{\partial \epsilon} \Big|_{\rho} = \left(\sum_i \frac{\partial P_i}{\partial T} \Big|_{\rho} \right) \left(\sum_j \frac{\partial \epsilon_j}{\partial T} \Big|_{\rho} \right)^{-1}, \quad (2.53)$$

where the sum is taken over B, e, ph and (ν) .

2.3.2. Weak-interaction and leakage rates

The leakage rates are phenomenologically defined by¹¹⁾

$$Q_{\alpha}^{\text{leak}} \equiv \sum_{(\nu)} Q_{(\nu)}^{\text{leak}} u_{\alpha} = \sum_{(\nu)} \left[(1 - e^{-b\tau_{(\nu)}}) Q_{(\nu)}^{\text{diff}} + e^{-b\tau_{(\nu)}} Q_{(\nu)}^{\text{local}} \right] u_{\alpha}, \quad (2.54)$$

$$\gamma_{(\nu)}^{\text{leak}} = (1 - e^{-b\tau_{(\nu)}}) \gamma_{(\nu)}^{\text{diff}} + e^{-b\tau_{(\nu)}} \gamma_{(\nu)}^{\text{local}}, \quad (2.55)$$

where $\tau_{(\nu)}$ is the optical depth of neutrinos and b is a parameter which is typically set to be $b^{-1} = 2/3^*$. Note that $Q_{(\nu)}^{\text{leak}}$ should be regarded as the emissivity of neutrinos measured in the *fluid rest frame* so that we set $Q_{\alpha}^{\text{leak}} = Q_{(\nu)}^{\text{leak}} u_{\alpha}$.^{55), 11)}

The optical depth is calculated by^{21), 22)}

$$\tau_{(\nu)} = \min \left[\tau_{(\nu)}^x, \tau_{(\nu)}^z, \tau_{(\nu)}^{qr} \right], \quad (2.56)$$

$$\tau_{(\nu)} = \min \left[\tau_{(\nu)}^x, \tau_{(\nu)}^y, \tau_{(\nu)}^z \right], \quad (2.57)$$

for axisymmetric (see § 3) and three-dimensional (see § 4) simulations, respectively. Here $\tau_{(\nu)}^x$, $\tau_{(\nu)}^y$, $\tau_{(\nu)}^z$, and $\tau_{(\nu)}^{qr}$ are the optical depths along x , y , z , and a 'quasi-radial' directions from each grid point, respectively. We calculate, for example, $\tau_{(\nu)}^z$ by^{**)}.

$$\tau_{(\nu)}^z(\varpi, z) = E_{(\nu)}(\varpi, z)^2 \tilde{\tau}^z(\varpi, z), \quad (2.58)$$

$$\tilde{\tau}^z(\varpi, z) = \int_z^{z_{\text{out}}} \tilde{\kappa}(\varpi, z') dz', \quad (2.59)$$

^{*)} We again used an abbreviation (ν) for ν_e , $\bar{\nu}_e$, and ν_x

^{**)} $\tau_{(\nu)}^{\varpi}$ and $\tau_{(\nu)}^r$ are calculated in a similar manner.

where z_{out} denotes the outer boundary in the z -direction. $\tilde{\kappa} (= \kappa_{(\nu)}/E_{(\nu)}^2)$ is an 'opacity' in which the neutrino-energy dependence is factored out (see Appendix C).

The neutrino energy is determined by

$$E_{(\nu)} = (1 - e^{-\tau_{(\nu)}/c})E_{(\nu)}^{\text{diff}} + e^{-\tau_{(\nu)}/c}E_{(\nu)}^{\text{local}}, \quad (2.60)$$

where we set the parameter as $c = 5$, which implies that it takes about three collisions to thermalize a neutrinos.⁵⁶⁾ Note that $\tau_{(\nu)}$ depends on the neutrino energy $E_{(\nu)}$ and we solve this equation by the Newton-Raphson method. $E_{(\nu)}^{\text{diff}}$ and $E_{(\nu)}^{\text{local}}$ are the average (thermalized) diffusion and local-production energy, which are given respectively by,

$$E_{(\nu)}^{\text{diff}} = k_B T \frac{F_3(\mu_{(\nu)}/k_B T)}{F_3(\mu_{(\nu)}/k_B T)}, \quad (2.61)$$

$$E_{(\nu)}^{\text{local}} = \frac{m_u}{\rho} \frac{Q_{(\nu)}^{\text{local}}}{\gamma_{(\nu)}^{\text{local}}}, \quad (2.62)$$

where $F_k(x)$ is the Fermi-Dirac integral.

As the local production reactions of neutrinos, we consider the electron and positron captures ($\gamma_{\nu_e}^{\text{ec}}$ and $\gamma_{\bar{\nu}_e}^{\text{pc}}$),⁵⁷⁾ the electron-positron pair annihilation ($\gamma_{\nu_e \bar{\nu}_e}^{\text{pair}}$ for electron-type neutrinos and $\gamma_{\nu_x \bar{\nu}_x}^{\text{pair}}$ for other types),⁵⁸⁾ the plasmon decays ($\gamma_{\nu_e \bar{\nu}_e}^{\text{plas}}$ and $\gamma_{\nu_x \bar{\nu}_x}^{\text{plas}}$),²¹⁾ and the Bremsstrahlung processes ($\gamma_{\nu_e \bar{\nu}_e}^{\text{Brems}}$ and $\gamma_{\nu_x \bar{\nu}_x}^{\text{Brems}}$).⁵⁹⁾ Then, the local reaction rates for the neutrino fractions are

$$\gamma_{\nu_e}^{\text{local}} = \gamma_{\nu_e}^{\text{ec}} + \gamma_{\nu_e \bar{\nu}_e}^{\text{pair}} + \gamma_{\nu_e \bar{\nu}_e}^{\text{plas}} + \gamma_{\nu_e \bar{\nu}_e}^{\text{Brems}}, \quad (2.63)$$

$$\gamma_{\bar{\nu}_e}^{\text{local}} = \gamma_{\bar{\nu}_e}^{\text{pc}} + \gamma_{\nu_e \bar{\nu}_e}^{\text{pair}} + \gamma_{\nu_e \bar{\nu}_e}^{\text{plas}} + \gamma_{\nu_e \bar{\nu}_e}^{\text{Brems}}, \quad (2.64)$$

$$\gamma_{\nu_x}^{\text{local}} = 4(\gamma_{\nu_x \bar{\nu}_x}^{\text{pair}} + \gamma_{\nu_x \bar{\nu}_x}^{\text{plas}} + \gamma_{\nu_x \bar{\nu}_x}^{\text{Brems}}). \quad (2.65)$$

Similarly, the local neutrino energy emission rate $Q_{(\nu)}^{\text{local}}$ is given by

$$Q_{\nu_e}^{\text{local}} = Q_{\nu_e}^{\text{ec}} + (Q_{\nu_e \bar{\nu}_e}^{\text{pair}} + Q_{\nu_e \bar{\nu}_e}^{\text{plas}} + Q_{\nu_e \bar{\nu}_e}^{\text{Brems}}), \quad (2.66)$$

$$Q_{\bar{\nu}_e}^{\text{local}} = Q_{\bar{\nu}_e}^{\text{pc}} + (Q_{\nu_e \bar{\nu}_e}^{\text{pair}} + Q_{\nu_e \bar{\nu}_e}^{\text{plas}} + Q_{\nu_e \bar{\nu}_e}^{\text{Brems}}), \quad (2.67)$$

$$Q_{\nu_x}^{\text{local}} = 4(Q_{\nu_x \bar{\nu}_x}^{\text{pair}} + Q_{\nu_x \bar{\nu}_x}^{\text{plas}} + Q_{\nu_x \bar{\nu}_x}^{\text{Brems}}). \quad (2.68)$$

The explicit forms of the local rates in Eqs. (2.63)–(2.68) are summarized in Appendices A and B (see also, Ref. 11)).

We follow the recent work by Rosswog and Liebendörfer²²⁾ for the diffusive neutrino emission rates $\gamma_{(\nu)}^{\text{diff}}$ and $Q_{(\nu)}^{\text{diff}}$ in Eqs. (2.54) and (2.55). The explicit forms of $\gamma_{(\nu)}^{\text{diff}}$ and $Q_{(\nu)}^{\text{diff}}$ are described in Appendix C (see also, Ref. 11)).

2.4. Recover of $(\rho, Y_e/Y_l, T)$

The quantities numerically evolved in the hydrodynamic equations are the conserved quantities: $\sqrt{\gamma}\rho w$, $\sqrt{\gamma}\rho w Y_L$, $\sqrt{\gamma}j_i$, and $\sqrt{\gamma}e_h$. The argument variables, $(\rho, (Y_e \text{ or } Y_l), T)$, of the EOS table, together with $w = \alpha u^t = \sqrt{1 + \gamma^{ij}u_i u_j}$, should be

calculated from the conserved quantities at each timestep. Note that $\sqrt{\gamma}$ is readily given by numerical evolution of Einstein's equations. Also, the lepton fractions (Y_L) can be calculated directly from the conserved quantities.

2.4.1. Non- β -equilibrium case

In the case that the β -equilibrium condition is not satisfied, the argument quantities (ρ , Y_e , T) can be reconstructed from the conserved quantities in the following straightforward manner.

1. Give a trial value of w , referred to as \tilde{w} . Then, one obtains a trial value of the rest mass density $\tilde{\rho}$.
2. A trial value of the temperature, \tilde{T} , can be obtained from the numerically evolved value of e_h , by solving the following equation:

$$e_h - \sum_{(\nu)} e_{h,(\nu)}(\tilde{\rho}, Y_{(\nu)}\tilde{T}) = e_{h,\text{EOS}}(\tilde{\rho}, Y_e, \tilde{T}). \quad (2.69)$$

Here, $e_{h,\text{EOS}}(\tilde{\rho}, Y_e, \tilde{T}) \equiv \tilde{\rho}\tilde{w}^2 h_{\text{EOS}}(\tilde{\rho}, Y_e, \tilde{T}) - P(\tilde{\rho}, Y_e, \tilde{T})$ should be evaluated from the EOS table which does not include the contributions of trapped-neutrinos. In the left-hand-side, $e_{h,(\nu)}$ is the trapped-neutrino part. Note that one dimensional search over the EOS table is required to obtain \tilde{T} .

3. The next trial value of w is given by

$$\tilde{w} = \sqrt{1 + \gamma^{kl} \left(\frac{j_k}{\tilde{\rho}\tilde{w}h_{\text{EOS}}} \right) \left(\frac{j_l}{\tilde{\rho}\tilde{w}h_{\text{EOS}}} \right)}. \quad (2.70)$$

4. Repeat the procedures (1)–(3) until a required degree of convergence is achieved. Convergent solutions of the temperature and w are obtained typically within 10 iterations.

2.4.2. The β -equilibrium case

In the case that the β -equilibrium condition is satisfied, on the other hand, we may reconstruct the argument quantities (ρ , Y_e , T) from the conserved quantities and Y_l , under the assumption of the β -equilibrium. In this case, two-dimensional recover (Y_l, e_h) \implies (Y_e, T) would be required for a given value of \tilde{w} . In this case, there may be more than one combination of (Y_e , T) which gives the same values of Y_l and e_h . Therefore, we have to adopt a different method to recover (ρ , Y_e , T). Under the assumption of the β -equilibrium, the electron fraction is related to the total lepton fraction: $Y_e = Y_e(\rho, Y_l, T)$. Using this relation, the EOS table can be rewritten in terms of the argument variables of (ρ , Y_l , T). Then, the similar strategy as in the non- β -equilibrium case can be adopted. Namely,

1. Give a trial value \tilde{w} . Then one obtains a trial value of the rest mass density.
2. A trial value of the temperature can be obtained by solving

$$e_h = e_{\text{EOS}}^\beta(\tilde{\rho}, Y_l, \tilde{T}) \quad (2.71)$$

with one dimensional search over the EOS table. Here e_{EOS}^β should be evaluated from the β -equilibrium EOS table, which contains the trapped-neutrino

contributions.

3. The next trial value of w is given in the same way.
4. Repeat the procedures (1)–(3) until a required degree of convergence is achieved. The electron fraction is given as $Y_e = Y_e(\rho, Y_l, T)$ in the β -equilibrium EOS table.

In the case of a simplified or analytic EOS, the Newton-Raphson method may be applied to recover the primitive variables. In the case of a tabulated EOS, by contrast, the Newton-Raphson method may not be a good approach because it requires derivatives of thermodynamical quantities which in general cannot be calculated precisely from a tabulated EOS by the finite differentiating method.

§3. Gravitational collapse of massive stellar core

The observational associations (for a review, see Ref. 60)) between LGRBs and supernovae has provided the strong support to a scenario, so-called collapsar model, in which LGRBs are assumed to be driven in the collapse of a massive stellar core to a BH.^{61),62)} In the collapsar model, a central core of a massive star is required to be rotating rapidly enough that a massive accretion disk can be formed around a BH.

Because the observed supernovae associated with LGRBs are Type Ib/c and the relativistic jets have to reach the stellar surface,⁶³⁾ the progenitors should have lost their hydrogen (and helium) envelopes before the onset of the stellar core collapse; otherwise a peculiar evolution path is required. Due to these reasons, the progenitors of LGRBs are now believed to be rotating massive Wolf-Rayet (WR) stars. However, ordinary WR stars are known to be accompanied by strong stellar winds driven by the radiation pressure which cause a rapid spin-down of the stellar core. Here, a serious problem concerning the collapsar model is that according to stellar evolution calculations, it is very difficult to produce pre-collapse cores which satisfy both the requirement of the collapsar model and the association of Type Ib/c supernova, if magnetic torques and standard mass-loss rates are taken into account.⁶⁴⁾

To resolve the above dilemma, several models have been proposed (see Ref. 65) for a review). All of the proposed progenitor models of LGRBs are anomalous in the sense that they are different from the progenitors of ordinary supernovae (see Ref. 12) for a discussion). Qualitatively speaking, LGRB progenitor cores may be modeled by a rapidly rotating, higher-entropy core, regardless of their formation processes. Based on this assumption, we performed simulations of a massive stellar core with higher values of entropy collapsing to a BH. In this section, we report our latest results of fully general relativistic simulations for the collapse of a rotating, higher-entropy cores, performed taking into account detailed microphysics.

3.1. Initial models and grid setting

As a representative model of a high entropy core, we adopt a presupernova core of $100M_\odot$ model calculated by Umeda and Nomoto⁶⁶⁾ (hereafter denoted by UN100). The model has an iron core of a large mass $M_{\text{core}} \approx 3.2M_\odot$ and radius $R_{\text{core}} \approx 2500$ km with the central density and temperature of $\rho_c \approx 10^{9.5}$ g/cm³ and $T_c \approx 10^{10}$ K.

	$\Phi_c \leq 0.02$	$\leq \Phi_c \leq 0.044$	$\leq \Phi_c \leq 0.09$	$\leq \Phi_c \leq 0.2$	$\Phi_c \geq 0.2$
Δx_0 (km)	4.0	2.0	1.0	0.5	0.25
δ	0.0075	0.007	0.0065	0.006	0.0055
N	332	428	542	668	812
L (km)	5840	5370	5000	4450	3860
Δx_0 (km)	5.5	2.85	1.45	0.7	0.35
δ	0.0075	0.007	0.0065	0.006	0.0055
N	294	380	484	610	752
L (km)	5860	5360	4980	4370	3870

Table I. Summary of the regridding procedure. The values of the minimum grid spacing Δx_0 (in units of km), the non-uniform-grid factor δ , and the grid number N for each range of $\Phi_c = 1 - \alpha_c$ are listed for the finer and the coarser (lower table) resolutions.

The central value of entropy per baryon is $s \approx 4k_B$, which is much larger than that of an ordinary presupernova core for which $s \lesssim 1k_B$.

Because the model UN100 is non-rotating, we add rotational profiles according to⁶⁷⁾

$$\Omega(\varpi) = \Omega_0 \frac{R_0^2}{R_0^2 + \varpi^2} \mathcal{F}_{\text{cut}}, \quad (3.1)$$

where $\varpi = \sqrt{x^2 + y^2}$, Ω_0 , and R_0 are parameters which control the magnitude and degree of differential rotation. The cut-off factor \mathcal{F}_{cut} is introduced by a practical reason for the numerical simulation: If the specific angular momentum in the outer region of the core is too large, the matter escapes from the computational domain. To avoid this, the rotational velocity has to be suppressed in the outer region.

We fix the central angular velocity as $\Omega_0 = 1.2$ rad/s and consider two values of R_0 ; a rigid rotation model ($R_0 = \infty$, referred to as UN100-rigid) and a differential rotation ($R_0 = R_{\text{core}}$, referred to as UN100-diff) model. We note that the imposed rotation is moderately large (not rapid) because Ω_0 is much smaller than the Kepler value $(M_{\text{core}}/R_{\text{core}}^3)^{1/2} \approx 5.2$ rad/s.

We assume axial and equatorial symmetries of the spacetime and the so-called Cartoon method^{68),69)} is adopted for integrating Einstein's equations. In the current implementation, we use a fourth order Lagrange interpolation scheme, which is necessary in the Cartoon method.

In numerical simulations, we adopt a nonuniform grid, in which the grid spacing is increased according to the rule

$$dx_{j+1} = (1 + \delta)dx_j, \quad dz_{l+1} = (1 + \delta)dz_l, \quad (3.2)$$

where $dx_j \equiv x_{j+1} - x_j$, $dz_l \equiv z_{l+1} - z_l$, and δ is a constant. In addition, a regridding technique^{70),71)} is adopted to assign a sufficiently large number of grid points inside the collapsing core, saving the CPU time efficiently. The regridding is carried out whenever the characteristic radius of the collapsing core, defined by⁷⁰⁾ $\Phi_c \equiv 1 - \alpha_c$ ($\Phi_c > 0$) where α_c is the central value of the lapse function, decreases by a factor of ~ 2 , and we set an infalling boundary condition at the outer boundary.

All the quantities on the new grid are calculated using a fifth-order Lagrange interpolation. However, for the fluid quantities such as ρ and h , the fifth-order

interpolation could fail because the interpolation may give negative values of ρ and $h - 1$. In case we have $\rho < 0$ or $h < 1$, we adopt the linear interpolation to calculate the quantities on the new grid, based on the prescription proposed by Ref. 42). In each regridding, we solve the Hamiltonian constraint equation numerically.

To check the convergence of numerical results, simulations are performed in two different grid resolutions. Table I summarizes the regridding parameters (N and L are the number of the grid points and the computational domain, respectively) of each level of the regridding procedure for finer (upper) and coarser (lower) resolutions. The numerical results in both grid resolutions agree well except for the formation time of a BH and the stochastic behavior due to connective and turbulent motions.

3.2. Dynamical features

Figure 2(a) shows the evolution path (red curve) of central values of the rest-mass density and the temperature in the ρ - T plane for UN100-rigid. As in the core collapse of an ordinary supernova for which the central value of entropy per baryon is $s/k_B \sim 1$, gravitational collapse is triggered by the electron capture and the photo-dissociation of heavy nuclei. Because of the higher value of the entropy per baryon ($s/k_B \approx 4$), the photo-dissociation is mainly responsible to the destabilization. Note that a substantial amount of heavy nuclei are resolved into heliums by the photo-dissociation (see Fig. 2): The fraction of heavy nuclei in mass is ≈ 0.4 and 0.2 for $\rho_c = 10^{11}$ and 10^{12} g/cm³, respectively. Then the collapse in the early phase proceeds in a homologous manner. As the collapse proceeds temperature increases, heliums are resolved into free nucleons (p, n).

Figure 2(b) shows the evolution path (red curve) of central values of the rest-mass density and Y_e in the ρ - Y_e plane for UN100-rigid. Because the temperature for the present models is higher than that for the ordinary supernova, the electron capture on the free proton is enhanced due to the larger value of the free proton fraction, and hence, the electron fraction for UN100 is by ~ 0.1 smaller than that for the ordinary supernova in the collapse phase (compare the red and green curves in Fig. 2(b)).

The time evolution of the central values of the rest-mass density, electron fraction, temperature, and the lapse function for models UN100-rigid and UN100-diff is shown in Figure 3. As in the collapse of the ordinary supernova core, the collapsing core experiences a bounce when the central density reaches the nuclear density ρ_{nuc} above which the pressure increases drastically due to the repulsive nuclear force, and then, shock waves are formed and launched. Because the electron fraction at the bounce is small as $Y_e \approx 0.17$ and hence the core is neutron rich, the nuclear force starts playing a role at relatively low density, $\rho \sim 10^{14}$ g/cm³, in Shen-EOS. After the bounce, a HMNS, which is supported by a significant rotation and thermal pressure, is formed.

The shock wave formed at the core bounce propagates outward but eventually stalls at $r \approx 100$ km due the neutrino cooling and photodissociation of heavy nuclei contained in the infalling matter (see the top panels of Figs. 4 and 5). Then, a standing accretion shock is formed. As in the case of the ordinary supernova, con-

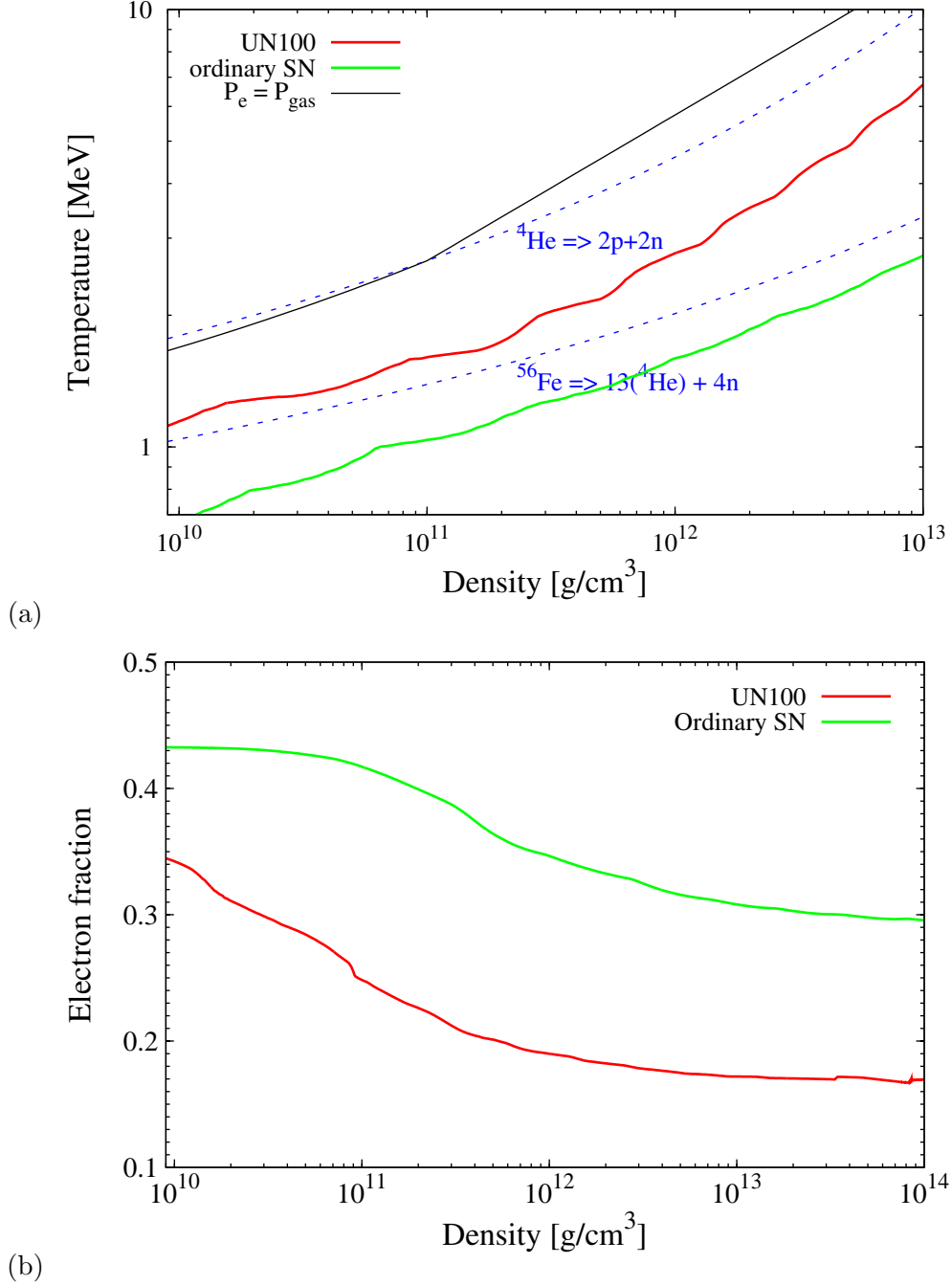


Fig. 2. (a) Evolution paths of the central values of the rest-mass density and the temperature in the ρ - T plane. The red curve shows the evolution path of UN100-rigid. The black solid curve shows the boundary at which the condition $P_e = P_{\text{gas}}$ is satisfied ($P_e > P_{\text{gas}}$ for the higher density side). The two blue dashed curves denote the values of (ρ, T) with which ^{56}Fe or ^4He will be half by mass due to the photo-dissociation. An evolution path for an ordinary supernova core¹¹⁾ is shown together for comparison (solid green curve). (b) Evolution paths of the central values of the rest-mass density and the electron fraction in the ρ - Y_e plane.

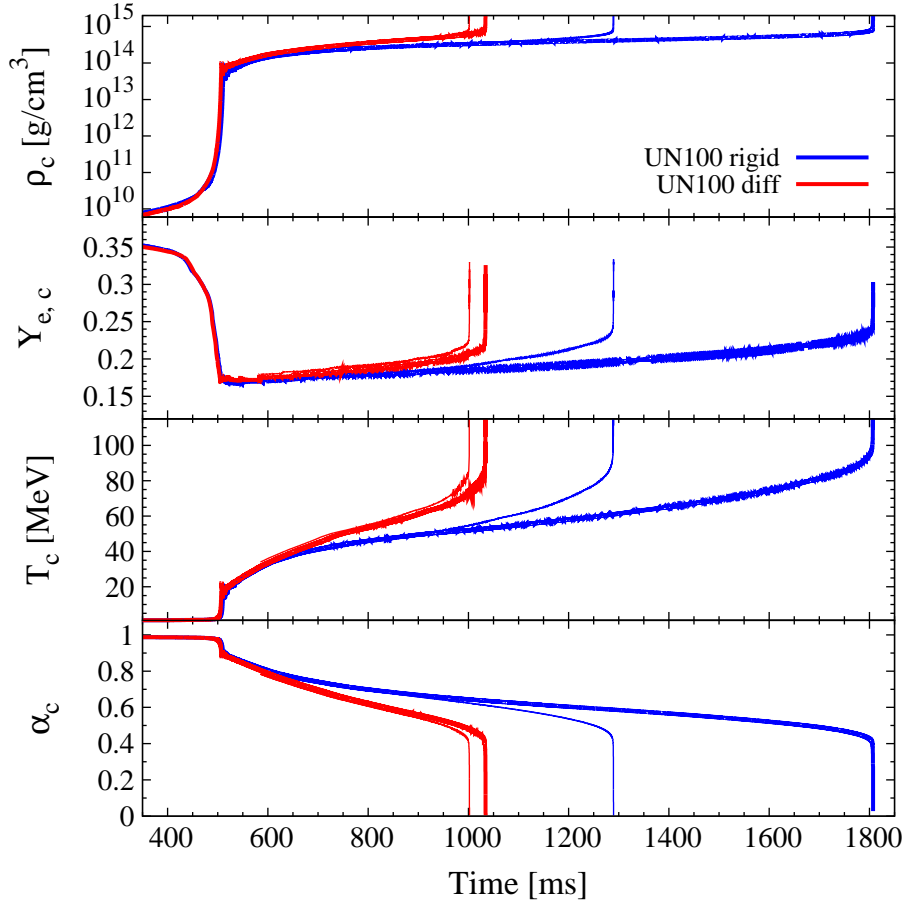


Fig. 3. Time evolution of the central values of rest-mass density, electron fraction, temperature, and the lapse function for UN100-rigid (blue curves) and UN100-diff (red curves). The results for the coarser grid resolution are shown together (thin curves). The collapsing core experiences a core bounce at $t \approx 510$ ms and collapse to a BH at $t \approx 1810$ ms.

vection is activated between the HMNS and the standing shock. However, it is not strong enough to push the standing shock outward. The convection is stronger for the differentially rotating model, which rotates more slowly than the rigidly rotating model. This is likely to be due to the stabilizing effect of the epicyclic modes which is stronger in UN100-rigid.¹²⁾ As the matter accretion proceeds, the central density and temperature increase gradually, and eventually, the HMNS collapses to a BH. The formation time of the BH depends on the grid resolution (compare the thin and thick curves in Fig. 3) in particular for UN100-rigid. This is because the HMNS is close to the marginally stable configuration, and hence, a small thermodynamical change results in a significant change in ρ . In general, for a finer grid resolution, the lifetime of HMNS increases. The longer lifetime for higher-resolution runs is a often-seen feature, because the numerical dissipation is less severe for high resolution. Note that the rotational profiles in the central region of UN100-rigid and UN100-diff

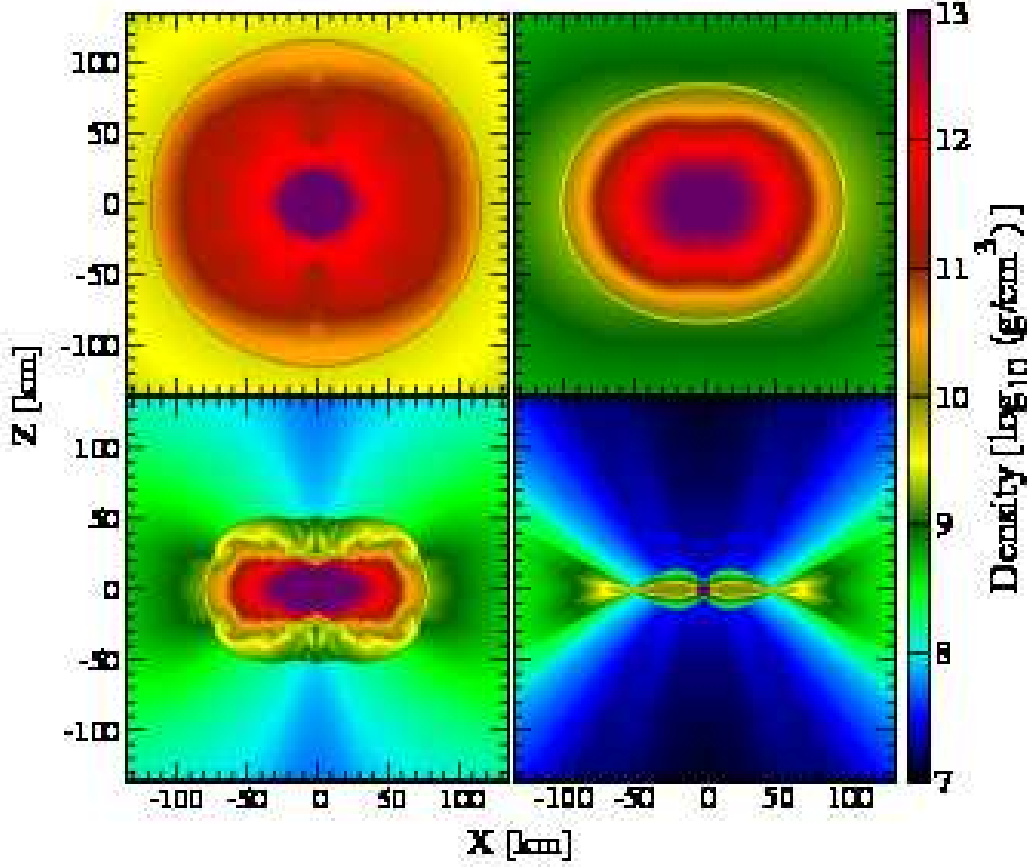


Fig. 4. Contour profiles of the rest-mass density in the x - z plane at $t = 570$ ms, (top left), 645 ms (top right), 890 ms (bottom left), and 1150 ms (bottom right) for UN100-diff.

are very similar, and their evolution process agrees well with each other soon after the core bounce. However, their evolution paths deviate as the matter in the outer region falls.

Dynamics of the system for the models UN100-diff and UN100-rigid in the later phase of the accretion onto the HMNS is qualitatively different. Figure 4 shows contour plots of the rest-mass density in the x - z plane at selected time slices for UN100-diff until the HMNS collapses to a BH. Because of the accretion of the matter, the shock front of the standing accretion shock gradually recedes. Note that the shape of the shock wave is deformed by the rotation to be spheroidal. As we shall see below, this shows a remarkable contrast with the case of UN100-rigid where the shock wave is deformed to be a torus-like shape. When the shock wave stalls, negative gradients of the entropy per baryon and of the total-lepton (electron) fraction appear because neutrinos carry away both the energy and the lepton number, as in the collapse of an ordinary presupernova core (see the bottom left panel of Fig. 4). The HMNS finally collapses to a BH due to the mass accretion, and a geometrically thin disk is formed around the BH. The system shows no violent time variability.

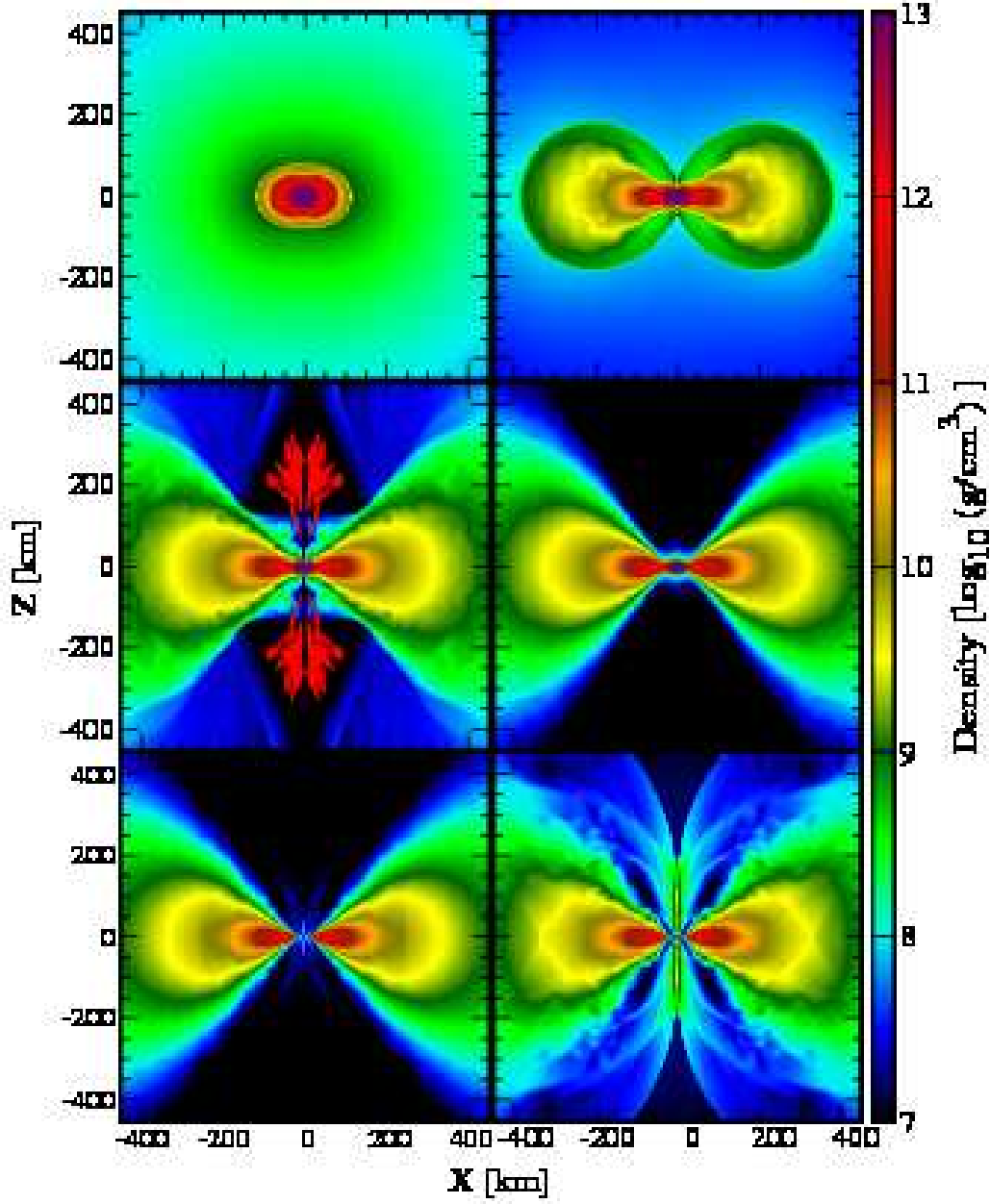


Fig. 5. Contour profiles of the rest-mass density in the x - z plane at $t = 617$ ms, (top left), 863 ms (top right), 1256 ms (middle left), 1437 ms (middle right), 1822 ms (bottom left), and 2225 ms (bottom right) for UN100-rigid. In the middle left panel, outflow velocity vectors larger than $0.15c$ are plotted together (red arrows). Note that the scale of the figure is different from that of Fig. 4. In the bottom two panels, a BH is formed at the center.

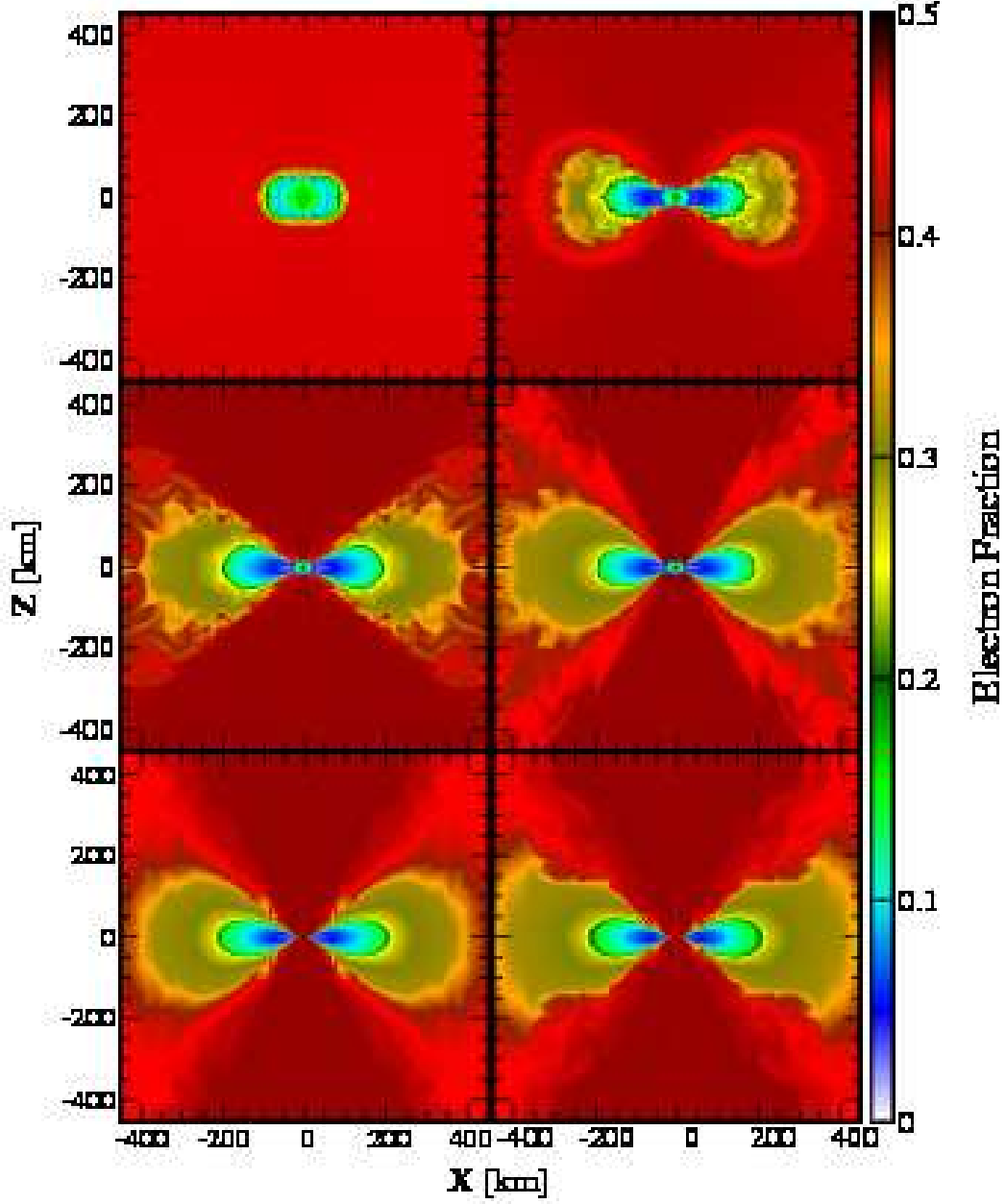


Fig. 6. Contour profiles of the electron fraction in the x - z plane at the same timeslices as Fig. 5.

Figures 5, 6, 7, and 8, respectively, show contour plots of the rest-mass density, the electron fraction, the entropy per baryon, and the temperature in the x - z plane at selected time slices for UN100-rigid. As in the model UN100-diff, the shock wave formed after the core bounce stalls at $r \sim 100$ km (the top left panel of Figs. 5–8). Due to the faster rotation of the outer region than in UN100-diff, the shock wave is deformed to be a torus-like configuration (the top right panel of Figs. 5–8).

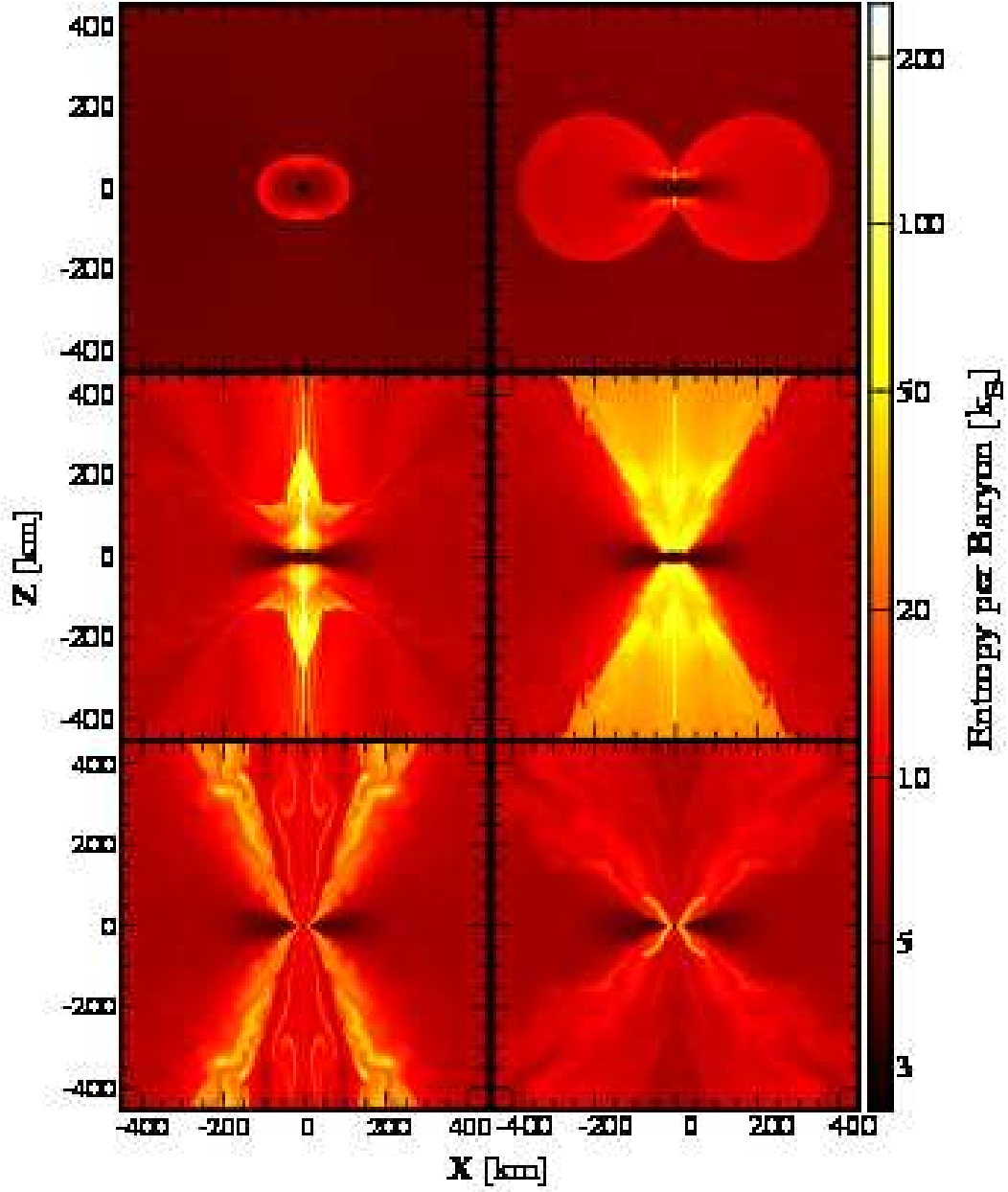


Fig. 7. Contour profiles of the entropy per baryon in the x - z plane at the same timeslices as Fig. 5.

The formation of this torus-shaped shock is the key ingredient which characterizes the dynamics of UN100-rigid. At the shock, the kinetic energy associated with the motion perpendicular to the shock surface is dissipated but that associated with the parallel component is preserved. In the model UN100-rigid, the shock front is highly deformed, and thus, the amount of the kinetic energy dissipated at the shock

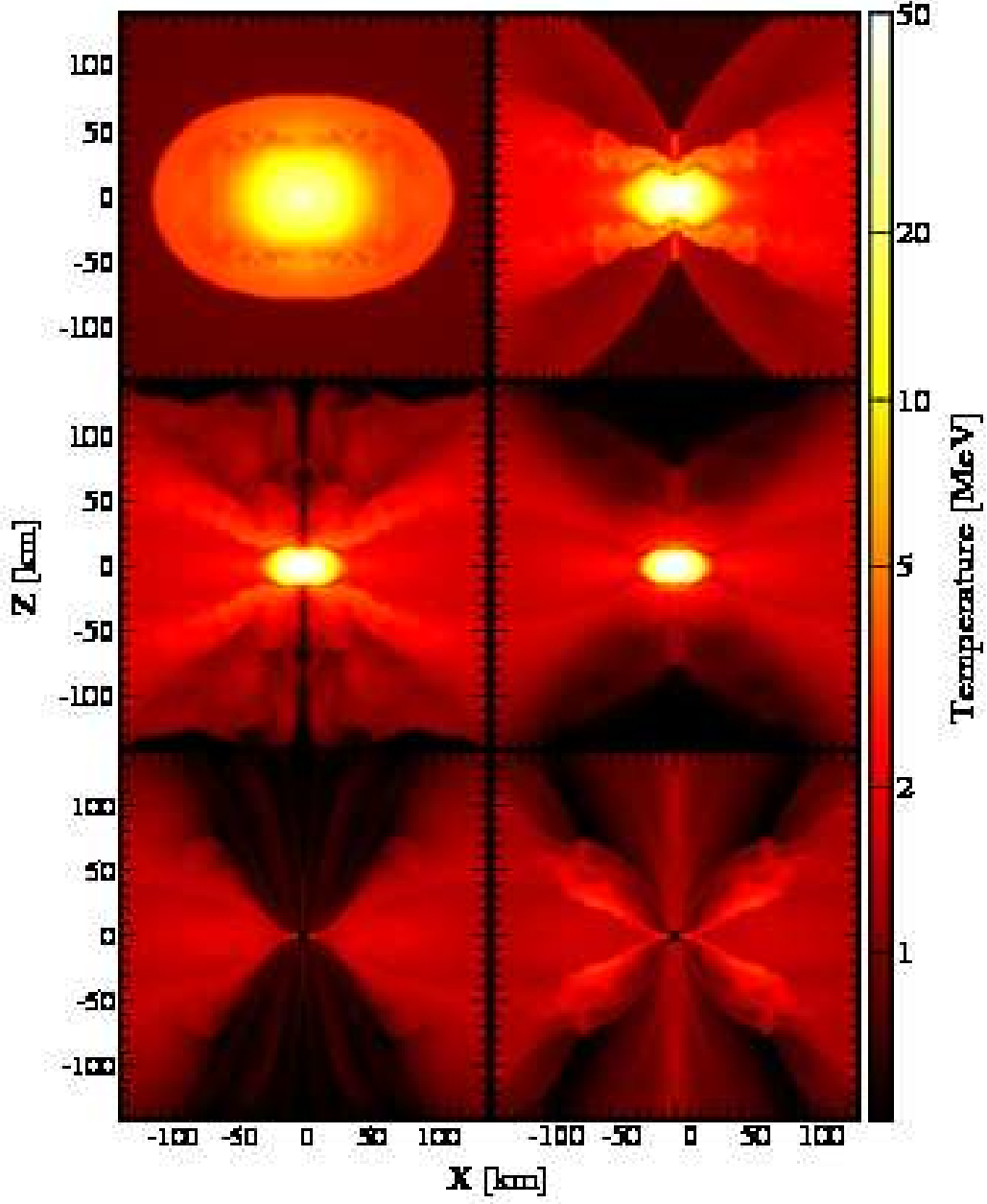


Fig. 8. Contour profiles of the temperature in the x - z plane at the same timeslices as Fig. 5 but with a different (zooming) scale.

is not as large as that in UN100-diff. This implies that the infalling materials are eventually accumulated in the central region and their kinetic energy is dissipated at the surface of the HMNS. Figure 9, which displays the velocity field in the x - z plane at a time slice, clearly shows this mechanism. During this process, oscillations of the HMNS are excited as the infalling matter hits it. Also, the shock waves gain

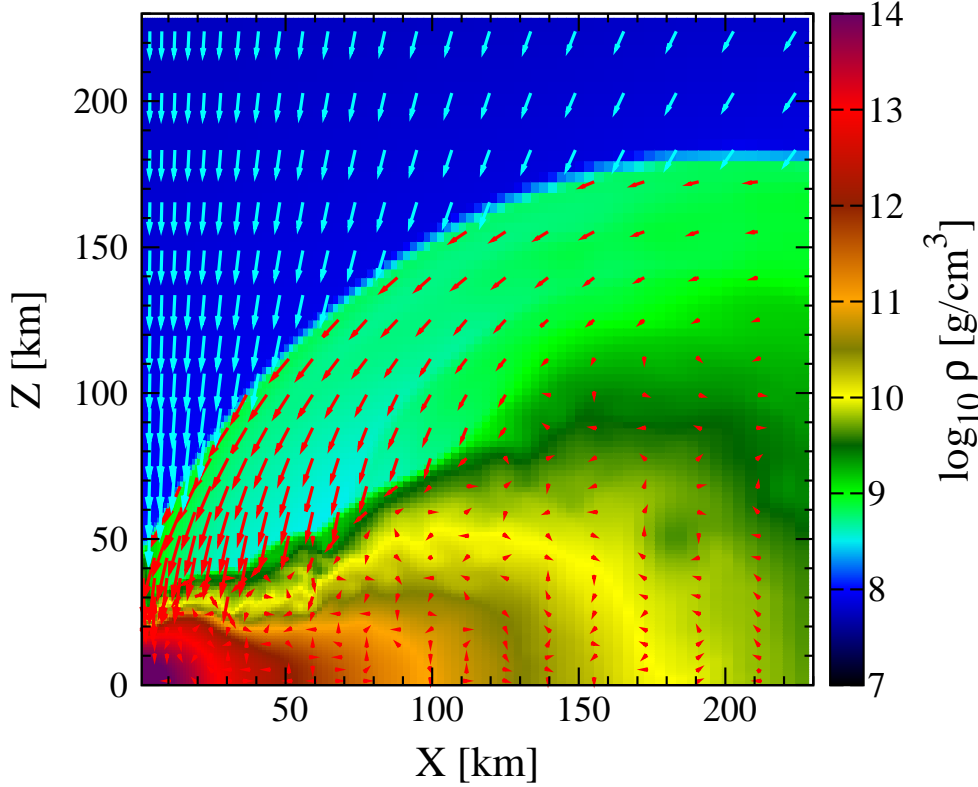


Fig. 9. Velocity vector fields outside the shock surface (blue arrows) and inside the shock (red arrows) together with a contour profile of the rest-mass density in the x - z plane at $t = 645$ ms. Only the velocity component perpendicular to the shock surface is dissipated at the shock. As a result, the infalling matter is accumulated in the central HMNS.

the thermal energy via PdV work and propagate outward.

Due to the accumulation of the matter onto the HMNS and the resulting shock heating, the thermal energy is stored in the polar region of the HMNS, increasing the gas pressure, P_{gas} , there. On the other hand, the ram pressure, P_{ram} , of the infalling matter decreases with the elapse of the time because its density decreases. When the condition, $P_{\text{ram}} < P_{\text{gas}}$, is realized, outflows are launched from the polar surface of the HMNS, forming shocks (see the middle left panel of Figs. 5–8). It can be seen that the entropy around the rotational axis is significantly enhanced due to the shock heating associated with the outflows (e.g., see the middle right panel of Fig. 7).

The outflows eventually lose the driving power by the neutrino cooling and matter again turns to fall onto the polar region of the HMNS. Due to the continuous mass accretion, the HMNS eventually collapses to a BH surrounded by a geometrically thick torus (see the bottom left panel of Figs. 5–8). Note that in the present leakage scheme, neutrino heating is not taken into account and exploring the fate of the thermally driven outflows in the presence of the neutrino heating is an in-

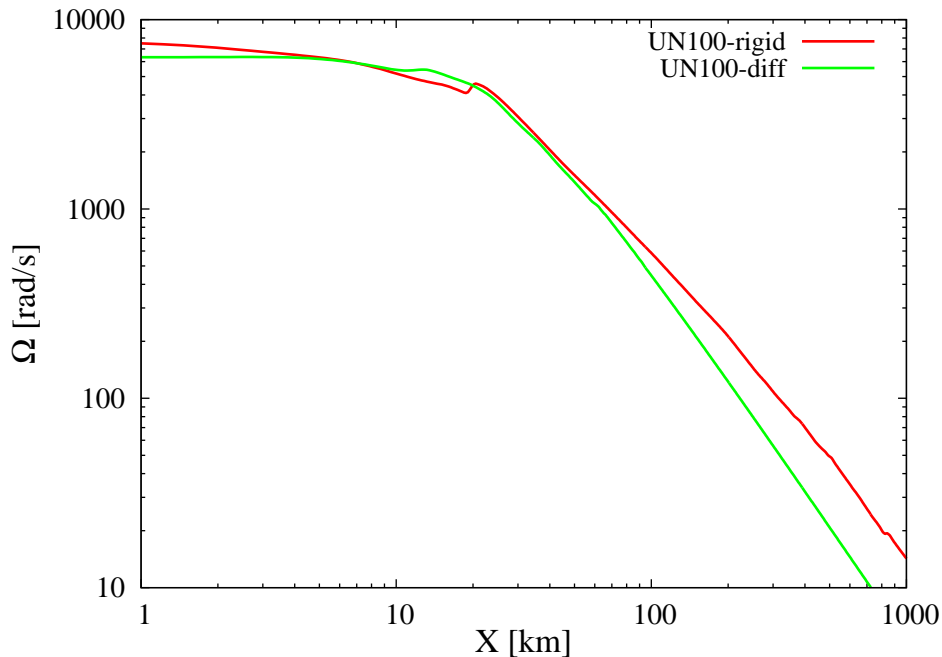


Fig. 10. Profiles of the rotational angular velocity along the equator just before the BH formation for UN100-diff (green curve) and UN100-rigid (red curve).

interesting subject. We plan to pursue this issue using a code based on the moment formalism^{49),16)} in the near future.

We found, as another novel feature of dynamics, that the BH-torus system shows a time variability (see the bottom right panel of Figs. 5–8). This is reflected in the neutrino luminosities as we shall show in § 3.3. Such a time variability has not been seen in UN100-diff. Reason for this will be explained as follows.

First, the infall timescale of the matter in the torus into the BH is longer for UN100-rigid due to the rapider rotation (in the outer region). Also, the neutrino cooling timescale for the torus will be longer for UN100-rigid because of the larger optical depth due to the higher density and temperature. Furthermore, the heating rate due to the mass accretion in the central region is larger for UN100-rigid due to the mass accumulation mechanism. Due to these reasons, the energy deposition by the accretion cannot be valanced by these cooling mechanisms: $\dot{Q}_{\text{acc}}^+ > \dot{Q}_{\text{infall}}^- + \dot{Q}_{\nu}^-$. Then the torus will expand lowering the optical depth which results in the enhancement of the neutrino cooling rate \dot{Q}_{ν}^- . Because of the strong dependence of neutrino opacities and cooling rate on the temperature, a slight change in the shock configuration may result in a huge loss of the thermal energy by neutrino emission. Here, note that the shock heated matter is partially supported by the pressure gradient due to the moderate (not very rapid) rotation. Therefore, if some materials lose their thermal energy, they will drop into the BH like an avalanche. The modulation of the shock configuration which triggers the above dropping appears to come from the Kelvin-Helmholtz instability, developed at the interface between the

torus and the accumulating flows.

In the model UN100-diff, by contrast, \dot{Q}_{acc}^+ is smaller due to the absence of the accumulation mechanism, and $\dot{Q}_{\text{infall}}^-$ and \dot{Q}_ν^- are larger due to the slower rotation. As a result, the above energy balance will be satisfied without expansion of the disk, and thus, there is no violent time variability.

It is remarkable that the above qualitative differences in dynamics between UN100-diff and UN100-rigid stem from a small difference in the initial angular velocity profile in the outer region. Figure 10 compares profiles of the rotational angular velocity along the equator just before the BH formation for UM100-diff and UM100-rigid. The rotational profiles of the HMNS ($r \lesssim 40$ km) are similar in the central region, and in the outer region, the difference at most by a factor of 2–3. This result shows that the final outcome depends strongly on the rotational profile of progenitor stars.

3.3. Neutrino Luminosity and Gravitational Waves

Figures 11(a) and 11(b) plot the time evolution of neutrino luminosities for UN100-diff. In the prebounce phase, electron neutrinos are dominantly emitted and the emissivity of electron anti-neutrinos is much smaller. This is because the electrons are (mildly) degenerate blocking the inverse β -decay and also the positron fraction, which is responsible for the anti-neutrino emission, is small. Soon after the core bounce, the so-called neutrino burst occurs at the time that the shock wave passes through the neutrino-sphere, as in the collapse of an ordinary supernova core.

After the neutrino burst, the emission of electron anti-neutrinos is enhanced and their luminosity becomes larger than that of electron neutrinos. This property is different from that in the ordinary supernova,^{72), 6)} and explained as follows. During the post neutrino burst phase, a large number of positrons are produced because the degeneracy parameter becomes low as $\eta_e \sim 1$ due to the high temperature of $T \gtrsim 20$ MeV, which is higher than the temperature in the ordinary supernova $T \sim 5$ MeV.⁷²⁾ Then, because the neutron fraction X_n is much larger than the proton fraction X_p , the positron capture on neutrons occurs more efficiently, and hence, the electron anti-neutrino luminosity becomes larger than the electron neutrino luminosity. This dominant emission of electron anti-neutrinos are also found for a HMNS formed after the BNS merger (see § 4) and in a BH-torus system formed in the collapse of a more massive core¹²⁾ with $s = 8k_B$. Both systems have a higher temperature and a lower electron fraction than the collapse of the ordinary supernova core, as in the present case.

The luminosity of μ and τ neutrinos is smaller than that of electron neutrinos and anti-neutrinos. This is simply due to the absence of the neutrino production channel mediated by the charged weak current. At later phases in the HMNS evolution ($800 \text{ ms} \lesssim t \lesssim 1100 \text{ ms}$), the electron neutrino and anti-neutrino luminosities show weak time variability. This is due to the convective activities that occur near the neutrino sphere. The μ and τ neutrino luminosity does not show the variability because they are mainly emitted by the hot central regions that do not suffer from the convection.

Soon after the BH formation at $t \approx 1090$ ms, neutrino luminosities decrease drastically because the main neutrino-emission region is swallowed into the BH. After

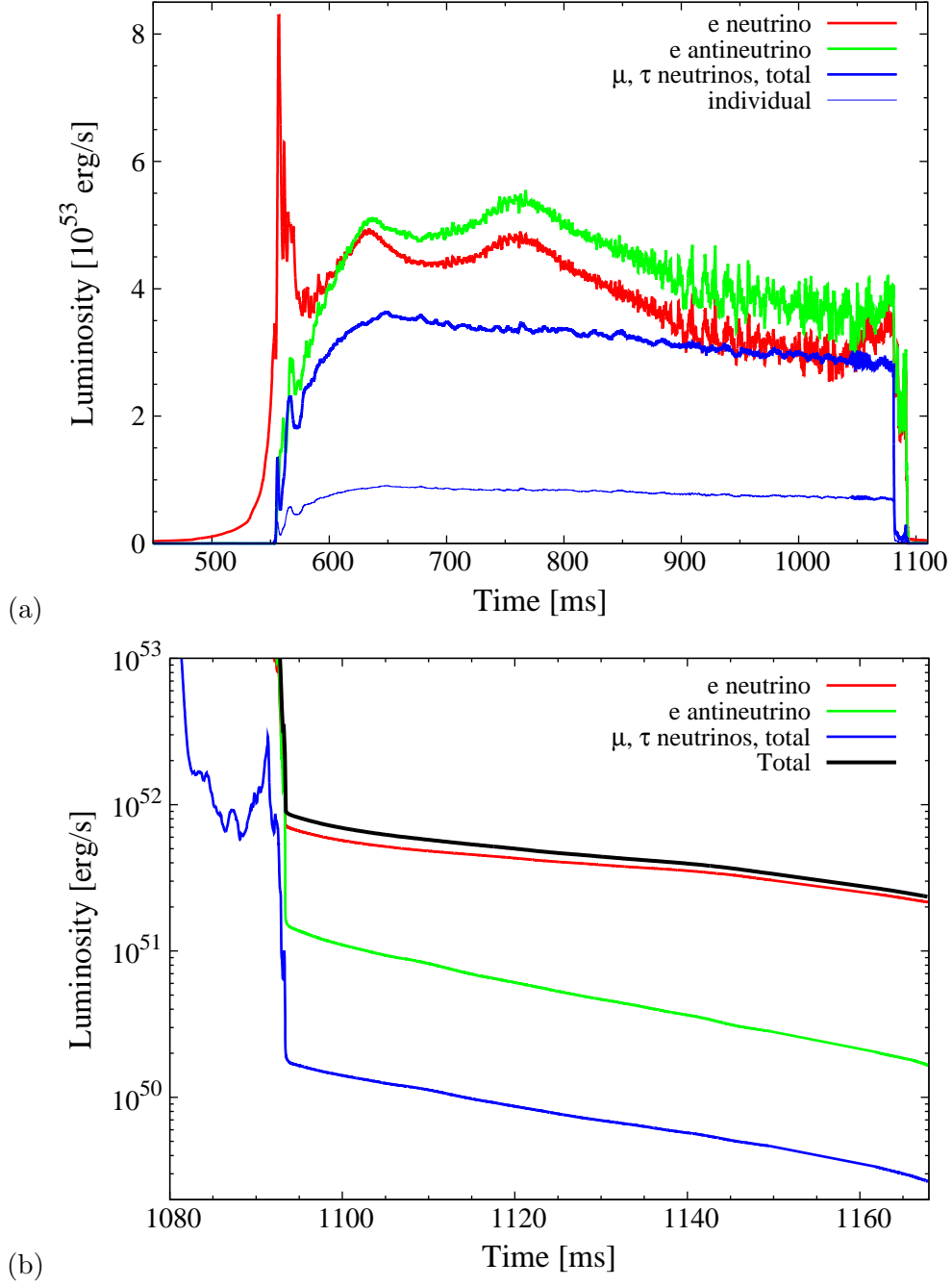


Fig. 11. Time evolution of neutrino luminosities for UN100-diff (a) before the BH formation and (b) after the BH formation. The red, green, and blue thick curves correspond to the luminosities of ν_e , $\bar{\nu}_e$, total of μ and τ pair neutrinos, respectively. The thin blue curve in the upper panel shows the luminosity of *individual* μ/τ neutrino (namely the quarter of thick blue curve). The thick black curve in the lower panel shows the total neutrino luminosity.

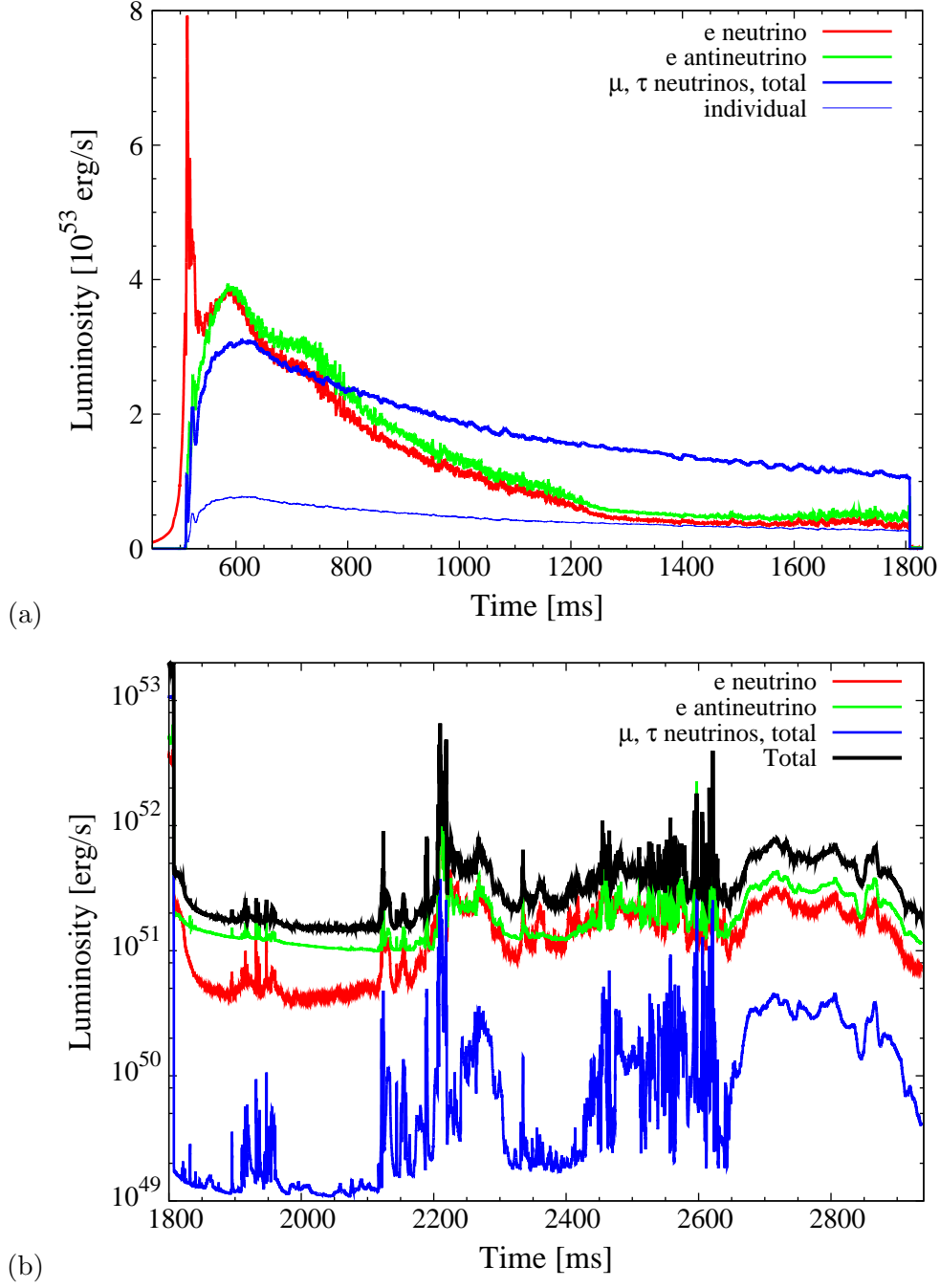


Fig. 12. Time evolution of neutrino luminosities for UN100-rigid (a) before the BH formation and (b) after the BH formation. Meanings of all curves are the same as those of Fig. 11.

that, the geometrically thin accretion disk emits $\sim 10^{51}$ – 10^{52} ergs/s by neutrinos in its early evolution phase with the duration ~ 100 ms and the luminosities decrease monotonically in time. We do not find any enhancement of the neutrino luminosities after the BH formation in our simulation time. In this phase, electron neutrinos are dominantly emitted because the disk is at a lower temperature of $T \lesssim$ a few MeV, and hence, there are less positrons. Also, the number of the target neutrons are smaller because the disk is composed mainly of proton-rich matter in the outer neutrino emission region.

Figures 12(a) and 12(b) show the time evolution of neutrino luminosities for UN100-rigid. The features of the evolution is similar to those for UN100-diff before the neutrino burst ($t \lesssim 700$ ms). After that time, the luminosities of electron neutrinos and anti-neutrinos gradually decrease. This is because the optical depth (diffusion time) gets larger (longer) as the torus grows. The luminosities of electron neutrinos and anti-neutrinos show only weak time variability, reflecting the weaker convective activity in UN100-rigid.

At $t \approx 800$ ms, the *total* luminosity of μ and τ neutrinos ($L_{\nu_\mu} + L_{\bar{\nu}_\mu} + L_{\nu_\tau} + L_{\bar{\nu}_\tau}$) becomes larger than the electron neutrino and anti-neutrino luminosities. This is partly due to a very high temperature of the neutrino sphere which enhances pair neutrino production processes, as well as a smaller optical depth along the rotational axis: Thermal neutrinos from the hot HMNS will be almost directly *seen* due to the low density along the rotational axis. Indeed, after $t \gtrsim 1300$ ms, all flavor of neutrinos and anti-neutrinos are almost equally emitted, indicating the dominant emission of thermal neutrinos from the very hot HMNS in the neutrino luminosity. This feature is not seen in the BNS merger (see § 4) and the collapse of the more massive stellar core.¹²⁾ This is because the continuous mass accretion is absent in the BNS merger and the HMNS is quickly collapses to a BH in the collapse of the more massive stellar core. At the final phase in the fallback collapse of an ordinary core (a failed supernova),⁵²⁾ an enhancement of the emission of ν_x is also seen.

Note that the above result implies that observational signals of neutrinos could depend on the viewing angle: If we would see the system from the direction along the rotational axis, we might see a brighter emission of neutrinos with a higher average energy from the hot HMNS, while we would see neutrino emissions from the torus if we see the system from the direction along the equator. In the leakage scheme adopted in this paper, unfortunately, we cannot investigate such an angle dependence of neutrino luminosities.

The neutrino luminosities show a precipitation when the BH is formed at $t \approx 1805$ ms, as in the case of UN100-diff. The total neutrino luminosity emitted from the torus around the BH amounts to $L_{\nu,\text{tot}} \sim 10^{51}$ ergs/s. A remarkable property in UN100-rigid is that this luminosity is maintained for $\gtrsim 1$ s. In addition, by contrast with the case of UN100-diff, the neutrino luminosities show a violent time variability. Such a long-term high luminosity and a time variability may be associated with the time variability that LGRBs show.

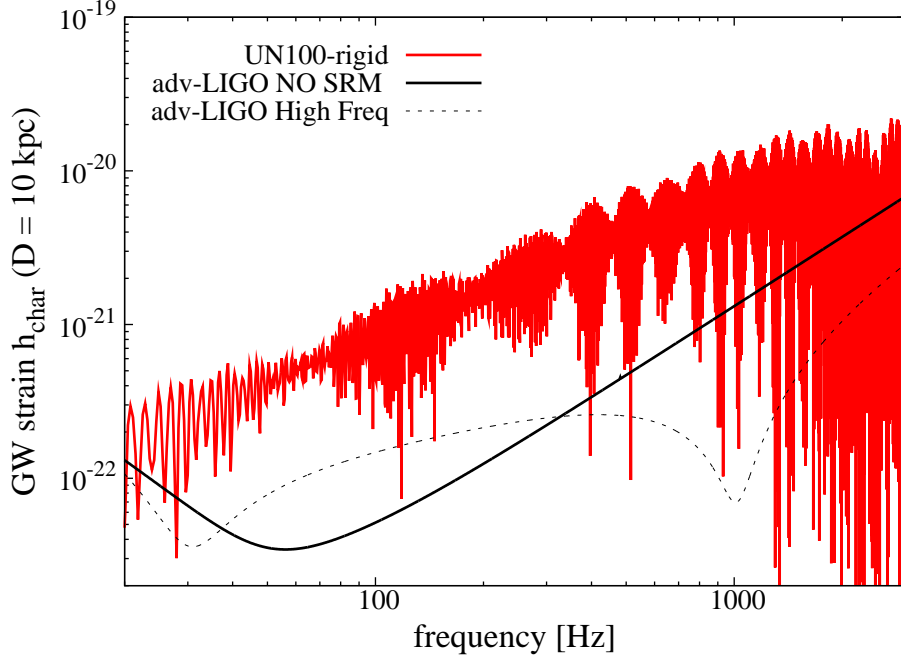


Fig. 13. The spectrum of the characteristic gravitational-wave strain for UN100-rigid. The noise amplitudes of Advanced LIGO for a version in which no signal recycling mirror is used (NO SRM) and a design with a narrow-band tuning at 1kHz (High Freq) are shown together.

Figure 13 plots the spectra of the characteristic gravitational-wave strain,⁷³⁾

$$h_{\text{char}}(f) \equiv \sqrt{\frac{2}{\pi^2} \frac{G}{c^3} \frac{1}{D^2} \frac{dE}{df}}, \quad (3.3)$$

where D is the distance to the source and

$$\frac{dE}{df} = \frac{8\pi^2}{15} \frac{c^3}{G} f^2 \left| \tilde{A}_2(f) \right|^2 \quad (3.4)$$

is the energy power spectra of the gravitational radiation. $\tilde{A}_2(f)$ is the Fourier transform of A_2 ,

$$\tilde{A}_2(f) = \int A_2(t) e^{2\pi i f t} dt \quad (3.5)$$

with A_2 being the $+$ -mode of gravitational waves with $l = 2$ and $m = 0$,

$$h_+^{\text{quad}} = \frac{\ddot{I}_{zz}(t_{\text{ret}}) - \ddot{I}_{xx}(t_{\text{ret}})}{D} \sin^2 \theta \equiv \frac{A_2(t)}{D} \sin^2 \theta, \quad (3.6)$$

where I_{ij} denotes a quadrupole moment,⁷⁴⁾ \ddot{I}_{ij} its second time derivative, and t_{ret} a retarded time. Because the strain of gravitational waves has a broad-band spectrum, they appear to be emitted primarily by a long-term stochastic motion of the infalling material and of the matter in the HMNS, as in the collapse of ordinary cores.²⁹⁾

Note that h_{char} includes only gravitational waves from the matter contribution and not from the anisotropic neutrino emissions. We also show the noise amplitudes of Advanced LIGO for a version in which no signal recycling mirror is used (NO SRM) and of a version of a specially designed narrow-band Advanced LIGO (High Freq) together.⁷⁵⁾

The effective amplitude of gravitational waves observed in the most optimistic direction is $h_{\text{char}} \sim 10^{-20}$ for an hypothetical event at a distance of 10 kpc, which is larger than that for the ordinary supernova.²⁹⁾ The frequency at the peak amplitude is 1–2 kHz. The reason for this larger gravitational-wave amplitude is that the HMNS in the present model has a larger mass and the gravitational-wave signal is accumulated during the long-term convective activity, for which the duration $\gtrsim 1$ s is longer than that for the ordinary supernova. Figure 13 shows that with NO-SRM Advanced LIGO the signal of gravitational waves will be detected with a signal-to-noise ratio $S/N \sim 10$ for $D = 10$ kpc. For High-Freq Advanced LIGO, the detection may be done with $S/N \sim 100$ for $D = 10$ kpc. Even for $D = 50$ kpc (the distance to the Large Magellanic Cloud), the detection will be possible with $S/N \gtrsim 20$.

For an event of $D \lesssim 50$ kpc, a large number of neutrinos will be also detected by water-Cherenkov neutrino detectors such as Super-Kamiokande and future Hyper-Kamiokande (see also a discussion in § 4.2).

3.4. Possible association to Gamma-ray bursts

Before closing this section, we give an order estimate of the energy deposition rates ($\dot{E}_{\nu\bar{\nu}}$) by the neutrino pair-annihilation which is one of the possible processes to drive relativistic jets required to produce LGRBs. Note that the energy from the neutrino pair annihilation should be deposited in a baryon-poor region in order to generate highly relativistic outflows. The funnel region near the rotational axis above the torus formed in UN100-rigid is a promising place for this purpose.

According to the estimate in Ref. 76), the deposition rate in the BH-torus system would be proportional to $\dot{M}^{9/4} M_{\text{BH}}^{-3/2}$. In this estimation, the neutrino luminosity is assumed to be originated from a viscous heating. In our present simulations, the neutrino luminosity is determined by the infalling rate of the material which experiences the shock heating at the surface of the torus to increase the thermal energy of the torus. However, the dependence of the pair-annihilation rate on the mass infall rate \dot{M} is essentially the same for thick torus phase. Figure 14 shows the irreducible mass of the BH (the upper panel) and the mass accretion rate (the lower panel). Due to this strong dependence on \dot{M} , the energy deposition by the neutrino pair-annihilation would be important only for a phase in which $L_{\nu,\text{tot}} \gtrsim 10^{51}$ ergs/s (see Figs. 11(b) and 12(b)). Figure 12(b) shows that for UN100-rigid, the duration of the neutrino emission (in the BH phase) with $L_{\nu,\text{tot}} \gtrsim 10^{51}$ ergs/s is longer than 1 s, and thus, a long-term energy deposition for a LGRB may be explained. Taking into account the dependence of the neutrino pair annihilation rate on the geometry of the torus,^{77), 76), 78), 79)} $\dot{E}_{\nu\bar{\nu}}$ would be given by,⁷⁶⁾

$$\dot{E}_{\nu\bar{\nu}} \sim 10^{48} \text{ ergs/s} \left(\frac{100 \text{ km}}{R_{\text{fun}}} \right) \left(\frac{0.1}{\theta_{\text{fun}}} \right)^2 \left(\frac{E_{\nu} + E_{\bar{\nu}}}{10 \text{ MeV}} \right)$$

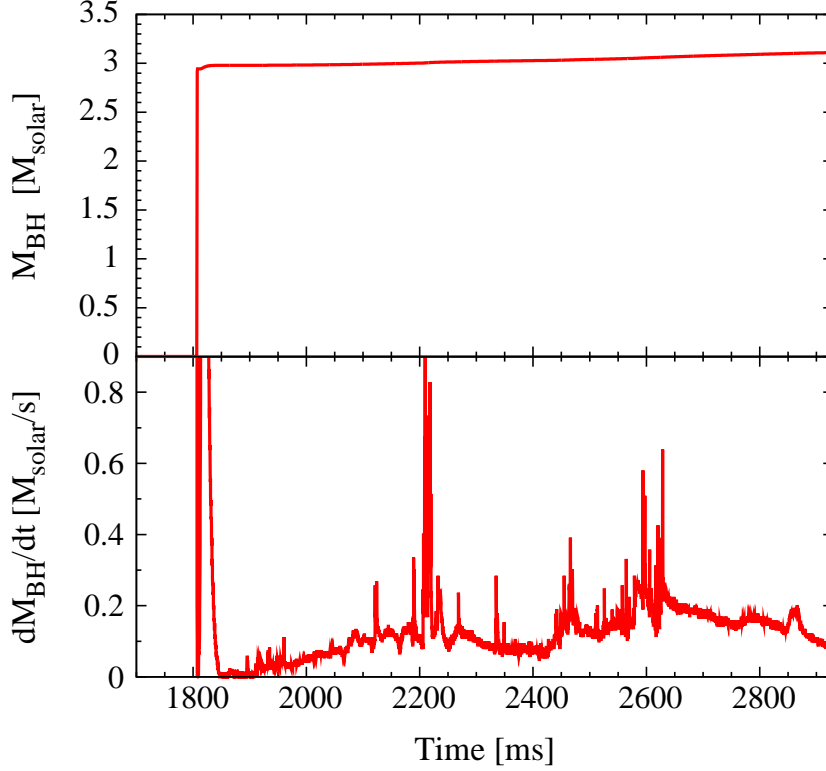


Fig. 14. Time evolution of the irreducible mass of the BH (the upper panel) and the mass accretion rate (the lower panel) for UN100-rigid.

$$\times \left(\frac{L_\nu}{10^{51} \text{ ergs/s}} \right) \left(\frac{L_{\bar{\nu}}}{10^{51} \text{ ergs/s}} \right) \sin^2 \Theta, \quad (3.7)$$

where R_{fun} and θ_{fun} are the characteristic radius and the opening angle of the funnel region. Θ denotes the collision angle of the neutrino pair. Thus a low-luminosity LGRB could be explained.

In the HMNS phase, by contrast, the neutrino luminosity is huge as $L_\nu \gtrsim 10^{53}$ ergs/s (see Figs. 11(a) and 12(a)), and hence, the deposition rate would be very large as

$$\begin{aligned} \dot{E}_{\nu\bar{\nu}} \sim & 3 \times 10^{52} \text{ ergs/s} \left(\frac{100 \text{ km}}{R_{\text{fun}}} \right) \left(\frac{0.1}{\theta_{\text{fun}}} \right)^2 \left(\frac{E_\nu + E_{\bar{\nu}}}{30 \text{ MeV}} \right) \\ & \times \left(\frac{L_\nu}{10^{53} \text{ ergs/s}} \right) \left(\frac{L_{\bar{\nu}}}{10^{53} \text{ ergs/s}} \right) \sin^2 \Theta. \end{aligned} \quad (3.8)$$

If the outflows launched due to the mass accumulation mechanism can penetrate the stellar envelope, a system composed of a long-lived HMNS and a geometrically thick torus may be a promising candidate of the central engine of LGRBs a relatively short duration.

§4. Binary neutron star merger

Coalescence of binary neutron stars (BNS) is one of the most promising sources for next-generation kilo-meter-size gravitational-wave detectors,^{1),2),3)} and also a possible candidate for the progenitor of SGRBs.^{80),81)} Motivated by these facts, numerical simulations have been extensively performed for the merger of BNS in the framework of full general relativity in the past decade since the first success⁸²⁾ in 2000 (see also, e.g., Refs. 33) for reviews).

BNS evolve due to the gravitational radiation reaction and eventually merge. Before the merger sets in, each neutron star is cold (i.e., thermal energy of constituent nucleons is much smaller than their Fermi energy), because the thermal energy inside the neutron stars is significantly reduced by neutrino and photon emissions⁸³⁾ in the long-term inspiral phase (typically $\gtrsim 10^8$ years⁹⁰⁾) until the merger. By contrast, after the merger sets in, shocks are generated by hydrodynamic interactions. In particular, when a HMNS is formed in the merger, spiral arms are developed in its envelope and continuous heating occurs due to the collision between the HMNS and spiral arms (e.g., Refs. 84), 85), 86)). Newtonian simulations indeed suggest that by this process the maximum temperature increases to $\sim 30\text{--}50$ MeV, and hence, copious neutrinos are emitted.^{21),22),87),88)} Thus, to accurately explore the merger process, the evolution of the hot HMNS, and possible subsequent formation of a BH with a physical modeling, numerical-relativity simulations have to be performed incorporating microphysical processes such as neutrino emission and equation of state (EOS) based on a theory for the high-density and high-temperature nuclear matter. However, such simulations have not been done in full general relativity until quite recently (but see Ref. 19) for a work in an approximate general relativistic gravity with finite-temperature EOS). Incorporation of microphysical processes is in particular important for exploring the merger hypothesis of SGRB because it may be driven through pair annihilation of neutrino-antineutrinos pairs.^{80),81)}

In this section, we review our first results of numerical-relativity simulations for the BNS merger presented in Refs. 27), 28), which are performed incorporating both a finite-temperature EOS^{9),25)} and neutrino cooling.¹¹⁾ In the following, we summarize the possible outcome formed after the merger, criteria for the formation of HMNS and BH, thermal properties of the HMNS and torus surrounding the formed BH, and neutrino luminosity and gravitational waveforms from the HMNS and in the BH formation.

4.1. Initial condition and grid setting

In Refs. 27), 28), we focused only on the merger of equal-mass BNS, because the mass difference for the observed BNS is not very large.^{89),90)} To date, we have performed simulations for 5 models: For Shen-EOS, we employed three masses for each neutron star: $M_{\text{NS}} = 1.35, 1.5, \text{ and } 1.6M_{\odot}$ (M_{NS} is the gravitational mass of a neutron star in isolation). We refer to each model as models S135, S15, and S16, respectively. For Hyp-EOS, we employed $M_{\text{NS}} = 1.35$ and $1.5M_{\odot}$, and refer to two models as H135 and H15, respectively. The simulations were performed with the initial condition of about 3–4 orbits before the onset of the merger, until the system

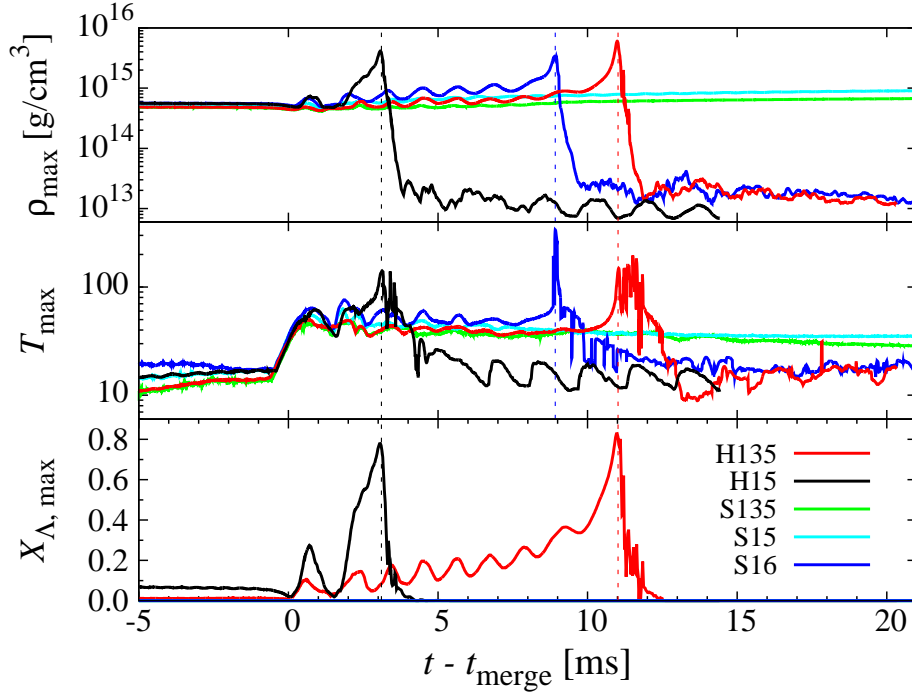


Fig. 15. Maximum rest-mass density, maximum matter temperature, and maximum hyperon fraction in mass as functions of time for all the models. t_{merge} denotes the onset time of the merger. The dashed vertical line shows the time at which a BH is formed for models S16, H135, and H15.

relaxes to a quasi-stationary state. Quasi-equilibrium states of BNS were prepared as the initial conditions, as in Refs. 84), 85), using the LORENE library.⁹¹⁾

There are two possible fates⁸⁴⁾ of BNS: If its total mass M is larger than a critical mass M_c , a BH will be formed soon after the onset of the merger, while a differentially rotating HMNS will be formed for $M < M_c$. The value of M_c depends strongly on the EOS. Because Shen-EOS is quite stiff, M_c is much larger than the typical total mass of BNS, $\sim 2.7M_\odot$,^{89), 90)} as shown in Ref. 27) and below. Thus, with this EOS, the HMNS will be the frequent outcomes, as in the cases of stiff EOS with which $M_{\text{max}} > 2M_\odot$.⁹²⁾ By contrast, Hyp-EOS is not stiff in particular for a high-density range. Thus, a BH is often formed with this EOS, although a HMNS could be a transient outcome soon after the onset of the merger.²⁸⁾

Numerical simulations were performed preparing a non-uniform grid as in Ref. 85). The inner domain was composed of a finer uniform grid and the outer domain of a coarser nonuniform grid. The grid resolution in the inner zone is chosen so that the major diameter of each neutron star in the inspiral orbit was covered by 60 and 80 grid points for low- and high-resolution runs, respectively: We always performed simulations for both grid resolutions to confirm that the convergence, sufficient to draw a scientific conclusion on the final outcome, gravitational waveforms, and neutrino luminosities, is approximately achieved. Outer boundaries are located in a local wave

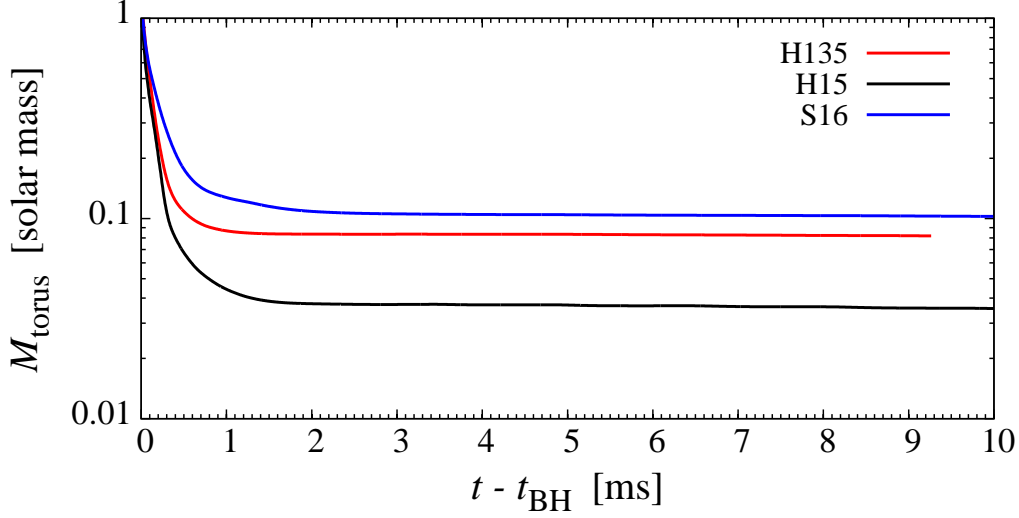


Fig. 16. The rest mass of a torus surrounding the formed BH as a function of time for models H135, H15, and S16. t_{BH} denotes the time at the formation of the BH.

zone (at $\approx 560\text{--}600$ km along each coordinate axis which is longer than gravitational wavelength in the inspiral phase). During the simulations, we checked the conservation of the baryon rest-mass, total gravitational mass (Arnowitt-Deser-Misner mass plus radiated energy of gravitational waves), and total angular momentum (including that radiated by gravitational waves), and found that the errors are within 0.5%, 1%, and 3%, respectively, for the high-resolution runs within the physical duration ≈ 30 ms.

4.2. Merger and subsequent evolution

Figure 15 plots the maximum rest-mass density, ρ_{max} , maximum matter temperature, T_{max} , and maximum hyperon fraction in mass $X_{\Lambda, \text{max}}$ as functions of $t - t_{\text{merge}}$ where t_{merge} is the onset time of the merger. For $t < t_{\text{merge}}$, ρ_{max} is approximately constant besides a small decline due to tidal elongation, while for $t \gtrsim t_{\text{merge}}$, it gradually increases because a HMNS is formed at least temporarily irrespective of models, and subsequently contracts due to the dissipation of the angular momentum by the gravitational-wave emission. Thus, ρ_{max} increases in the gravitational radiation time scale. The subsequent evolution process depends on the mass and EOS. For models S135 and S15, the degree of non-axial symmetry of the HMNS becomes low enough at $t - t_{\text{merge}} \sim 20$ ms that the emissivity of gravitational waves is significantly reduced. Because no dissipation process except for the neutrino cooling is present, the HMNS will be alive at least for the cooling time scale before collapsing to a BH (see below). For models S16, H135, and H15, the HMNS collapse to a BH at $t - t_{\text{merge}} \lesssim 10$ ms after the gradual contraction due to the gravitational-wave emission and a massive disk of $\approx 0.03\text{--}0.1M_{\odot}$ is formed around the BH. It should be noted that for Hyp-EOS, a BH is formed at $t - t_{\text{merge}} \sim 10$ ms even with the total mass $2.7M_{\odot}$. This is due to the softening effect by the appearance of Λ hyperons:

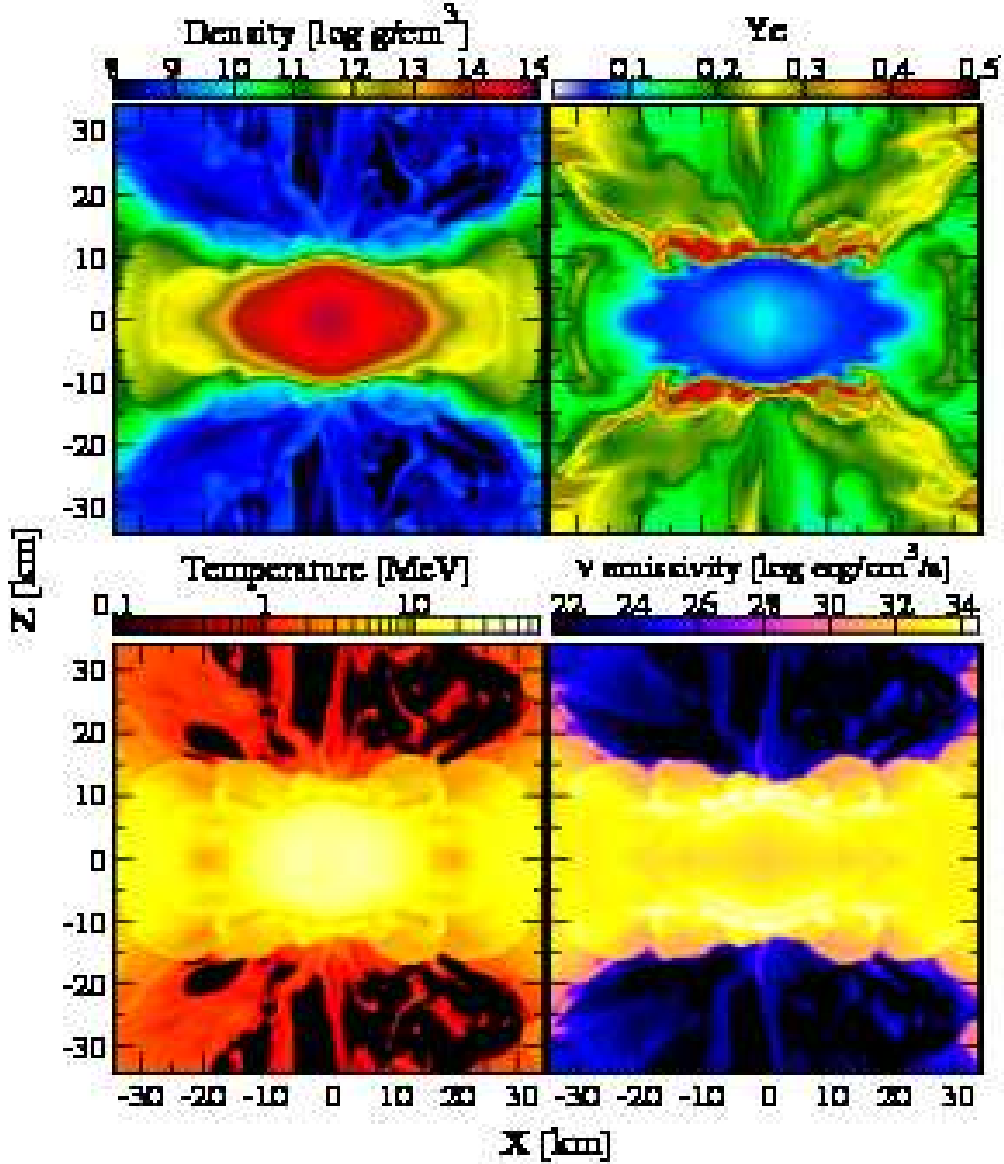


Fig. 17. Contour maps in the x - z plane of the rest-mass density (top left), the electron fraction (top right), the temperature (bottom left), and the total neutrino emissivity (bottom right) at $t \approx 16.7$ ms after the onset of the merger for model S135.

See the bottom panel of Fig. 15, which shows that $X_{A,\max}$ increases steeply just before the HMNS collapses to a BH.

The evolution of T_{\max} plotted in Fig. 15 shows that the HMNS formed just after the merger are hot with $T_{\max} \sim 50$ – 70 MeV (much higher than that in the ordinary supernova and as high as that in the HMNS formed after the collapse of the massive stellar core; cf. § 3). Such a high temperature is achieved due to the liberation of the kinetic energy of the orbital motion at the collision of two neutron stars. For

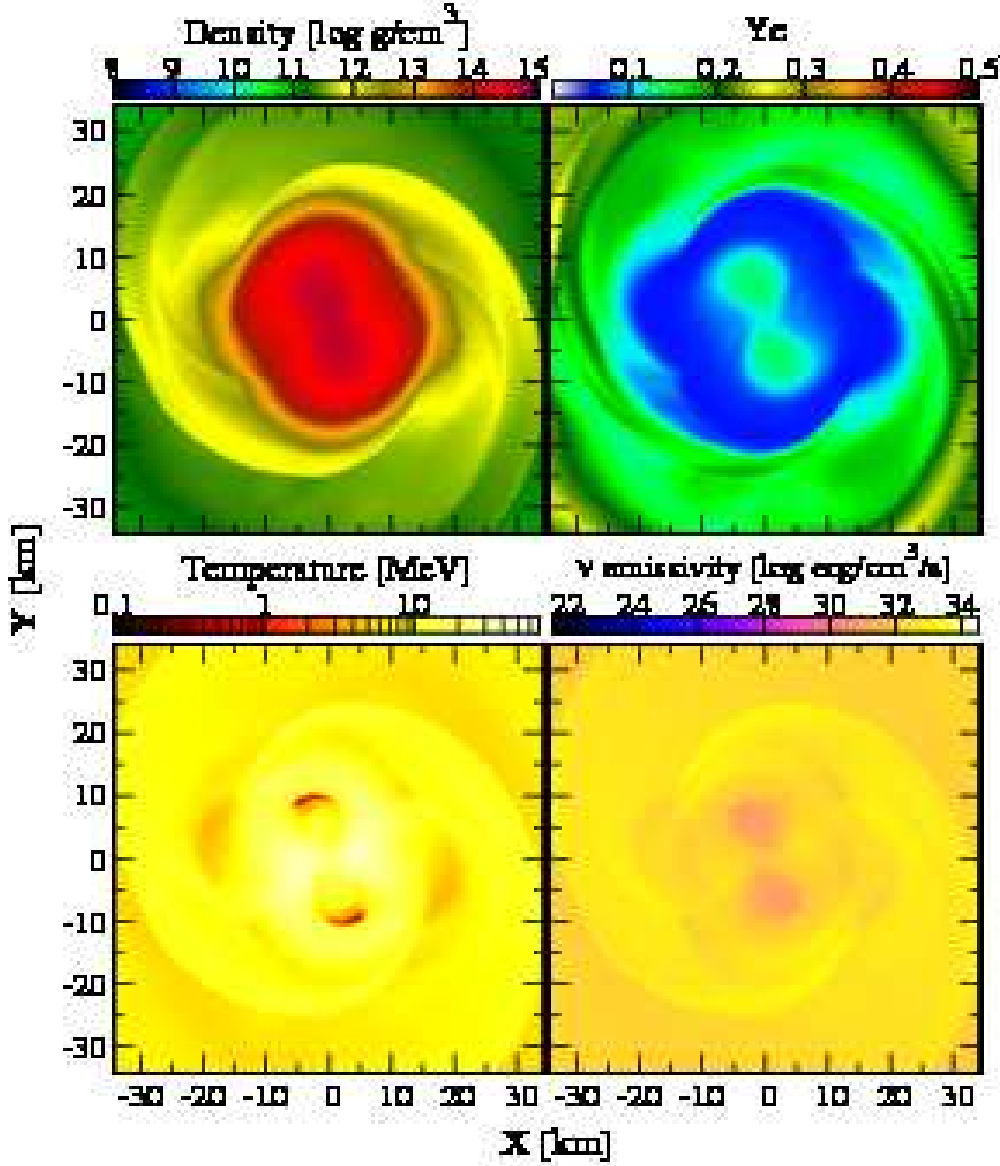


Fig. 18. The same figure as Fig. 17 but in the x - y plane.

the case that a long-lived HMNS is formed, subsequently, T_{\max} decreases due to the neutrino cooling, with the maximum luminosity $3\text{--}10 \times 10^{53}$ ergs/s (see Fig. 23), but relaxes to a high value with 25–50 MeV when the HMNS relaxes to a quasi-steady state. Around the HMNS, spiral arms are formed and shock heating continuously occurs when the spiral arms hit the HMNS (see Figs. 17–22 for snapshots). Due to this process and because of the long neutrino-cooling time scale, the temperature (and thermal energy) does not significantly decrease in ~ 100 ms: We estimated the cooling time scale as $E_{\text{th}}/L_\nu \sim 2\text{--}3$ s where E_{th} is the total thermal energy of the

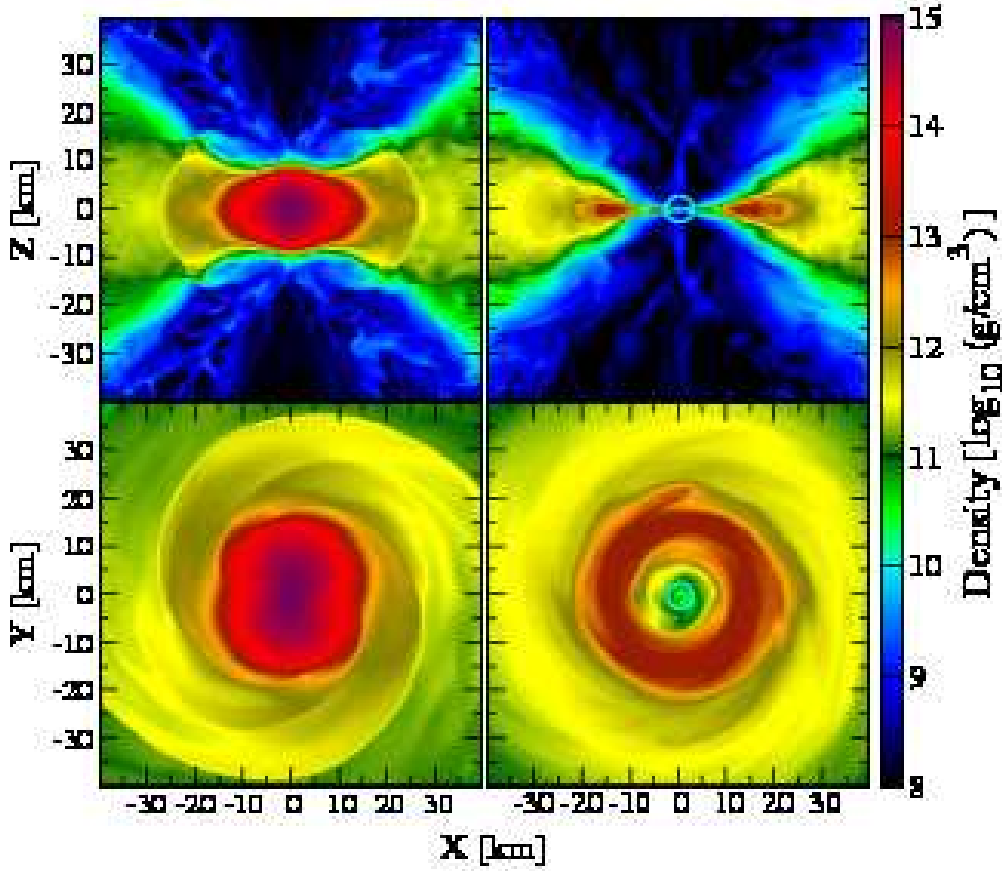


Fig. 19. Contour maps of the rest-mass density for a HMNS phase at $t \approx 17.5$ ms after the merger (left panels) and that for a BH phase at $t \approx 26.8$ ms after the onset of the merger for model H135. The upper and lower panels show the configuration in the x - y and x - z planes, respectively. The blue circle of the right panels shows the location of the apparent horizon.

HMNS.

For the case that a BH is eventually formed, the maximum temperature raises significantly to $\gtrsim 100$ MeV just before the BH formation. This is simply due to the adiabatic compression effect. For models S16, H135, and H15, a torus surrounding the BH is subsequently formed. The typical maximum density and temperature of the torus are $\sim 10^{13}$ g/cm³ and 20 MeV, respectively, with the mass ≈ 0.03 – $0.1M_{\odot}$ (see Fig. 16). This mass has a correlation with the lifetime of the HMNS; for the longer lifetime (e.g., for model S16), the torus mass is larger (compare the mass of the torus in Fig. 16). The reason is that during the evolution of the HMNS which is deformed in a non-axisymmetric manner, the angular momentum is transported from the inner to the outer region via the hydrodynamic torque associated with its non-axisymmetric structure. Thus, the longer lifetime helps increasing the mass element of a sufficiently large specific angular momentum which can escape falling into the formed BH. This fact implies that stiff EOS are favored for the formation

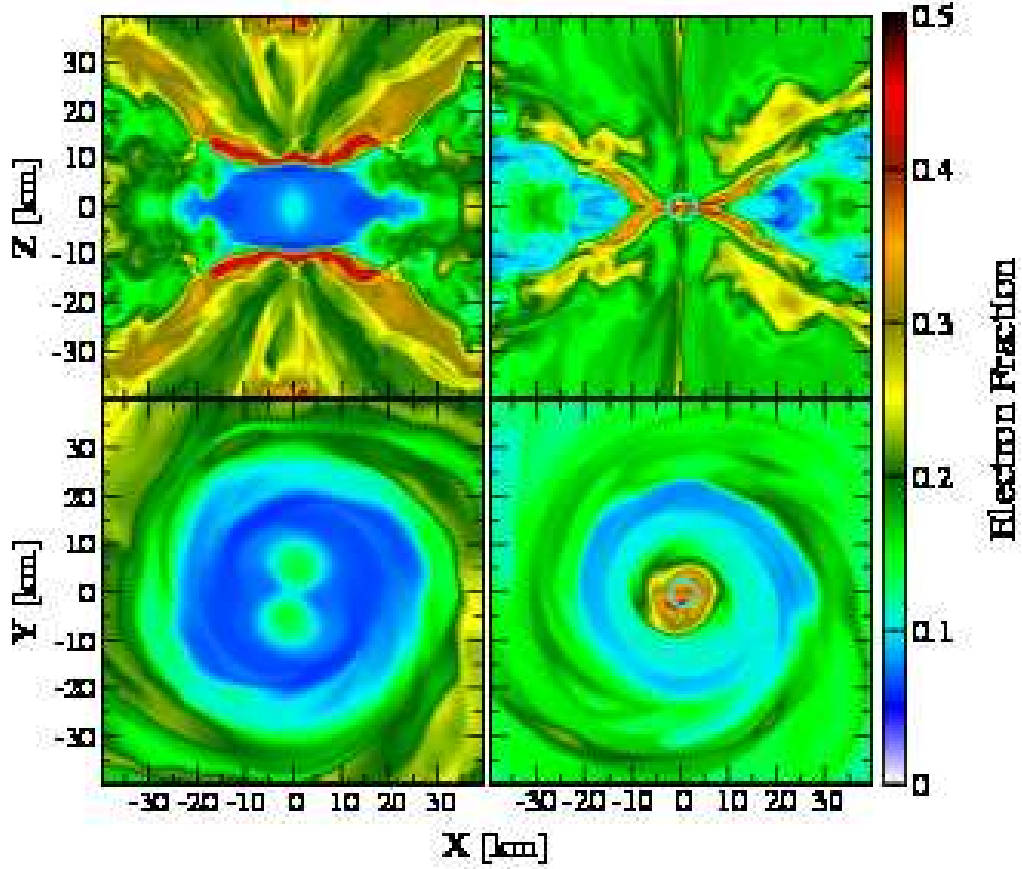


Fig. 20. The same figure as Fig. 19 but for the electron fraction.

of a massive torus.

Figures 17 and 18 plot the contour maps of the rest-mass density, electron fraction, matter temperature, and total neutrino luminosity of a HMNS for model S135 at $t - t_{\text{merge}} \approx 16.7$ ms in the x - z and x - y planes, respectively, at which it already relaxed to a semi-final quasi-steady state. This shows that the HMNS is weakly spheroidal and the temperature is high ($T \sim 30$ MeV) in its outer region. The neutrino luminosity is also high in its outer region, in particular, near the polar surface. With the fact that the rest-mass density is relatively small near the rotation axis above the polar surface, this is a favorable feature for the merger hypothesis of SGRB; pair annihilation of neutrinos and anti-neutrinos could supply a large amount of thermal energy which may drive a fire ball along the rotation axis. As in § 3.4, the neutrino pair annihilation rate is estimated as

$$\begin{aligned} \dot{E}_{\nu\bar{\nu}} \sim & 10^{51} \text{ ergs/s} \left(\frac{50 \text{ km}}{R_{\text{fun}}} \right) \left(\frac{0.3}{\theta_{\text{fun}}} \right)^2 \left(\frac{E_{\nu} + E_{\bar{\nu}}}{20 \text{ MeV}} \right) \\ & \times \left(\frac{L_{\nu}}{10^{53} \text{ ergs/s}} \right) \left(\frac{L_{\bar{\nu}}}{10^{53} \text{ ergs/s}} \right) \sin^2 \Theta, \end{aligned} \quad (4.1)$$

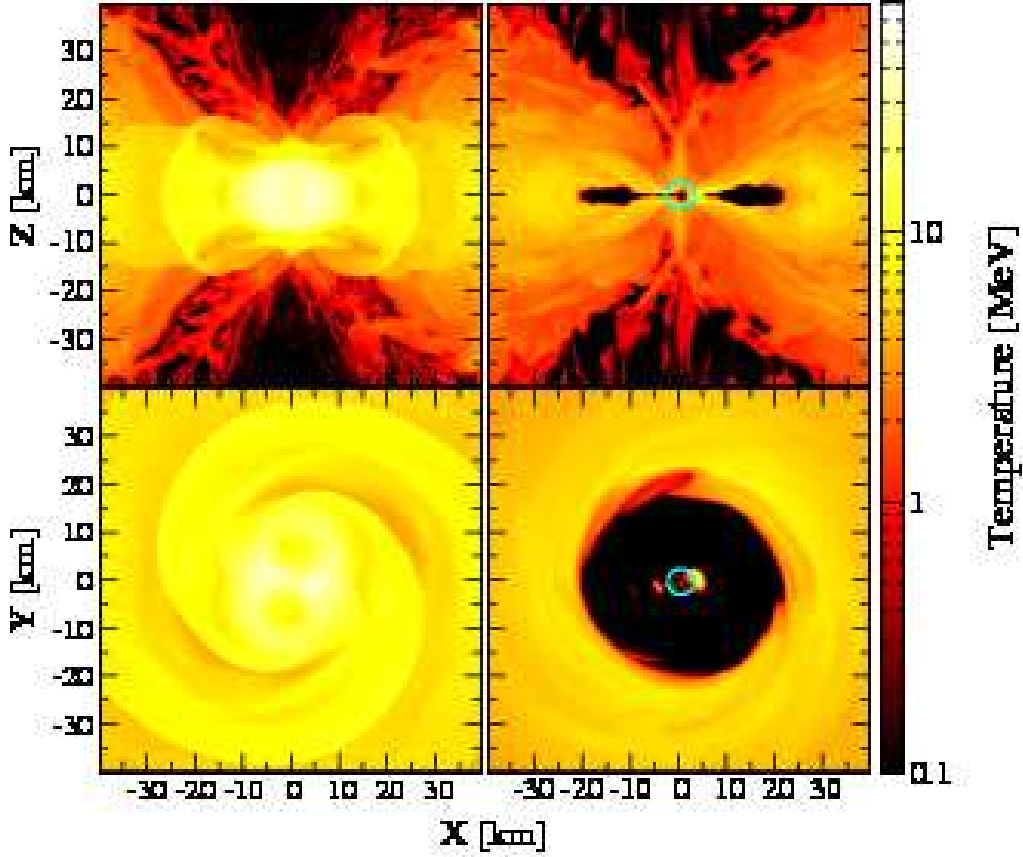


Fig. 21. The same figure as Fig. 19 but for the temperature.

which would be sufficient for driving SGRBs. The pair annihilation efficiency has been approximately estimated in the previous works^{(21), (22), (87), (88)} and our result is consistent with these works.

Possible reasons that HMNS are formed are; (i) it is rapidly rotating with the period ~ 1 ms, and hence, the centrifugal force increases the possible mass that can be sustained; (ii) because it is hot, the thermal energy enhances the pressure. We find that the rotational velocity with the period ~ 1 ms does not play a substantial role. Exploring in detail Shen-EOS for the high density tells us that the effect of the thermal energy is significant and can increase M_{max} by $\sim 20\text{--}30\%$ for a high-temperature state with $T \gtrsim 20$ MeV. This indicates that the HMNS will alive before collapsing to a BH for a long cooling time $\gtrsim 1$ s. At the time when the HMNS collapse to a BH, it will be close to a spherical configuration with low temperature due to long-term gravitational-wave and neutrino emissions. Thus, observable signals from the late-time collapse will not be remarkable.

Figure 23 plots neutrino luminosities as functions of time for three flavors (ν_e , $\bar{\nu}_e$, and sum of ν_x). It is found that electron anti-neutrinos are dominantly emitted for any model. The reason for this is as follows: The HMNS has a high temperature, and

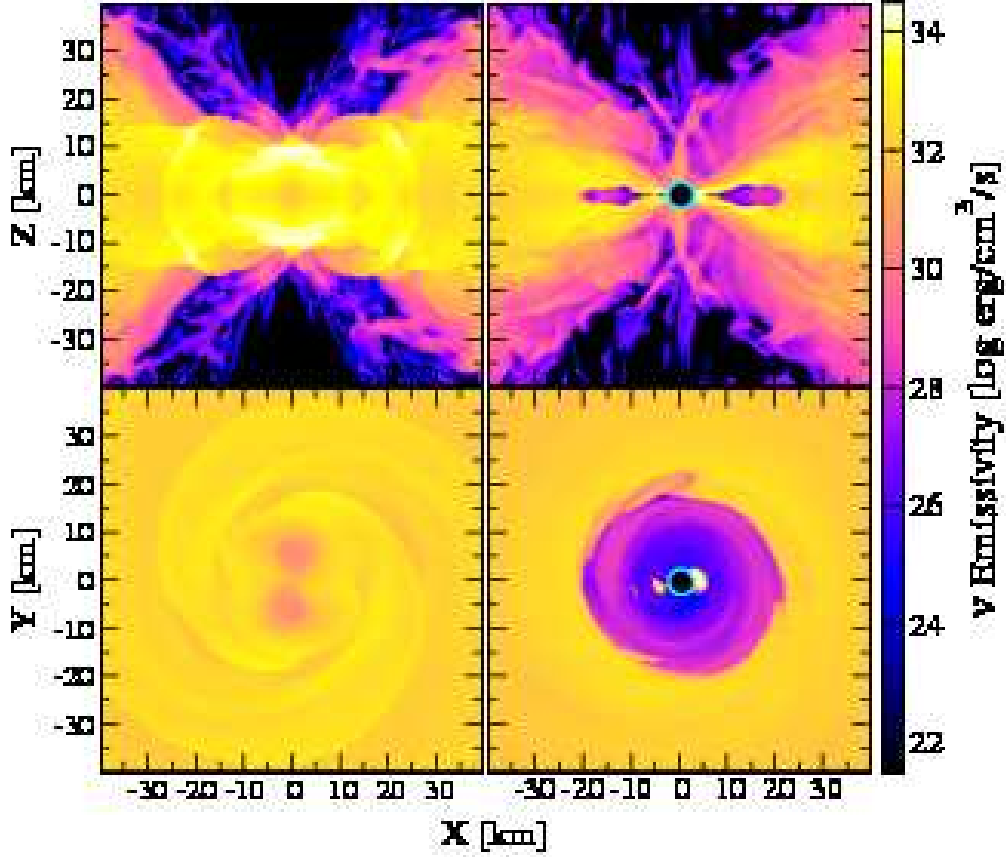


Fig. 22. The same figure as Fig. 19 but for the total neutrino emissivity.

hence, electron-positron pairs are efficiently produced from thermal photons, in particular in its envelope. Neutrons efficiently capture positrons to emit anti-neutrinos whereas electrons are not captured by protons as frequently as positrons because the proton fraction is much smaller. This hierarchy in the neutrino luminosities was reported also in Refs. 21), 22).

Soon after the BH formation for models S16, H135, and H15, μ/τ neutrino luminosity steeply decreases because high-temperature regions are swallowed into the BH, while luminosities of electron neutrinos and anti-neutrinos decrease only gradually because these neutrinos are emitted via charged-current processes from the massive accretion disk. We here note that magnetic fields, which are not taken into account in the present simulations, could be amplified significantly in the accretion disk⁸⁶⁾ and may play a role in the late evolution of the BH-disk system.

The *anti-neutrino* luminosity for the long-lived HMNS is $L_{\bar{\nu}} \sim 1.5\text{--}3 \times 10^{53}$ ergs/s with a small time variability. It is by a factor of $\sim 1\text{--}5$ larger than that from proto-neutron stars formed after supernovae,⁶⁾ while it is comparable to the luminosities for UN100-rigid model. The averaged neutrino energy is $\epsilon_{\bar{\nu}} \sim 20\text{--}30$ MeV. The sensitivity of water-Cherenkov neutrino detectors such as Super-Kamiokande and

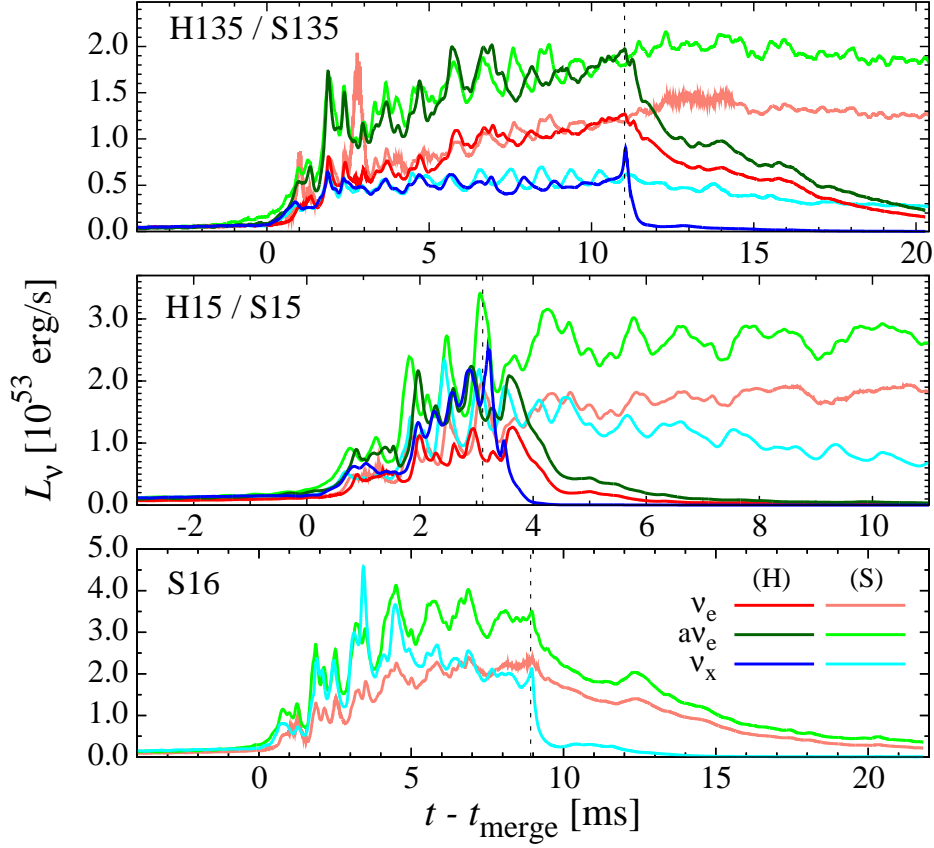


Fig. 23. Neutrino luminosities for three flavors for all the models. The upper, middle, and lower panels show the results for $M_{\text{NS}} = 1.35, 1.5$, and $1.6M_{\odot}$, respectively. The meaning of the dashed line is the same as in Fig. 15.

future Hyper-Kamiokande have a good sensitivity for such high-energy neutrinos in particular for electron anti-neutrinos.⁹³⁾ The detection number for electron anti-neutrinos is approximately estimated by $\sigma \Delta T L_{\bar{\nu}} / (4\pi D^2 \epsilon_{\bar{\nu}})$ where σ is the total cross section of the detector against target neutrinos, ΔT is the lifetime of the HMNS, and D is the distance to the HMNS. For a one-Mton detector such as Hyper-Kamiokande, the expected detection number is $\gtrsim 10$ for $D \lesssim 5$ Mpc with $\Delta T \sim 2\text{--}3$ s, based on an analysis of Ref. 93). Thus, if the BNS merger fortunately happens within $D \sim 5$ Mpc, neutrinos from the HMNS may be detected and its formation may be confirmed. Note that gravitational waves from the HMNS will be simultaneously detected for such a close event (see below), reinforcing the confirmation of the HMNS formation.

4.3. Gravitational waves

Figure 24(a) plots the plus mode (h_+) of gravitational waves as a function of $t_{\text{ret}} - t_{\text{merge}}$ where t_{ret} is the retarded time, $t_{\text{ret}} = t - D - 2M \log(D/M)$ ($M = 2M_{\text{NS}}$). Gravitational waves are extracted from the metric through the outgoing

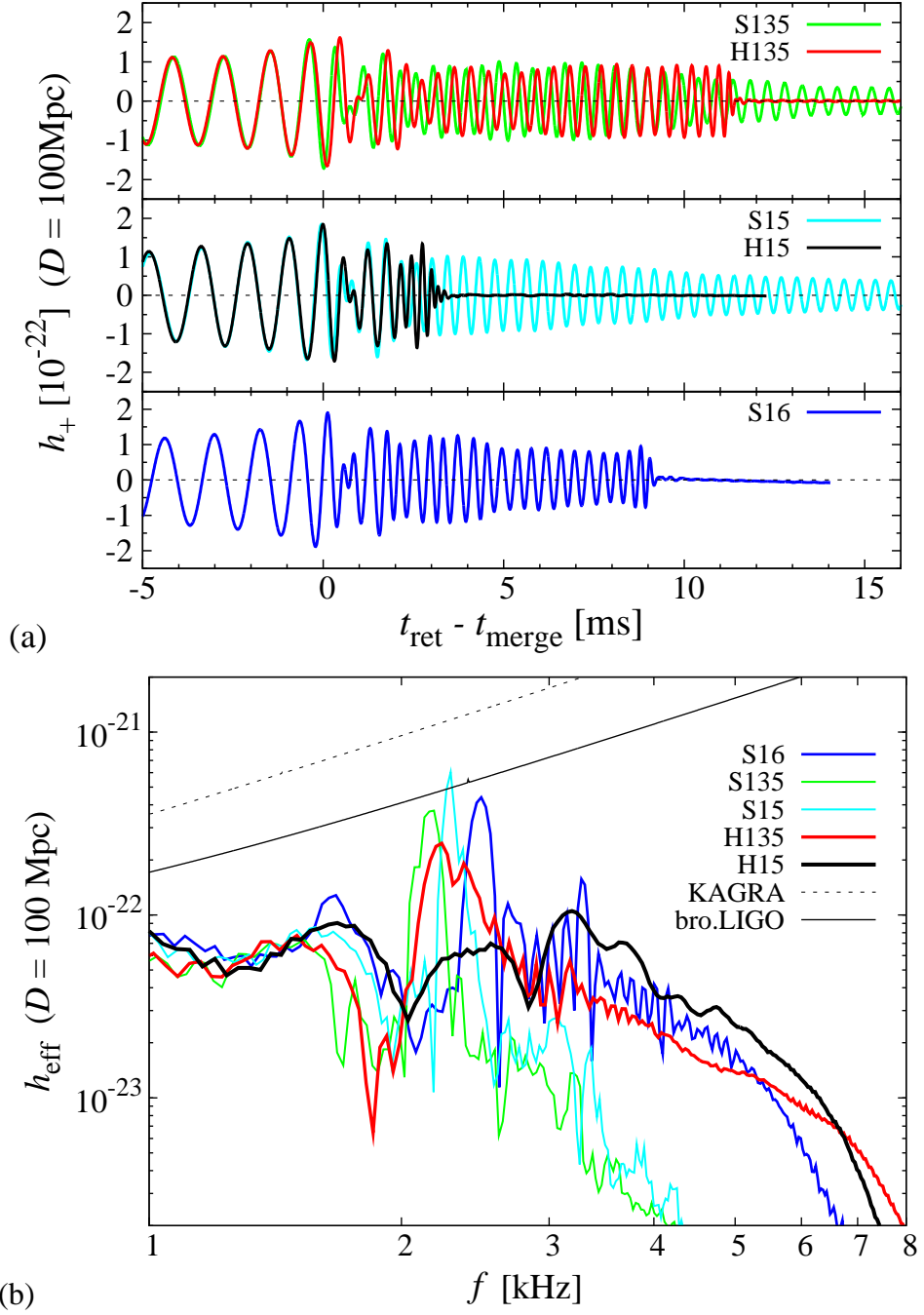


Fig. 24. (a) Gravitational waves observed along the axis perpendicular to the orbital plane for the hypothetical distance to the source $D = 100$ Mpc for all the models. (b) The effective amplitude of gravitational waves as a function of frequency for $D = 100$ Mpc. The noise amplitudes of a broadband configuration of Advanced LIGO (bro. LIGO) and KAGRA are shown together.

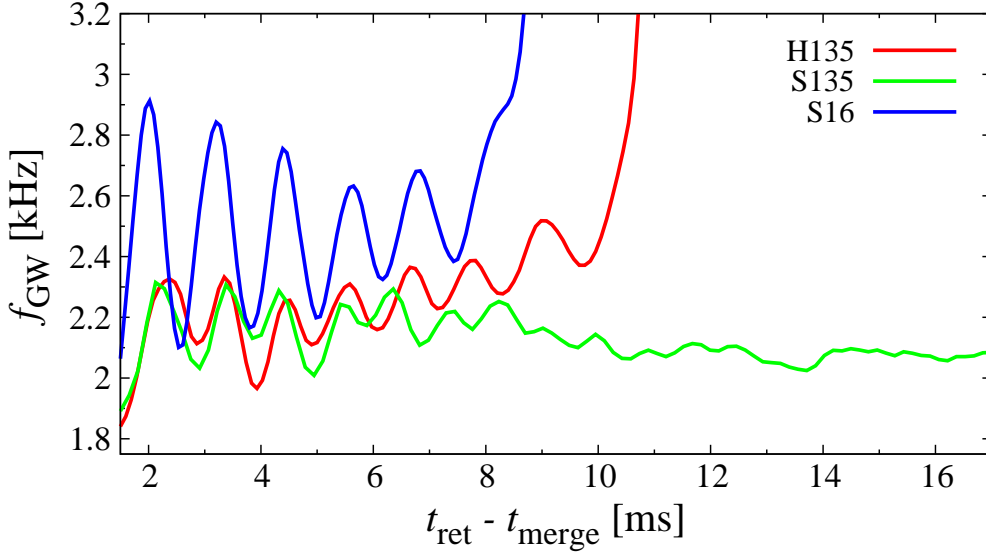


Fig. 25. $f_{\text{GW}}(t)$ in the HMNS evolution phase, smoothed by a weighted spline, for models H135, S135, and S16.

component of the complex Weyl scalar, Ψ_4 , in the local wave zone. The waveforms are composed of the so-called chirp waveform, which is emitted when the BNS is in an inspiral motion (for $t_{\text{ret}} \lesssim t_{\text{merge}}$), and the merger waveform (for $t_{\text{ret}} \gtrsim t_{\text{merge}}$). Gravitational waves from the inspiral phase (for $t_{\text{ret}} \lesssim t_{\text{merge}}$) agree well with each other for the models with Hyp-EOS and Shen-EOS for the same mass. On the other hand, quasi-periodic gravitational waves from the HMNS (for $t_{\text{ret}} \gtrsim t_{\text{merge}}$) show several differences. First, the amplitude of quasi-periodic gravitational waves damps steeply at the BH formation for H135 and H15. This is because the HMNS collapse to a BH before relaxing to a stationary spheroid. Second, the characteristic gravitational-wave frequency, f_{GW} , *increases* with time for Hyp-EOS models, while it is approximately constant for Shen-EOS models with $f_{\text{peak}} \approx 2.0\text{--}2.5$ kHz which depends weakly on M . These facts are clearly observed in the effective amplitude (see Fig. 24(b)) defined by $h_{\text{eff}}(f) \equiv 0.4f|h(f)|$ where $h(f)$ is the Fourier transform of $h_+ - ih_\times$ with h_\times being the cross mode and the factor 0.4 comes from taking the average in terms of the random direction to the source and rotational axis of the HMNS. Reflecting a shorter lifetime of the HMNS in Hyp-EOS models, the peak amplitude of $h_{\text{eff}}(f)$ is smaller, in particular for H15 where the HMNS survives only for a short period ~ 3 ms. Reflecting the shift of the characteristic frequency, the prominent peak in h_{eff} for Hyp-EOS models (H135 and H15) is broadened. The reason for this is described as follows in more detail.

In the case that hyperons are absent, the HMNS slightly contract during their evolution simply due to the angular momentum loss (weakening centrifugal force). By contrast, in the case that hyperons are present, X_A increases with the contraction of the HMNS, resulting in the relative reduction of the pressure. As a result, the HMNS contracts by a larger fraction. Recent studies showed that f_{GW} is associated

with the frequency of an f -mode which is approximately proportional to $\sqrt{M_{\text{H}}/R_{\text{H}}^3}$ where M_{H} and R_{H} are the mass and radius of the HMNS.⁹⁴⁾ This indicates that f_{GW} should increase with time. To see that this is indeed the case, we show $f_{\text{GW}}(\equiv d\phi_{\text{NP}}/dt)$ calculated from $\Psi_4 \equiv |Psi_4|e^{i\phi_{\text{NP}}}$ in the HMNS phase for H135, S135, and S16 in Fig. 25. It is clearly seen that the mean value of f_{GW} is approximately constant for Shen-EOS models; $f_{\text{GW}} \approx 2.1$ and 2.5 kHz for S135 and S16, respectively. By contrast, f_{GW} for H135 increases with time (from $f_{\text{GW}} \approx 2.0$ kHz at $t_{\text{ret}} - t_{\text{merge}} = 2$ ms to ≈ 2.5 kHz at $t_{\text{ret}} - t_{\text{merge}} = 10$ ms) as the HMNS becomes compact.

Figure 24(b) shows that if a HMNS with the lifetime $\gtrsim 10$ ms is formed, the effective amplitude $h_{\text{eff}} \sim 4\text{--}6 \times 10^{-22}$ at $D = 100$ Mpc for Shen-EOS models and 2×10^{-22} at $D = 100$ Mpc for H135 with $f_{\text{peak}} \approx 2.0\text{--}2.5$ kHz which depends weakly on M and EOS. For the detection, Hyp-EOS is obviously unfavored. By contrast, for Shen-EOS, the maximum amplitude for a hypothetical distance of 100 Mpc is as high as the sensitivity curve of a specially-designed version of advanced gravitational-wave detectors such as broadband LIGO,⁷⁵⁾ which has a good sensitivity for a high-frequency band. This suggests that gravitational waves from the HMNS oscillations may be detected with $S/N = 5$ if $D \lesssim 20$ Mpc. If the source is located in an optimistic direction, the detection with $S/N = 5$ may be possible for $D = 50$ Mpc.

§5. Summary

We have described our latest results of numerical-relativity simulations of rotating stellar core collapses to a BH and BNS mergers, performed incorporating a finite-temperature EOS and neutrino cooling effects. The following is the summary of our latest findings and prospects for the near future.

5.1. Stellar core collapse

We presented our latest results of axisymmetric simulations of very massive stellar core collapsing to a system composed of a rotating BH and surrounding disk/torus in full general relativity. The simulation were performed taking into account of the microphysical processes and the neutrino cooling. Because progenitor models of LGRBs suggested in the literatures⁶⁵⁾ propose a possibility that they may have an entropy higher than that of ordinary supernova cores, we employed a model of a pre-supernova core with a high entropy of $s/k_B = 4$ calculated by Umeda and Nomoto⁶⁶⁾ together with hypothetical two rotational profiles (UN100-rigid and UN100-diff).

As in the collapse of ordinary supernova cores, the gravitational collapse sets in due to the photo-dissociation of heavy nuclei and the electron capture. The collapsing core eventually experiences a core bounce, forming a shock wave. Then a HMNS, which is supported by the centrifugal force and the thermal pressure is, formed. The neutrino luminosity in this HMNS phase is larger than that in the ordinary supernova as $\gtrsim 5 \times 10^{53}$ ergs/s. The HMNS eventually collapses to a BH irrespective of the initial rotational profiles. However, the dynamics and the geometry of the final outcome depend strongly on the degree of the initial rotation.

For the model UN100-rigid, the shock wave formed at the core bounce is de-

formed to be a torus-like shape. Then the infalling materials are accumulated in the central region after they pass through the oblique shock formed at the torus-shaped outer region of the HMNS. As a result, the thermal energy is efficiently stored at the surface of the HMNS due to the dissipation of the kinetic energy of the accumulated materials, driving outflows. After the collapse of the HMNS, a torus is formed around the BH. We found that the torus shows a time variability. The total neutrino luminosity emitted from the torus around the BH amounts to $L_{\nu,\text{tot}} \sim 10^{51}\text{--}10^{52}$ ergs/s, which lasts for a long duration of $\gtrsim 1$ s. Associated with the time variability of the BH-torus system, the neutrino luminosities also show a violent time variability. Such a long-term high luminosity with the time variation may be related to the time variability that LGRBs show. For the model UN100-diff, by contrast, a geometrically thin disk is formed around the BH and the BH-disk system shows essentially no time variability. Remarkably, the above differences in the dynamics and the outcome stem from a small difference in the initial rotational profile.

We also calculated the characteristic gravitational-wave strain h_{char} for UN100-rigid. The effective amplitude is as large as $\sim 10^{-20}$ at $f \sim 1$ kHz for a hypothetical event occurred at a distance of 10 kpc. This shows a possibility that we may observe multi-messenger information, namely, gravitational waves, neutrinos, and electromagnetic radiation from such a nearby event and may obtain a clue to understand the stellar core collapse and the central engine of LGRBs.

5.2. Binary neutron star merger

We showed that for a stiff, purely nucleonic EOS, a HMNS is the canonical outcome and a BH is not promptly formed after the onset of the merger as long as the total mass of the system is smaller than $3.2M_{\odot}$. The primary reason is that the thermal pressure plays an important role for sustaining the HMNS. We further showed that the lifetime of the formed HMNS with mass $\lesssim 3M_{\odot}$ would be much longer than its dynamical time scale, i.e., $\gg 10$ ms, and will be determined by the time scale of the subsequent neutrino cooling. The neutrino luminosity in the early evolution phase of the HMNS was shown to be high as $\sim 3\text{--}10 \times 10^{53}$ ergs/s. The effective amplitude of gravitational waves averaged over the random source direction and orbital plane inclination is $h_{\text{eff}} = 4\text{--}6 \times 10^{-22}$ at $f_{\text{peak}} = 2.1\text{--}2.5$ kHz for a hypothetical source distance of $D = 100$ Mpc. If the BNS merger happens at a relatively short source distance ~ 20 Mpc or is located in an optimistic direction with $D \sim 50$ Mpc, such gravitational waves may be detected by advanced gravitational-wave detectors with $S/N = 5$, and the HMNS formation will be confirmed.

For an EOS in which effects of hyperons are taken into account, the EOS becomes softer than the purely nucleonic EOS. With this EOS, a BH is often formed in a short time scale after the onset of the merger, although a HMNS could be a transient outcome with a short lifetime $\lesssim 10$ ms. Because the EOS becomes soft during the evolution of the HMNS, the compactness significantly changes in a short time scale in this EOS. This is well reflected in gravitational waveforms and their spectra. Specifically, the characteristic frequency changes with time. This effect reduces the amplitude at a peak frequency of gravitational waves in the Fourier space, and make a feature unfavorable for the detection of gravitational waves. Roughly speaking,

the allowed distance for the detection of gravitational waves from the HMNS is by a factor of 2 smaller than that in the nucleonic EOS for the same mass of BNS.

5.3. Future prospects

5.3.1. Massive stellar core collapse

As mentioned in § 3, we did not take into account effects of the neutrino heating in the numerical simulations to date. Recently, we have developed¹⁶⁾ a formulation for numerical simulations of general relativistic radiation transfer based on Thorne's moment formalism.⁴⁹⁾ Based on this formalism, we have already performed general relativistic radiation magnetohydrodynamics (GRRMHD) simulations⁹⁵⁾ for the evolution of a system composed of a BH and a surrounding torus with a simplified treatment of microphysics, as a step toward a more physical modelling. Furthermore, we have succeeded in implementing a code which can solve the neutrino transfer with a detailed microphysics (in preparation). Using this code, we plan to perform simulations of the stellar core collapse to explore a supernova explosion mechanism and the formation of a BH in full general relativity.

Throughout the study of the massive stellar collapse in this article, we assume the axial symmetry in the simulations. However, this assumption would be invalid if non-axisymmetric instabilities set in. For example, in Ref. 96), it has been shown that the BH-torus systems could exhibit the so-called Papaloizou-Pringle instability.⁹⁷⁾ Also, for a rapidly rotating HMNS, non-axisymmetric instabilities such as a bar-mode instability could set in.^{98), 99), 100), 101), 31)} Once these instabilities turn on, the torus/HMNS may deform to be a highly non-axisymmetric structure. This will enhance the angular momentum transport in the torus and HMNS, and the evolution processes of these systems may be modified. We plan to perform a three dimensional simulation to explore if the non-axisymmetric instabilities set in and play an important role for the collapsar models.

5.3.2. Binary neutron star merger

To date, we performed the BNS merger simulations for the case of the equal-mass binaries. As a straightforward extension of the previous studies, we plan to perform simulations for unequal-mass binaries, for which the merger dynamics, gravitational waveforms, and the mass of the disk will be modified. We also plan to perform merger simulations of BHNS binaries. It has been reported (see Ref. 102) and references therein) that a massive disk of $M_{\text{disk}} \gtrsim 0.1M_{\odot}$ can be formed for stiff EOSs even when the BH rotates moderately ($a_{\text{BH}} \gtrsim 0.5$). Such a system is a promising candidate of the central engine of SGRBs. Only simulations with detailed microphysics will enable a quantitative study for this merger hypothesis of SGRB.

In the study of the BNS merger simulation, we totally ignore the effect of magnetic fields. Recent studies on magnetized BNS merger showed that the magnetic fields in the merger and post-merger phases have an impact on the dynamics of the torus formed around the BH.⁸⁶⁾ This is because the angular velocity inside the torus has a steep gradient. Thus, the magnetic field is subject to the amplification via magnetic winding and/or magneto-rotational instability.¹⁰³⁾ This condition holds in the HMNS because it has strong and rapid differential rotation as discussed in § 4.2.

We plan to incorporate magneto-hydrodynamics in our code and explore its impact on the evolution of HMNSs.

Acknowledgments

We thank H. Umeda for providing us the presupernova model (UN100) adopted in this work. Numerical simulations were performed on SR16000 at YITP of Kyoto University, on SX9 and XT4 at CfCA of NAOJ, and on the NEC SX-8 at RCNP in Osaka University. This work was supported by Grant-in-Aid for Scientific Research (21018008, 21105511, 21340051, 21684014, 22740178, 23740160), Grant-in-Aid on Innovative Area (20105004), and HPCI Strategic Program of Japanese MEXT.

Appendix A

— Electron and positron captures —

In this section, we briefly summarize our methods of handling electron and positron captures based on Ref. 57), and give the explicit forms of $\gamma_{\nu_e}^{\text{ec}}$, $\gamma_{\bar{\nu}_e}^{\text{pc}}$, $Q_{\nu_e}^{\text{ec}}$, and $Q_{\bar{\nu}_e}^{\text{pc}}$ in Eqs. (2.63), (2.64), (2.66), and (2.67), for completeness

A.1. The electron and positron capture rates $\gamma_{\nu_e}^{\text{ec}}$ and $\gamma_{\bar{\nu}_e}^{\text{pc}}$

The 'net' electron fraction is written as $Y_e = Y_- - Y_+$ where Y_- (Y_+) denotes the number of electrons (positrons) per baryon including pair electrons. Then the electron-neutrino number emission rate by the electron capture and the electron-anti-neutrino number emission rate by the positron capture are given by

$$\gamma_{\nu_e}^{\text{local}} = -\dot{Y}_- = -(\dot{Y}_-^f + \dot{Y}_-^h), \quad (\text{A.1})$$

$$\gamma_{\bar{\nu}_e}^{\text{local}} = -\dot{Y}_+ = -(\dot{Y}_+^f + \dot{Y}_+^h), \quad (\text{A.2})$$

where the electron and positron capture rates are decomposed into two parts, capture on by free nucleons (with the superscript f) and on heavy nuclei (with the superscript h). In the following, we will present the explicit forms of \dot{Y}_-^f , \dot{Y}_+^f , \dot{Y}_-^h , and \dot{Y}_+^h .

A.2. Capture on free nucleons \dot{Y}^f

The electron capture rate (including the contribution of the inverse reaction of the neutrino capture) on free nucleons (\dot{Y}_-^f) is given by

$$\dot{Y}_-^f = X_n \lambda^{\nu_e c, f} - X_p \lambda^{\text{ec}, f}, \quad (\text{A.3})$$

where $\lambda^{\text{ec}, f}$ is the specific electron capture rate on free protons, $\lambda^{\nu_e c, f}$ is the specific electron-neutrino capture rate on free neutrons, and X_p and X_n are the mass fraction of free protons and neutrons, respectively. Based on a balance argument,⁵⁷⁾ one can show that $\lambda^{\nu_e c, f}$ is related to $\lambda^{\text{ec}, f}$ by

$$\lambda^{\nu_e c, f} = \exp\left(\eta_{\nu_e} - \eta_e - \frac{\delta m}{k_B T}\right) \lambda^{\text{ec}, f}, \quad (\text{A.4})$$

where η_{ν_e} and η_e are the chemical potentials of electron neutrinos and electrons in units of $k_B T$ and $\delta m = (m_n - m_p)c^2$. Furthermore, we use the following Saha's

relation for non-degenerate free nucleons,

$$X_n \approx X_p \exp \left(\eta_n - \eta_p + \frac{\delta m}{k_B T} \right), \quad (\text{A.5})$$

where η_n and η_p are the chemical potentials of free neutrons and protons in units of $k_B T$. Then we obtain

$$\dot{Y}_-^f = [\exp(\eta_{\nu_e} - \eta_e + \eta_n - \eta_p) - 1] X_p \lambda^{\text{ec},f}. \quad (\text{A.6})$$

The positron capture rate (including the contribution of the inverse reaction) on free nucleons is similarly given by

$$\dot{Y}_+^f = X_p \lambda^{\bar{\nu}_e c,f} - X_n \lambda^{\text{pc},f} = [\exp(\eta_{\bar{\nu}_e} + \eta_e + \eta_p - \eta_n) - 1] X_n \lambda^{\text{pc},f}, \quad (\text{A.7})$$

where $\eta_{\bar{\nu}_e}$ is the chemical potential of electron-anti-neutrinos in units of $k_B T$, λ^{pc} is the specific positron capture rate on free neutrons, and $\lambda^{\bar{\nu}_e c,f}$ is the specific electron-anti-neutrino capture rate on free protons.

A.3. Capture on heavy nuclei \dot{Y}^h

The electron capture rate (including the contribution of the inverse reaction of the neutrino capture) on a heavy nucleus of mass number A (\dot{Y}_-^h) is given by⁵⁷⁾

$$\dot{Y}_-^h = \frac{X_D}{A} \lambda^{\nu_e c,h} - \frac{X_P}{A} \lambda^{\text{ec},h}, \quad (\text{A.8})$$

where $\lambda^{\text{ec},h}$ is the specific electron capture rate on the parent nucleus (mass fraction X_P), $\lambda^{\nu_e c,h}$ is the specific electron-neutrino capture rate on the daughter nucleus (mass fraction X_D), and A is the atomic mass of the parent and daughter nuclei. In the present simulations, we set $X_D = X_P = X_A$. Then, under the assumption of a nuclear statistical equilibrium, one may approximate the capture rate on heavy nuclei as,⁵⁷⁾

$$\dot{Y}_-^h \approx [\exp(\eta_{\nu_e} - \eta_e + \eta_n - \eta_p) - 1] \frac{X_A}{A} \lambda^{\text{ec},h}. \quad (\text{A.9})$$

Similarly, the positron capture rate (including the contribution of the inverse reaction) on heavy nuclei (\dot{Y}_+^h) is given by

$$\dot{Y}_+^h = \frac{X_D}{A} \lambda^{\bar{\nu}_e c,h} - \frac{X_P}{A} \lambda^{\text{pc},h} \approx [\exp(\eta_{\bar{\nu}_e} + \eta_e + \eta_p - \eta_n) - 1] \frac{X_A}{A} \lambda^{\text{pc},h}. \quad (\text{A.10})$$

A.4. The specific capture rate λ

The specific electron and positron capture rates on free nucleons and on heavy nuclei are written in the same form as⁵⁷⁾

$$\lambda^{\text{ec},f} = \frac{\ln 2}{\langle ft \rangle_{\text{eff}}^{\text{ec},f}} I^{\text{ec},f}, \quad \lambda^{\text{pc},f} = \frac{\ln 2}{\langle ft \rangle_{\text{eff}}^{\text{pc},f}} I^{\text{pc},f}, \quad (\text{A.11})$$

$$\lambda^{\text{ec},h} = \frac{\ln 2}{\langle ft \rangle_{\text{eff}}^{\text{ec},h}} I^{\text{ec},h}, \quad \lambda^{\text{pc},h} = \frac{\ln 2}{\langle ft \rangle_{\text{eff}}^{\text{pc},h}} I^{\text{pc},h}, \quad (\text{A.12})$$

where $I^{\text{ec},f}$ and $I^{\text{pc},f}$ are the phase space factors for the electron and positron captures on free electrons, and $I^{\text{ec},h}$ and $I^{\text{pc},h}$ are those on heavy nuclei. $\langle ft \rangle_{\text{eff}}$'s are the effective ft -values introduced by Fuller et al.,⁵⁷⁾ which is essentially the same as the square of the nuclear transition matrix.

The phase space factors are given by

$$I^{\text{ec},f} = \left(\frac{k_B T}{m_e c^2} \right)^5 \int_{\eta_0}^{\infty} \eta^2 (\eta + \zeta^{\text{ec},f})^2 \frac{1}{1 + e^{\eta - \eta_e}} \left[1 - \frac{1}{1 + e^{\eta - \eta_{\nu_e} + \zeta^{\text{ec},f}}} \right] d\eta, \quad (\text{A}\cdot 13)$$

$$I^{\text{pc},f} = \left(\frac{k_B T}{m_e c^2} \right)^5 \int_{\eta_0}^{\infty} \eta^2 (\eta + \zeta^{\text{pc},f})^2 \frac{1}{1 + e^{\eta + \eta_e}} \left[1 - \frac{1}{1 + e^{\eta - \eta_{\bar{\nu}_e} + \zeta^{\text{pc},f}}} \right] d\eta, \quad (\text{A}\cdot 14)$$

$$I^{\text{ec},h} = \left(\frac{k_B T}{m_e c^2} \right)^5 \int_{\eta_0}^{\infty} \eta^2 (\eta + \zeta^{\text{ec},h})^2 \frac{1}{1 + e^{\eta - \eta_e}} \left[1 - \frac{1}{1 + e^{\eta - \eta_{\nu_e} + \zeta^{\text{ec},h}}} \right] d\eta, \quad (\text{A}\cdot 15)$$

$$I^{\text{pc},h} = \left(\frac{k_B T}{m_e c^2} \right)^5 \int_{\eta_0}^{\infty} \eta^2 (\eta + \zeta^{\text{pc},h})^2 \frac{1}{1 + e^{\eta + \eta_e}} \left[1 - \frac{1}{1 + e^{\eta - \eta_{\bar{\nu}_e} + \zeta^{\text{pc},h}}} \right] d\eta, \quad (\text{A}\cdot 16)$$

where $\zeta^{\text{ec},f}$, $\zeta^{\text{pc},f}$, $\zeta^{\text{ec},h}$, and $\zeta^{\text{pc},h}$ are the nuclear mass-energy differences for the electron and positron captures in units of $k_B T$. The superscripts 'f' and 'h' again denote free nucleons and heavy nuclei. The nuclear mass-energy differences for the capture on free nuclei are given by

$$\zeta^{\text{ec},f} = -\zeta_n^{\text{pc},f} \approx \eta_p - \eta_n. \quad (\text{A}\cdot 17)$$

We follow Fuller et al.⁵⁷⁾ for the nuclear mass-energy differences in the capture on heavy nuclei: In the case of $N < 40$ or $Z > 20$ (referred to as 'unblocked' case), we set

$$\zeta^{\text{ec},h} = -\zeta_n^{\text{pc},h} \approx \eta_p - \eta_n. \quad (\text{A}\cdot 18)$$

In the case of $N \geq 40$ or $Z \leq 20$ (referred to as 'blocked' case), on the other hand, we set

$$\zeta^{\text{ec},h} \approx \eta_p - \eta_n - \frac{5 \text{ MeV}}{k_B T}, \quad (\text{A}\cdot 19)$$

$$\zeta^{\text{pc},h} \approx -\eta_p + \eta_n + \frac{5 \text{ MeV}}{k_B T}. \quad (\text{A}\cdot 20)$$

Then, the threshold value of the electron and positron captures is given by $\eta_0 = m_e c^2 / (k_B T)$ for $\zeta > -m_e c^2 / (k_B T)$ and $\eta_0 = |\zeta|$ for $\zeta < -m_e c^2 / (k_B T)$ where we have dropped the superscripts 'ec', 'pc', 'f', and 'h' in ζ for simplicity.

The effective ft -value of the electron or positron capture on free nuclei is given by (e.g. Ref. 57)

$$\log_{10} \langle ft \rangle_{\text{eff}}^{\text{ec},f} = \log_{10} \langle ft \rangle_{\text{eff}}^{\text{pc},f} \approx 3.035. \quad (\text{A}\cdot 21)$$

We follow Fuller et al.⁵⁷⁾ for the effective ft -value of the capture on heavy nuclei, who proposed to use

$$\log_{10} \langle ft \rangle_{\text{eff}}^{\text{ec},h} \approx \begin{cases} 3.2 & \text{unblocked} & \eta_e < |\zeta^{\text{ec},h}| \\ 2.6 & \text{unblocked} & \eta_e > |\zeta^{\text{ec},h}| \\ 2.6 + \frac{25.9}{T_9} & \text{blocked} & \end{cases}, \quad (\text{A}\cdot 22)$$

$$\log_{10}\langle ft \rangle_{\text{eff}}^{\text{pc},h} \approx \begin{cases} 3.2 & \text{unblocked} & \eta_e < |\zeta^{\text{pc},h}| \\ 2.6 & \text{unblocked} & \eta_e > |\zeta^{\text{pc},h}| \\ 2.6 + \frac{25.9}{T_9} & \text{blocked} & \end{cases}, \quad (\text{A}\cdot 23)$$

where $T_9 = T/(10^9 K)$. In this expression, the thermal unblocking effect¹⁰⁴⁾ is readily taken into account. In the thermal unblocking, it costs ≈ 5.13 MeV to remove a neutron from a filled orbital $1f_{5/2}$ and place it in the gd -shell.⁵⁷⁾

A.5. Energy emission rates $Q_{\nu_e}^{\text{ec}}$ and $Q_{\bar{\nu}_e}^{\text{pc}}$

The neutrino energy emission rates associated with the electron and positron captures in units of $m_e c^2 \text{ s}^{-1}$ are given by⁵⁷⁾

$$\pi^{\text{ec}} = \ln 2 \frac{J^{\text{ec}}}{\langle ft \rangle_{\text{eff}}^{\text{ec}}}, \quad \pi^{\text{pc}} = \ln 2 \frac{J^{\text{pc}}}{\langle ft \rangle_{\text{eff}}^{\text{pc}}}, \quad (\text{A}\cdot 24)$$

where the phase space factors are given by

$$J^{\text{ec}} = \left(\frac{k_B T}{m_e c^2} \right)^6 \int_{\eta_0}^{\infty} \eta^2 (\eta + \zeta^{\text{ec}})^3 \frac{1}{1 + e^{\eta - \eta_e}} \left[1 - \frac{1}{1 - e^{\eta - \eta_{\nu_e} + \zeta^{\text{ec}}}} \right] d\eta, \quad (\text{A}\cdot 25)$$

$$J^{\text{pc}} = \left(\frac{k_B T}{m_e c^2} \right)^6 \int_{\eta_0}^{\infty} \eta^2 (\eta + \zeta^{\text{pc}})^3 \frac{1}{1 + e^{\eta + \eta_e}} \left[1 - \frac{1}{1 - e^{\eta - \eta_{\bar{\nu}_e} + \zeta^{\text{pc}}}} \right] d\eta. \quad (\text{A}\cdot 26)$$

In Eqs. (A·24)–(A·26), we have dropped the superscripts 'f' and 'h' in π^{ec} , π^{pc} , J^{ec} , J^{pc} , $\langle ft \rangle_{\text{eff}}^{\text{ec}}$, $\langle ft \rangle_{\text{eff}}^{\text{pc}}$, ζ^{ec} , and ζ^{pc} for simplicity.

The average energy of the electron neutrinos produced by electron and positron captures is defined, in units of $m_e c^2$, as

$$\langle \epsilon_{\nu_e} \rangle^{\text{ec}} = \frac{J^{\text{ec}}}{I^{\text{ec}}}, \quad \langle \epsilon_{\bar{\nu}_e} \rangle^{\text{pc}} = \frac{J^{\text{pc}}}{I^{\text{pc}}}. \quad (\text{A}\cdot 27)$$

Then, the local neutrino energy emission rates by the electron and positron captures per unit volume is given by

$$Q_{\nu_e}^{\text{ec}} = \frac{\rho}{m_u} \left[X_p \langle \epsilon_{\nu_e} \rangle^{\text{ec},f} \lambda^{\text{ec},f} + \frac{X_A}{A} \langle \epsilon_{\nu_e} \rangle^{\text{ec},h} \lambda^{\text{ec},h} \right], \quad (\text{A}\cdot 28)$$

$$Q_{\bar{\nu}_e}^{\text{pc}} = \frac{\rho}{m_u} \left[X_n \langle \epsilon_{\bar{\nu}_e} \rangle^{\text{pc},f} \lambda^{\text{pc},f} + \frac{X_A}{A} \langle \epsilon_{\bar{\nu}_e} \rangle^{\text{pc},h} \lambda^{\text{pc},h} \right]. \quad (\text{A}\cdot 29)$$

Appendix B

—— Neutrino pair processes ——

In this section, we briefly summarize our method of handling the pair processes of the neutrino emission and give the explicit forms of $\gamma_{\nu_e \bar{\nu}_e}^{\text{pair}}$, $\gamma_{\nu_e \bar{\nu}_e}^{\text{plas}}$, $\gamma_{\nu_e \bar{\nu}_e}^{\text{Brems}}$, $\gamma_{\nu_x \bar{\nu}_x}^{\text{pair}}$, $\gamma_{\nu_x \bar{\nu}_x}^{\text{Brems}}$, $Q_{\nu_e \bar{\nu}_e}^{\text{pair}}$, $Q_{\nu_e \bar{\nu}_e}^{\text{plas}}$, $Q_{\nu_e \bar{\nu}_e}^{\text{Brems}}$, $Q_{\nu_x \bar{\nu}_x}^{\text{pair}}$, $Q_{\nu_x \bar{\nu}_x}^{\text{plas}}$, and $Q_{\nu_x \bar{\nu}_x}^{\text{Brems}}$ for completeness.

B.1. Electron-positron pair annihilation

We follow Cooperstein et al.⁵⁸⁾ for computing the rate of neutrino emission by the electron-positron pair annihilation. The number emission rate of ν_e or $\bar{\nu}_e$ by the

electron-positron pair annihilation can be written as

$$\gamma_{\nu_e \bar{\nu}_e}^{\text{pair}} = \frac{m_u}{\rho} \frac{C_{\nu_e \bar{\nu}_e}^{\text{pair}}}{36\pi^4} \frac{\sigma_0 c}{m_e^2 c^4} \frac{(k_B T)^8}{(\hbar c)^6} F_3(\eta_e) F_3(-\eta_e) \langle \text{block} \rangle_{\nu_e \bar{\nu}_e}^{\text{pair}}, \quad (\text{B}\cdot 1)$$

where $\sigma_0 \approx 1.705 \times 10^{-44} \text{cm}^{-2}$ and $C_{\nu_e \bar{\nu}_e}^{\text{pair}} = (C_V - C_A)^2 + (C_V + C_A)^2$ with $C_V = \frac{1}{2} + 2\sin^2 \theta_W$ and $C_A = \frac{1}{2}$. The Weinberg angle is given by $\sin^2 \theta_W \approx 0.23$. Using the average energy of neutrinos produced by the pair annihilation,

$$\langle \epsilon_{\nu_e \bar{\nu}_e} \rangle^{\text{pair}} = \frac{k_B T}{2} \left(\frac{F_4(\eta_e)}{F_3(\eta_e)} + \frac{F_4(-\eta_e)}{F_3(-\eta_e)} \right), \quad (\text{B}\cdot 2)$$

the blocking factor $\langle \text{block} \rangle_{\nu_e \bar{\nu}_e}^{\text{pair}}$ is evaluated as

$$\langle \text{block} \rangle_{\nu_e \bar{\nu}_e}^{\text{pair}} \approx \left[1 + \exp \left(\eta_{\nu_e} - \frac{\langle \epsilon_{\nu_e \bar{\nu}_e} \rangle^{\text{pair}}}{k_B T} \right) \right]^{-1} \left[1 + \exp \left(\eta_{\bar{\nu}_e} - \frac{\langle \epsilon_{\nu_e \bar{\nu}_e} \rangle^{\text{pair}}}{k_B T} \right) \right]^{-1}. \quad (\text{B}\cdot 3)$$

The associated neutrino energy emission rate by the pair annihilation is given by

$$Q_{\nu_e \bar{\nu}_e}^{\text{pair}} = \frac{\rho}{m_u} \gamma_{\nu_e \bar{\nu}_e}^{\text{pair}} \langle \epsilon_{\nu_e \bar{\nu}_e} \rangle^{\text{pair}}. \quad (\text{B}\cdot 4)$$

Similarly, the number emission rate of ν_x or $\bar{\nu}_x$ by the electron-positron pair annihilation and the associated energy emission rate are given by

$$\gamma_{\nu_x \bar{\nu}_x}^{\text{pair}} = \frac{m_u}{\rho} \frac{C_{\nu_x \bar{\nu}_x}^{\text{pair}}}{36\pi^4} \frac{\sigma_0 c}{m_e^2 c^4} \frac{(k_B T)^8}{(\hbar c)^6} F_3(\eta_e) F_3(-\eta_e) \langle \text{block} \rangle_{\nu_x \bar{\nu}_x}^{\text{pair}}, \quad (\text{B}\cdot 5)$$

$$Q_{\nu_x \bar{\nu}_x}^{\text{pair}} = \frac{\rho}{m_u} \gamma_{\nu_x \bar{\nu}_x}^{\text{pair}} \langle \epsilon_{\nu_x \bar{\nu}_x} \rangle^{\text{pair}}, \quad (\text{B}\cdot 6)$$

where $C_{\nu_x \bar{\nu}_x} = (C_V - C_A)^2 + (C_V + C_A - 2)^2$. The average neutrino energy and the blocking factor are given by

$$\langle \epsilon_{\nu_x \bar{\nu}_x} \rangle^{\text{pair}} = \langle \epsilon_{\nu_e \bar{\nu}_e} \rangle^{\text{pair}}, \quad (\text{B}\cdot 7)$$

and

$$\langle \text{block} \rangle_{\nu_x \bar{\nu}_x}^{\text{pair}} \approx \left[1 + \exp \left(\eta_{\nu_x} - \frac{\langle \epsilon_{\nu_x \bar{\nu}_x} \rangle^{\text{pair}}}{k_B T} \right) \right]^{-1} \left[1 + \exp \left(\eta_{\bar{\nu}_x} - \frac{\langle \epsilon_{\nu_x \bar{\nu}_x} \rangle^{\text{pair}}}{k_B T} \right) \right]^{-1}, \quad (\text{B}\cdot 8)$$

where $\eta_{\bar{\nu}_x} = \eta_{\nu_x}$ because they are produced only by the pair processes.

B.2. Plasmon decay

We follow Ruffert et al.²¹⁾ for computing the pair creation rate of neutrinos by the decay of transversal plasmons. The number emission rate of ν_e or $\bar{\nu}_e$ can be written as

$$\gamma_{\nu_e \bar{\nu}_e}^{\text{plas}} = \frac{m_u}{\rho} \frac{C_V^2}{192\pi^3 \alpha_{\text{fine}}} \frac{\sigma_0 c}{m_e^2 c^4} \frac{(k_B T)^8}{(\hbar c)^6} \gamma_p^6 e^{-\gamma_p} (1 + \gamma_p) \langle \text{block} \rangle_{\nu_e \bar{\nu}_e}^{\text{plas}}, \quad (\text{B}\cdot 9)$$

where $\alpha_{\text{fine}} \approx 1/137$ is the fine-structure constant and $\gamma_p \approx 2\sqrt{(\alpha_{\text{fine}}/9\pi)(\pi^2 + 3\eta_e)}$. The blocking factor is approximately given by

$$\langle \text{block} \rangle_{\nu_e \bar{\nu}_e}^{\text{plas}} \approx \left[1 + \exp \left(\eta_{\nu_e} - \frac{\langle \epsilon_{\nu_e \bar{\nu}_e} \rangle^{\text{plas}}}{k_B T} \right) \right]^{-1} \left[1 + \exp \left(\eta_{\bar{\nu}_e} - \frac{\langle \epsilon_{\nu_e \bar{\nu}_e} \rangle^{\text{plas}}}{k_B T} \right) \right]^{-1}, \quad (\text{B}\cdot 10)$$

where

$$\langle \epsilon_{\nu_e \bar{\nu}_e} \rangle^{\text{plas}} = \frac{k_B T}{2} \left(2 + \frac{\gamma_p^2}{1 + \gamma_p} \right) \quad (\text{B}\cdot 11)$$

is the average energy of neutrinos produced by the plasmon decay. The associated neutrino energy emission rate is given by

$$Q_{\nu_e \bar{\nu}_e}^{\text{plas}} = \frac{\rho}{m_u} \gamma_{\nu_e \bar{\nu}_e}^{\text{plas}} \langle \epsilon_{\nu_e \bar{\nu}_e} \rangle^{\text{plas}}. \quad (\text{B}\cdot 12)$$

Similarly, the number emission rate of ν_x or $\bar{\nu}_x$ by the plasmon decay and the associated energy emission rate are given by

$$\gamma_{\nu_x \bar{\nu}_x}^{\text{plas}} = \frac{m_u}{\rho} \frac{(C_V - 1)^2}{192\pi^3 \alpha_{\text{fine}}} \frac{\sigma_0 c}{m_e^2 c^4} \frac{(k_B T)^8}{(\hbar c)^6} \gamma_p^6 e^{-\gamma_p} (1 + \gamma_p) \langle \text{block} \rangle_{\nu_x \bar{\nu}_x}^{\text{plas}}, \quad (\text{B}\cdot 13)$$

$$Q_{\nu_x \bar{\nu}_x}^{\text{plas}} = \frac{\rho}{m_u} \gamma_{\nu_x \bar{\nu}_x}^{\text{plas}} \langle \epsilon_{\nu_x \bar{\nu}_x} \rangle^{\text{plas}}, \quad (\text{B}\cdot 14)$$

where the average neutrino energy is $\langle \epsilon_{\nu_x \bar{\nu}_x} \rangle^{\text{plas}} = \langle \epsilon_{\nu_e \bar{\nu}_e} \rangle^{\text{plas}}$ and the blocking factor is given by

$$\langle \text{block} \rangle_{\nu_x \bar{\nu}_x}^{\text{pair}} \approx \left[1 + \exp \left(\eta_{\nu_x} - \frac{\langle \epsilon_{\nu_x \bar{\nu}_x} \rangle^{\text{plas}}}{k_B T} \right) \right]^{-1} \left[1 + \exp \left(\eta_{\bar{\nu}_x} - \frac{\langle \epsilon_{\nu_x \bar{\nu}_x} \rangle^{\text{plas}}}{k_B T} \right) \right]^{-1}. \quad (\text{B}\cdot 15)$$

B.3. Nucleon-nucleon bremsstrahlung

We follow Burrows et al.⁵⁹⁾ for computing the pair creation rate of neutrinos by the nucleon-nucleon bremsstrahlung radiation. They derived the neutrino energy emission rate associated with the pair creation of ν_x or $\bar{\nu}_x$ by the nucleon-nucleon bremsstrahlung radiation without the blocking factor as

$$Q_{\nu_x \bar{\nu}_x}^{\text{Brems},0} = 3.62 \times 10^5 \zeta^{\text{Brems}} \left(X_n^2 + X_p^2 + \frac{28}{3} X_n X_p \right) \rho^2 \left(\frac{k_B T}{m_e c^2} \right)^{4.5} \langle \epsilon_{\nu_x \bar{\nu}_x} \rangle^{\text{Brems}}, \quad (\text{B}\cdot 16)$$

where $\zeta^{\text{Brems}} \sim 0.5$ is a correction factor and the average energy is

$$\langle \epsilon_{\nu_x \bar{\nu}_x} \rangle^{\text{Brems}} \approx 4.36 k_B T. \quad (\text{B}\cdot 17)$$

To obtain the 'blocked' neutrino energy emission rate we multiply the blocking factor,

$$\langle \text{block} \rangle_{\nu_x \bar{\nu}_x}^{\text{Brems}} \approx \left[1 + \exp \left(\eta_{\nu_x} - \frac{\langle \epsilon_{\nu_x \bar{\nu}_x} \rangle^{\text{Brems}}}{k_B T} \right) \right]^{-1} \left[1 + \exp \left(\eta_{\bar{\nu}_x} - \frac{\langle \epsilon_{\nu_x \bar{\nu}_x} \rangle^{\text{Brems}}}{k_B T} \right) \right]^{-1}, \quad (\text{B}\cdot 18)$$

to give

$$Q_{\nu_x \bar{\nu}_x}^{\text{Brems}} = Q_{\nu_x \bar{\nu}_x}^{\text{Brems},0} \langle \text{block} \rangle_{\nu_x \bar{\nu}_x}^{\text{Brems}}. \quad (\text{B} \cdot 19)$$

The number emission rate of ν_x or $\bar{\nu}_x$ is readily given by

$$\gamma_{\nu_x \bar{\nu}_x}^{\text{Brems}} = 3.62 \times 10^5 \zeta^{\text{Brems}} \left(X_n^2 + X_p^2 + \frac{28}{3} X_n X_p \right) m_u \rho \left(\frac{k_B T}{m_e c^2} \right)^{4.5} \langle \text{block} \rangle_{\nu_x \bar{\nu}_x}^{\text{Brems}}. \quad (\text{B} \cdot 20)$$

Noting that the weak interaction coefficients of the bremsstrahlung radiation are¹⁰⁵⁾ $(1 - C_V)^2 + (1 - C_A)^2$ for the pair creation of $\nu_x \bar{\nu}_x$ and $C_V^2 + C_A^2$ for the pair creation of $\nu_e \bar{\nu}_e$, the number emission rate and the associated energy emission rate for ν_e or $\bar{\nu}_e$ are written as

$$\gamma_{\nu_e \bar{\nu}_e}^{\text{Brems}} = \frac{C_V^2 + C_A^2}{(1 - C_V)^2 + (1 - C_A)^2} \gamma_{\nu_x \bar{\nu}_x}^{\text{Brems}}, \quad (\text{B} \cdot 21)$$

$$Q_{\nu_e \bar{\nu}_e}^{\text{Brems}} = \frac{C_V^2 + C_A^2}{(1 - C_V)^2 + (1 - C_A)^2} Q_{\nu_x \bar{\nu}_x}^{\text{Brems}}. \quad (\text{B} \cdot 22)$$

Appendix C

—— Neutrino diffusion rates ——

We follow Ref. 22) for computing the diffusive neutrino-number emission rate $\gamma_{(\nu)}^{\text{diff}}$ and the associated energy emission rate $Q_{(\nu)}^{\text{diff}}$ in Eqs. (2·54) and (2·55). An alternative definition of the diffusion rates are found in Ref. 21).

C.1. Neutrino diffusion rates

To calculate the neutrino diffusion rates $\gamma_{(\nu)}^{\text{diff}}$ and $Q_{(\nu)}^{\text{diff}}$, we first define the neutrino diffusion time. In this paper, we consider cross sections for scattering on nuclei ($\sigma_{\nu A}^{\text{sc}}$), and on free nucleons ($\sigma_{\nu p}^{\text{sc}}$ and $\sigma_{\nu n}^{\text{sc}}$), as well as that for absorption on free nucleons ($\sigma_{\nu n}^{\text{ab}}$ and $\sigma_{\nu p}^{\text{ab}}$).

Ignoring the higher-order correction terms in neutrino energy E_ν , these neutrino cross sections can be written in general as

$$\sigma(E_\nu) = E_\nu^2 \tilde{\sigma}, \quad (\text{C} \cdot 1)$$

where $\tilde{\sigma}$ is a 'cross section' in which E_ν^2 dependence is factored out. In practice, the cross sections contain the correction terms which cannot be expressed in the form of Eq. (C·1). We take account of these correction terms, approximating neutrino-energy dependence on temperature according to

$$E_\nu \approx k_B T \frac{F_3(\eta_\nu)}{F_2(\eta_\nu)}. \quad (\text{C} \cdot 2)$$

The opacity is written as

$$\kappa(E_\nu) = \sum \kappa_i(E_\nu) = E_\nu^2 \sum \tilde{\kappa}_i = E_\nu^2 \tilde{\kappa}, \quad (\text{C} \cdot 3)$$

and the corresponding optical depth is calculated by

$$\tau(E_\nu) = \int \kappa(E_\nu) ds = E_\nu^2 \int \tilde{\kappa} ds = E_\nu^2 \tilde{\tau}. \quad (\text{C}\cdot 4)$$

Then, we define the neutrino diffusion time by

$$T_\nu^{\text{diff}}(E_\nu) \equiv a^{\text{diff}} \frac{\Delta x(E_\nu)}{c} \tau(E_\nu) = E_\nu^2 a^{\text{diff}} \frac{\tilde{\tau}^2}{c\tilde{\kappa}} = E_\nu^2 \tilde{T}_\nu^{\text{diff}}, \quad (\text{C}\cdot 5)$$

where the distance parameter $\Delta x(E_\nu)$ is given by

$$\Delta x(E_\nu) = \frac{\tau(E_\nu)}{\kappa(E_\nu)}. \quad (\text{C}\cdot 6)$$

Note that $\tilde{T}_\nu^{\text{diff}}$ can be calculated only using matter quantities. Here, a^{diff} is a parameter which controls how many neutrinos diffuse outward and we chose it to be 3 following Ref. 21). For a larger value of a^{diff} , the corresponding neutrino emission rate due to diffusion becomes smaller.

Finally, we define the neutrino diffusion rates by

$$\gamma_{(\nu)}^{\text{diff}} \equiv \frac{m_u}{\rho} \int \frac{n_\nu(E_\nu)}{T_\nu^{\text{diff}}(E_\nu)} dE_\nu = \frac{1}{a^{\text{diff}}} \frac{m_u}{\rho} \frac{4\pi c g_\nu}{(hc)^3} \frac{\tilde{\kappa}}{\tilde{\tau}^2} T F_0(\eta_\nu), \quad (\text{C}\cdot 7)$$

$$Q_{(\nu)}^{\text{diff}} \equiv \int \frac{E_\nu n_\nu(E_\nu)}{T_\nu^{\text{diff}}(E_\nu)} dE_\nu = \frac{1}{a^{\text{diff}}} \frac{4\pi c g_\nu}{(hc)^3} \frac{\tilde{\kappa}}{\tilde{\tau}^2} T^2 F_1(\eta_\nu). \quad (\text{C}\cdot 8)$$

C.2. Summary of cross sections

In this subsection, we briefly summarize the cross sections adopted in the present neutrino leakage scheme.

C.2.1. Neutrino nucleon scattering

The total ν - p scattering cross section σ_p for all neutrino species is given by

$$\sigma_{\nu p}^{\text{sc}} = \frac{\sigma_0}{4} \left(\frac{E_\nu}{m_e c^2} \right)^2 [(C_V - 1)^2 + 3g_A^2(C_A - 1)^2] W_p^{\text{sc}}(E_\nu), \quad (\text{C}\cdot 9)$$

where g_A is the axial-vector coupling constant $g_A \approx -1.26$. W_p^{sc} is the correction for the proton recoil. We use the exact expression derived by Horowitz¹⁰⁶⁾ for high neutrino energies $E_\nu/m_p c^2 \gtrsim 0.01$. However, the exact expression has a behavior which is inconvenient to treat numerically (such as 0/0). Thus we adopt expanded forms of the exact expression in low neutrino energies $E_\nu/m_p c^2 \lesssim 0.01$, which give

$$W_p^{\text{sc}}(E_\nu) \approx 1 - 1.524 \frac{E_\nu}{m_p c^2} + 1.451 \left(\frac{E_\nu}{m_p c^2} \right)^2, \quad (\text{C}\cdot 10)$$

$$W_p^{\text{sc}}(E_{\bar{\nu}}) \approx 1 - 6.874 \frac{E_{\bar{\nu}}}{m_p c^2} + 29.54 \left(\frac{E_{\bar{\nu}}}{m_p c^2} \right)^2, \quad (\text{C}\cdot 11)$$

for neutrinos and anti-neutrinos, respectively. Note that in the case of black hole formation, the neutrino energy becomes large and this correction becomes important.

On the other hand, the total $\nu - n$ scattering cross section σ_n is

$$\sigma_{\nu n}^{\text{sc}} = \frac{\sigma_0}{16} \left(\frac{E_\nu}{m_e c^2} \right)^2 [1 + 3g_A^2] W_n^{\text{sc}}. \quad (\text{C}\cdot 12)$$

We evaluate W_n^{sc} by the same method as for W_p^{sc} . The expanded forms in the low neutrino energies are

$$W_n^{\text{sc}}(E_\nu) \approx 1 - 0.7659 \frac{E_\nu}{m_n c^2} - 1.3947 \left(\frac{E_\nu}{m_n c^2} \right)^2, \quad (\text{C}\cdot 13)$$

$$W_n^{\text{sc}}(E_{\bar{\nu}}) \approx 1 - 7.366 \frac{E_{\bar{\nu}}}{m_n c^2} + 33.25 \left(\frac{E_{\bar{\nu}}}{m_n c^2} \right)^2, \quad (\text{C}\cdot 14)$$

for neutrinos and anti-neutrinos, respectively.

C.2.2. Coherent scattering of neutrinos on nuclei

The differential cross section for the ν - A neutral current scattering is written as⁵⁹⁾

$$\frac{d\sigma_A^{\text{sc}}}{d\Omega} = \frac{\sigma_0}{64\pi} \left(\frac{E_\nu}{m_e c^2} \right)^2 A^2 [\mathcal{W}\mathcal{C}_{\text{FF}} + \mathcal{C}_{\text{LOS}}]^2 \langle \mathcal{S}_{\text{ion}} \rangle (1 + \cos \theta), \quad (\text{C}\cdot 15)$$

where θ is the azimuthal angle of the scattering and

$$\mathcal{W} = 1 - \frac{2Z}{A}(1 - 2\sin^2 \theta_W). \quad (\text{C}\cdot 16)$$

$\langle \mathcal{S}_{\text{ion}} \rangle$, \mathcal{C}_{LOS} , and \mathcal{C}_{FF} are correction factors due to the Coulomb interaction among the nuclei,¹⁰⁷⁾ due to the electron polarization,¹⁰⁸⁾ and due to the finite size of heavy nuclei.¹⁰⁹⁾ Because it is known that the correction factor \mathcal{C}_{LOS} is important only for low-energy neutrinos,⁵⁹⁾ we consider only $\langle \mathcal{S}_{\text{ion}} \rangle$ and \mathcal{C}_{FF} .

The correction factor due to the Coulomb interaction among the nuclei is given by

$$\langle \mathcal{S}_{\text{ion}} \rangle = \frac{3}{4} \int_{-1}^1 d\cos \theta (1 + \cos \theta)(1 - \cos \theta) S_{\text{ion}}. \quad (\text{C}\cdot 17)$$

Itoh et al.¹¹¹⁾ presented a detailed fitting formula for the correction factor. However, the fitting formula is so complicated that we use a simple approximation based on Ref. 112), in which

$$S_{\text{ion}} \approx \frac{(qa_I)^2}{3\Gamma + f(\Gamma)(qa_I)^2}, \quad (\text{C}\cdot 18)$$

where $q = (2E_\nu/\hbar c) \sin(\theta/2)$, $a_I = (4\pi n_A/3)^{-1/3}$ is the ion-sphere radius, n_A is the number density of a nucleus, $\Gamma = (Ze)^2/(a_I k_B T)$ is the conventional parameter that characterizes the strongness of the Coulomb interaction, and $f(\Gamma)$ is given by¹¹¹⁾

$$f(\Gamma) \approx 0.73317 - 0.39890\Gamma + 0.34141\Gamma^{1/4} + 0.05484\Gamma^{-1/4}. \quad (\text{C}\cdot 19)$$

The integration approximately gives for $x \equiv E_\nu a_I/(\hbar c) < 1$

$$\langle \mathcal{S}_{\text{ion}} \rangle \approx \frac{1}{6} \frac{1}{\Gamma} x^2 - \frac{1}{30} \frac{f(\Gamma)}{\Gamma^2} x^4 + \frac{1}{135} \frac{(f(\Gamma))^2}{\Gamma^3} x^6 - \frac{1}{567} \frac{(f(\Gamma))^3}{\Gamma^4} x^8 + \frac{1}{2268} \frac{(f(\Gamma))^4}{\Gamma^5} x^{10}. \quad (\text{C}\cdot 20)$$

To use this expression for the case of $x \geq 1$, we set the maximum value as $\langle \mathcal{S}_{\text{ion}} \rangle = \max(1, \langle \mathcal{S}_{\text{ion}} \rangle)$ where $\langle \mathcal{S}_{\text{ion}} \rangle = 1$ corresponds to the case without the correction.

C.2.3. Absorption on free neutrons

The total cross section of the absorption of electron neutrinos on free neutrons is given by⁵⁹⁾

$$\sigma_n^{\text{ab}} = \sigma_0 \left(\frac{1 + 3g_A^2}{4} \right) \left(\frac{E_\nu + \Delta_{\text{np}}}{m_e c^2} \right)^2 \left[1 - \left(\frac{m_e c^2}{E_\nu + \Delta_{\text{np}}} \right) \right] W_n^{\text{ab}}, \quad (\text{C} \cdot 21)$$

where $\Delta_{\text{np}} = m_n c^2 - m_p c^2$, and W_n^{ab} is the correction for weak magnetism and recoil of neutron. We use the exact expression derived by Horowitz.¹⁰⁶⁾ By contrast with the corrections in the scattering cross section on free nucleons, the corrections in the absorption do not show the bad behavior at low neutrino energies. Similarly, the total cross section of the absorption of electron anti-neutrinos on free protons is given by⁵⁹⁾

$$\sigma_p^{\text{ab}} = \sigma_0 \left(\frac{1 + 3g_A^2}{4} \right) \left(\frac{E_{\bar{\nu}} - \Delta_{\text{np}}}{m_e c^2} \right)^2 \left[1 - \left(\frac{m_e c^2}{E_{\bar{\nu}} - \Delta_{\text{np}}} \right) \right] W_p^{\text{ab}}. \quad (\text{C} \cdot 22)$$

Again, we use the exact expression derived by Horowitz¹⁰⁶⁾ for W_p^{ab} .

References

- 1) J. Abadie, et al., Nucl. Instrum. Methods Phys. Res. Sect. **A624** (2010), 223.
- 2) T. Accadia, et al., Class. Quant. Grav. **28** (2011), 025005.
- 3) K. Kuroda, et al., Class. Quant. Grav. **27** (2010), 084004.
- 4) T. Piran, Rev. Mod. Phys. **76** (2005), 1143.
- 5) K. Nakazato, K. Sumiyoshi, and S. Yamada, Astrophys. J. **666** (2007), 1140.
- 6) e.g., K. Sumiyoshi, S. Yamada, H. Suzuki, and S. Chiba, Phys. Rev. Lett. **97** (2006), 091101; M. Liebendörfer, A. Mezzacappa, F.-K. Thielemann, O. E. Messer, W. R. Hix, and S. W. Bruenn, Phys. Rev. D **63** (2001), 103004.
- 7) C. D. Ott, H. Dimmelmeier, A. Marek, H.-T. Janka, I. Hawke, B. Zink, and E. Schnetter, Phys. Rev. Lett. **98** (2007), 261101.
- 8) H. Dimmelmeier, C. D. Ott, H.-Th. Janka, A. Marek, and E. Müller, Phys. Rev. Lett. **98** (2007), 251101.
- 9) H. Shen, H. Toki, K. Oyamatsu, and K. Sumiyoshi, Nucl. Phys. A **637** (1998), 435; Prog. Theor. Phys. **100** (1998), 1013.
- 10) M. Liebendörfer, Astrophys. J. **633** (2005), 1042.
- 11) Y. Sekiguchi, Prog. Theor. Phys. **124** (2010), 331; Class. Quant. Grav. **27** (2010), 331.
- 12) Y. Sekiguchi and M. Shibata, Astrophys. J. **737** (2011), 6.
- 13) B. Müller, H.-T. Janka, and H. Dimmelmeier, Astrophys. J. Suppl. **189** (2010), 10; B. Müller, H.-T. Janka, and A. Marek, arXiv:1202.0815.
- 14) I. Cordero-Carrión, et al., Phys. Rev. D **79** (2009), 024017.
- 15) T. Kuroda, K. Kotake, and T. Takiwaki, arXiv:1202.2487.
- 16) M. Shibata, K. Kiuchi, Y. Sekiguchi, and Y. Suwa, Prog. Theor. Phys. **125** (2011), 1255.
- 17) C. D. Ott, et al., arXiv:1204.0512.
- 18) J. Isenberg and J. Nester, *Canonical Gravity*, in *General Relativity and Gravitation, one hundred Years after the Birth of Albert Einstein*, ed. A. Held, Plenum Press (New York, 1980); J. R. Wilson, G. J. Mathews, and P. Marronetti, Phys. Rev. D **54** (1996), 1317.
- 19) R. Oechslin and H. T. Janka, Phys. Rev. Lett. **99** (2007), 121102; R. Oechslin, H. T. Janka, and A. Marek, Astron. Astrophys. **467** (2007), 395.
- 20) J. M. Lattimer and F. D. Swesty, Nucl. Phys. A **535** (1991), 331.
- 21) M. Ruffert, H.-Th. Janka, and G. Schäfer, Astron. Astrophys. **311** (1996), 532; M. Ruffert and H.-Th. Janka, Astron. Astrophys. **380** (2001), 554.

- 22) S. Rosswog and M. Liebendörfer, Mon. Not. R. Astron. Soc. **342** (2003), 673.
- 23) M. D. Duez, F. Foucart, L. E. Kidder, C. D. Ott, and S. A. Teukolsky, Class. Quant. Grav. **27** (2010), 114106.
- 24) A. Bauswein, et al., arXiv:1204.1888; A. Bauswein and H.-Th. Janka, Phys. Rev. Lett. **108** (2012), 011101.
- 25) H. Shen, H. Toki, K. Oyamatsu, and K. Sumiyoshi, Astrophys. J. Suppl. **197** (2011), 20.
- 26) Y. Sekiguchi and M. Shibata, in preparation.
- 27) Y. Sekiguchi, K. Kiuchi, K. Kyutoku, and M. Shibata, Phys. Rev. Lett. **107** (2011), 051102.
- 28) Y. Sekiguchi, K. Kiuchi, K. Kyutoku, and M. Shibata, Phys. Rev. Lett. **107** (2011), 211101.
- 29) K. Kotake, arXiv:1110.5107.
- 30) C. D. Ott, Class. Quant. Grav. **26** (2009), 6.
- 31) C. Fryer and K. C. B. New, Living. Rev. Relat. **14** (2011), 1.
- 32) M. Shibata and K. Taniguchi, Living. Rev. Relat. **14** (2011), 6.
- 33) D. Duez, Class. Quant. Grav. **27** (2010), 114002.
- 34) J. A. Faber and F. A. Rasio, to appear in Living Reviews in Relativity, arXiv:1204.3858.
- 35) J. M. Centrella, J. G. Baker, B. J. Kelly, J. R. van Meter, Rev. Mod. Phys. **82** (2010), 3069; Ann. Rev. Nucl. Part. Sci. **60** (2010), 75.
- 36) F. Pretorius, *Binary Black Hole Coalescence in Physics of Relativistic Objects in Compact Binaries: From Birth to Coalescence*, eds. M. Colpi, P. Casella, V. Gorini, U. Moschella, and A. Possenti, Springer (Netherlands, 2009), arXiv:0710.1338.
- 37) J. K. York, *Kinematics and Dynamics of General Relativity*, in *Sources of Gravitational Radiation*, ed. L. Smarr, Cambridge University Press (Cambridge, 1979).
- 38) M. Shibata and T. Nakamura, Phys. Rev. D **52** (1995), 5428.
- 39) T. W. Baumgarte and S. L. Shapiro, Phys. Rev. D **59** (1999), 024007.
- 40) M. Campanelli, C. O. Lousto, P. Marronetti, and Y. Zlochower, Phys. Rev. Lett. **96** (2006), 111101.
- 41) P. Marronetti, W. Tichy, B. Brügmann, J. González, and U. Sperhake, Phys. Rev. D **77** (2008), 064010.
- 42) T. Yamamoto, M. Shibata, and K. Taniguchi, Phys. Rev. D **78** (2008), 064054.
- 43) C. Bona, J. Masso, E. Seidel, and J. Stela, Phys. Rev. Lett. **75** (1995), 600.
- 44) M. Alcubierre and B. Brügmann, Phys. Rev. D **63** (2001), 104006.
- 45) S. W. Bruenn, Astrophys. J. Suppl. **58** (1985), 771.
- 46) M. Shibata, Astrophys. J. **595** (2003), 992.
- 47) A. Kurganov and E. Tadmor, J. Comp. Phys. **160** (2000), 241.
- 48) M. Liebendörfer, S. C. Whitehouse, and T. Fischer, Astrophys. J. **698** (2009), 1174.
- 49) K. S. Thorne, Mon. Not. Roy. Astron. Soc. **194** (1981), 439.
- 50) Y. Sugahara and H. Toki, Nucl. Phys. A **579** (1994), 557; B. D. Serot and J. D. Walecka, Adv. Nucl. Phys. **16** (1986), 1.
- 51) P. Demorest, T. Pennucci, S. Ransom, W. Roberts, and J. Hessels, Nature **467** (2010), 1081.
- 52) K. Sumiyoshi, S. Yamada, and H. Suzuki, Astrophys. J. **667** (2007), 382; Astrophys. J. **688** (2008), 1176.
- 53) K. Nakazato, K. Sumiyoshi, and S. Yamada, Phys. Rev. D **77** (2008), 103006.
- 54) J. P. Cox and R. T. Giuli, *Principles of Stellar Structure*, Gordon and Breach (New York, 1968).
- 55) M. Shibata, Y. Sekiguchi, and R. Takahashi, Prog. Theor. Phys. **118** (2007), 257.
- 56) J. Cooperstein, Phys. Rep. **163** (1988), 95.
- 57) G. M. Fuller, W. A. Fowler, and M. J. Newman, Astrophys. J. **293** (1985), 1.
- 58) J. Cooperstein, L. J. van den Horn, and E. A. Baron, Astrophys. J. **309** (1986), 653.
- 59) A. Burrows, S. Reddy, and T. A. Thompson, Nucl. Phys. A **777** (2006), 356.
- 60) S. E. Woosley and J. S. Bloom, Annu. Rev. Astron. Astrophys. **44** (2006), 507.
- 61) S. E. Woosley, Astrophys. J. **405** (1993), 273.
- 62) A. I. MacFadyen and S. E. Woosley, Astrophys. J. **524** (1999), 262.
- 63) W. Zhang and S. E. Woosley, Astrophys. J. **608** (2004), 365.
- 64) S. E. Woosley and A. Heger, Astrophys. J. **637** (2006), 914.
- 65) C. L. Fryer et al., Publi. Astron. Soc. Pacific **119** (2007), 1211.
- 66) H. Umeda and K. Nomoto, Astrophys. J. **673** (2008), 1014.
- 67) e.g., E. O'Connor and C. D. Ott, Astrophys. J. **730** (2011), 70.

- 68) M. Shibata, Prog. Theor. Phys. **104** (2000), 325; Phys. Rev. D **67** (2003), 024033.
- 69) M. Alcubierre, B. Brügmann, D. Holz, R. Takahashi, S. Brandt, E. Seidel, J. Thornburg, and A. Ashtekar, Int. J. Mod. Phys. D **10** (2001), 273.
- 70) M. Shibata and S. L. Shapiro, Astrophys. J. Lett. **572** (2002), L39.
- 71) Y. Sekiguchi and M. Shibata, Phys. Rev. D **71** (2005), 084013; Prog. Theor. Phys. **117** (2007), 1029.
- 72) H. A. Bethe, Rev. Mod. Phys. **62** (1990), 801.
- 73) E. E. Flanagan and S. A. Hughes, Phys. Rev. D **57** (1998), 4535.
- 74) M. Shibata and Y. Sekiguchi, Phys. Rev. D **68** (2003), 104020.
- 75) <https://dcc.ligo.org/cgi-bin/DocDB/ShowDocument?docid=2974>
- 76) A. M. Beloborodov, in AIP Conf. Proc. 1054, Cool Discs, Hot Flows: The Varying Faces of Accreting Compact Objects, ed. M. Axelsson (Melville, NY: AIP, 2008), 51.
- 77) R. Mochkovitch, M. Hernanz, J. Isern, and X. Martin, Nature **361** (1993), 236.
- 78) T. Liu, W.-M. Gu, Z.-G. Dai, and J.-F. Lu, Astrophys. J. **709** (2010), 851.
- 79) I. Zalamea and A. M. Beloborodov, Mon. Not. Roy. Astron. Soc. **410** (2011), 2302.
- 80) R. B. P. Narayan and T. Piran, Astrophys. J. Lett. **395** (1992), 83.
- 81) E. Nakar, Phys. Rep. **442** (2007), 166.
- 82) M. Shibata and K. Uryū, Phys. Rev. D **61** (2000), 064001.
- 83) See, e.g., S. L. Shapiro and S. A. Teukolsky, *Black Holes, White Dwarfs, and Neutron Stars*, Wiley Interscience (New York, 1983).
- 84) M. Shibata, K. Taniguchi, and K. Uryū, Phys. Rev. D **71** (2005), 084021; M. Shibata and K. Taniguchi, Phys. Rev. D **73** (2006), 064027.
- 85) K. Kiuchi, Y. Sekiguchi, M. Shibata, and K. Taniguchi, Phys. Rev. D **80** (2009), 064037.
- 86) L. Rezzolla, B. Giacomazzo, L. Baiotti, J. Granot, and C. Kouveliotou, and M. A. Aloy, Astrophys. J. Lett. **732** (2011), 6.
- 87) S. Setiawan, M. Ruffert, and H.-Th. Janka, Astron. Astrophys. **458** (2006), 553.
- 88) L. Dessart et al., Astrophys. J. **690** (2009), 1681.
- 89) I. H. Stairs, Science **304** (2004), 547.
- 90) D. R. Lorimer, Living Rev. Relat. **11** (2008), 8.
- 91) <http://www.lorene.obspm.fr/>
- 92) K. Hotokezaka, K. Kyutoku, H. Okawa, M. Shibata, and K. Kiuchi, Phys. Rev. D **83** (2011), 124008.
- 93) Y. Suwa and K. Murase, Phys. Rev. D **80** (2009), 123008.
- 94) N. Stergioulas, A. Bauswein, K. Zagkouris, and H.-T. Janka, Mon. Not. Roy. Astron. Soc. **418** (2011), 427.
- 95) M. Shibata and Y. Sekiguchi, Prog. Theor. Phys. **127** (2012), 535.
- 96) K. Kiuchi, M. Shibata, P. J. Montero, and J. A. Font, Phys. Rev. Lett. **106** (2011), 251102.
- 97) J. C. Papaloizou and J. E. Pringle, Mon. Not. Roy. Astron. Soc. **208** (1984), 721.
- 98) M. Shibata and Y. Sekiguchi, Phys. Rev. D **71** (2005), 024014.
- 99) M. Rampp, E. Müller, M. Ruffert, Astron. Astrophys. **332** (1998), 969.
- 100) C. D. Ott, S. Ou, J. E. Tohline, and A. Burrows, Astrophys. J. Lett. **625** (2005), 119.
- 101) S. Scheidegger, T. Fischer, S. C. Whitehouse, M. Liebendörfer, Astron. Astrophys. **490** (2008), 231; S. Scheidegger, R. Käppeli, T. Fischer, S. C. Whitehouse, M. Liebendörfer, Astron. Astrophys. **514** (2010), A51.
- 102) K. Kyutoku, H. Okawa, M. Shibata, and K. Taniguchi, Phys. Rev. D **84** (2011), 064018.
- 103) S. A. Balbus and J. F. Hawley, Rev. Mod. Phys. **70** (1998), 1.
- 104) J. Cooperstein and J. Wambach, Nucl. Phys. A **420** (1984), 591.
- 105) N. Itoh et al. Astrophys. J. Suppl. **102** (1996), 411.
- 106) C. J. Horowitz, Phys. Rev. D **65** (2002), 043001.
- 107) C. J. Horowitz, Phys. Rev. D **55** (1997), 4577.
- 108) L. B. Leinson, V. N. Oraevsky, and V. B. Semikoz, Phys. Lett. B **209** (1988), 80.
- 109) D. L. Tubbs and D. N. Schramm, Astrophys. J. **201** (1975), 467; A. Burrows, T. J. Mazurek, and J. M. Lattimer, Astrophys. J. **251** (1981), 325.
- 110) S. W. Bruenn and A. Mezzacappa, Phys. Rev. D **56** (1997), 7529.
- 111) N. Itoh et al. Astrophys. J. **611** (2004), 1041.
- 112) N. Itoh, Prog. Theor. Phys. **54** (1975), 1580.